

Nonequilibrium nanosystems

Pierre Gaspard

*Center for Nonlinear Phenomena and Complex Systems,
Université Libre de Bruxelles, Code Postal 231, Campus Plaine, B-1050 Brussels, Belgium*

An overview is presented of recent results on nonequilibrium processes at the nanoscale and their statistical thermodynamics. First of all, the different levels of description of small systems are presented from the microscopic molecular dynamics in terms of Newton's equations to the stochastic processes ruled by Langevin or master equations. In this framework, the connection to thermodynamic considerations can be established. The fluctuation theorem for currents in nonequilibrium steady states is established thanks to the analysis of the graph associated with the stochastic process. The fluctuation theorem for currents is shown to imply relations between the nonlinear response coefficients and the statistical cumulants of current fluctuations, which generalize Onsager reciprocity relations. Further consequences of the breaking of time-reversal symmetry in the statistical description are presented such as the theorem of nonequilibrium temporal ordering. All these results are shown to apply to several classes of nonequilibrium nanosystems. Selected case studies are presented for mechanical, mechanochemical, and chemical nonequilibrium nanosystems. For mechanical systems, we consider friction in the sliding motion of double-walled carbon nanotubes and microplasma heating by electromagnetic waves. For mechanochemical systems, recent work is summarized on the F₁-ATPase rotary nanomotor. For chemical systems, the reviewed examples are the chemical transistor, Schlögl's bistable reaction network, the Brusselator model of chemical clock, nanometric chemical clocks observed in field emission microscopy, as well as information processing in copolymerization processes with or without a template.

I. INTRODUCTION

The nanometer is the length scale just above the size of atoms. Accordingly, the nanoscale is the root of the tree of the structures made of atoms: molecules, macromolecules, polymers, fullerenes and nanotubes, atomic or molecular clusters, supramolecular assemblies, molecular machines, up to viruses, organelles or cells in the organic world, and gases, liquids, or solids in the inorganic world. It should be emphasized that the importance of these atomic systems holds not only in their 3D spatial structure but also in the 4D spatiotemporal paths they can perform, as it is the case for catalysts or molecular motors.

In principle, their motions are ruled by Newton's equations based on molecular forces which typically have nonlinear dependences on the interatomic distances. A key feature of atomic motions is their randomness that results from the incessant collisions among the atoms or molecules composing the nanosystem. This randomness manifests itself in the thermal and molecular fluctuations affecting to some extent every observable at the nanoscale. Accordingly, nanosystems are often described in terms of stochastic processes as it is the case for the Brownian motion of micrometric particles suspended in a liquid. In this example, the forces between the Brownian particle and the many molecules of the surrounding liquid are random on long time scales, the heavy Brownian particle being much slower than the light molecules of the liquid. Accordingly, the Newtonian equation for the Brownian particle contains a Langevin fluctuating force because of the interaction with the surrounding. Since Brownian motion is stochastic, its description is based on a probability distribution, which obeys a time-evolution equation called the master equation. As already pointed out by Einstein [1], Brownian particles are examples of mesoscopic systems which are larger than the molecules obeying the microscopic Newtonian dynamics but smaller than the macroscopic systems where the molecular fluctuations are so small with respect to their size that a deterministic description should be considered. In this regard, the stochastic description developed for Brownian motion is expected to apply at the nanoscale as well. The condition of validity of a stochastic approach is that some degree of freedom of the nanosystem should have a heavier mass than others, in which case there is a separation of time scales between the slow degree of freedom and the other ones responsible for the fast thermal fluctuations.

Because of the interaction between the slow and fast degrees of freedom, energy is exchanged between them. The asymmetry of the coupling between a few slow and many fast degrees of freedom leads to an energy flux from the former to the latter, which is the phenomenon of energy dissipation. Dissipation happens for instance if an excess of energy is initially deposited on the slow degrees of freedom and progressively dissipated over the fast degrees of freedom

during a relaxation which is determined by the interaction. If the subsystem is interacting with the many degrees of freedom of a thermal bath at a given temperature, its probability distribution undergoes a relaxation towards the equilibrium Boltzmann-Maxwell distribution at the temperature of the bath. During this relaxation, the subsystem is transiently out of equilibrium but ultimately reaches thermal equilibrium after a long enough time. These relaxation processes occur in isolated nanosystems such as atomic or molecular clusters where the slow degrees of freedom are associated with the spherical or nonspherical shape of the cluster while the fast degrees of freedom describe the motion of the individual atoms relative to the global shape. Statistical ensembles of clusters can be described in terms of probability distribution for all the internal degrees of freedom of the cluster, allowing several possible distributions for the total energy depending on the experimental technique to produce the beam of clusters [2]. Such nanosystems remain out of equilibrium during some relaxation time, but finally reach the thermodynamic equilibrium state after a long enough time [3]. Strictly speaking, the concepts of equilibrium state or relaxation times are associated with the probability distribution and its time evolution. The probability distribution describes a statistical ensemble of copies of the nanosystem, each launched from different initial conditions statistically distributed according to the initial probability density. Consequently, the concepts of equilibrium state or relaxation times do not concern an individual nanosystem, but instead ensembles composed of infinitely many copies of the nanosystem with statistically distributed degrees of freedom.

Besides the aforementioned nanosystems which relax towards an equilibrium state, there exist nanosystems which are in contact with at least two heat or particle reservoirs at different temperatures or chemical potentials. These nanosystems present the remarkable feature to reach a *nonequilibrium steady state* after some transient behavior. Contrary to the previous cases, such nanosystems sustain currents or fluxes of heat or particles and they remain out of equilibrium by energy supply from the external reservoirs. Although the instantaneous currents fluctuate in time, they are described by a probability distribution which remains stationary in the nonequilibrium steady state. The mean values of the fluctuating currents are not vanishing and controlled by the differences of temperatures or chemical potentials between the external reservoirs. These mean currents are sustained at the expense of energy dissipation. Therefore, such nonequilibrium nanosystems are characterized by a positive entropy production according to the second law of thermodynamics. In contrast, the entropy production vanishes in the equilibrium stationary state reached by nanosystems in contact with a single heat or particle reservoir. Examples of nonequilibrium nanosystems are the electronic circuits considered in semiconductor or molecular electronics, the chemical nanoreactors in heterogeneous catalysis, or the molecular motors in biology. These examples show the variety of nonequilibrium nanosystems and their importance for nanoscience and nanotechnology.

Further nonequilibrium nanosystems are those which are driven by a time-dependent external force. Examples of such nanosystems are macromolecules such as RNA undergoing repeated unfolding and folding processes by optical tweezers [4] or nanosystems with electric charges driven by electromagnetic fields. In these cases as well, the energy supplied by the external forces is dissipated during the process, leading to thermodynamic entropy production.

The nonequilibrium nanosystems are also of fundamental importance in biology [5]. Indeed, one of the key features of biological systems is their metabolism, meaning that biological systems are functioning out of equilibrium as open thermodynamic systems with an internal dissipation of the chemical energy from the nutrients supplied by the environment. The thermodynamic aspects of metabolism are traditionally envisaged at the macroscale. However, the biological systems are hierarchically structured from the nanoscale up to the macroscale. Indeed, molecules such as lipids form cellular membranes while copolymers such as proteins, RNA, and DNA combine into supramolecular assemblies functioning as machines: polymerases, ribosomes, flagellar motors, linear motors for cargo transport or muscle contraction. Many of these molecular structures exist only because of their ability to perform a specific motion powered by some energy source as provided by transmembrane pH differences or the hydrolysis of adenosine triphosphate (ATP). In this regard, energy transduction plays a fundamental role at the molecular level in all the biochemical processes of the metabolism [6]. The directionality so essential to biological functions is acquired at the nanoscale when the molecular structures are driven out of equilibrium by the metabolism. In this respect, the time scale over which a correlated motion can be maintained in some 3D molecular structure is here an essential property characterizing a biological function [7–10]. The nonequilibrium nanosystems thus find their importance not only for technological applications but also for our fundamental understanding of biological systems from the viewpoint of the physico-chemical laws of Nature.

The purpose of the present contribution is to give an overview of nonequilibrium nanosystems and to outline their statistical thermodynamics.

In Section II, the statistical thermodynamics of nanosystems is presented starting from the problem of their multi-scale description with, on the one hand, Newton's equations ruling the microscopic dynamics of their constituent atoms over the scales of picometers and femtoseconds and, on the other hand, stochastic processes describing the motion of some of their degrees of freedom on the spatial scales of nanometers or larger and over the time scales of picoseconds or longer. Recent advances in statistical thermodynamics are overviewed such as the fluctuation theorems that are large-deviation relations for the fluctuations of nonequilibrium work, currents, or other quantities [11–27],

as well as a new relationship established between the thermodynamic entropy production and the breaking of time reversal in the property of temporal disorder [28–31]. This latter is at the basis of a new understanding of information processing at the molecular level [32, 33].

Section III is devoted to mechanical nanosystems and, in particular, the study of friction in double-walled carbon nanotubes. This is an example of an isolated nanosystem evolving towards an equilibrium stationary state because it is not powered by continuous energy supply.

In Section IV, the case of mechanochemical nanosystems is considered. These nanosystems – such as the F₁-ATPase nanomotor – are continuously powered by chemical energy and can thus be driven into nonequilibrium stationary states. By their large molecular architecture, the mechanics of these molecular motors can be tightly coupled to their chemistry, allowing sustained rotary or linear motions under nonequilibrium conditions.

As presented in Section V, there also exist chemical nanosystems such as chemical clocks in far-from-equilibrium oscillatory regimes. In such systems, the directionality is maintained in a noisy limit cycle of the populations of small molecules involved in a network of coupled chemical reactions.

Conclusions and perspectives are drawn in Section VI.

II. STATISTICAL THERMODYNAMICS OF NONEQUILIBRIUM NANOSYSTEMS

A. From Newton's equations to stochastic processes

The same nanosystem may admit several descriptions depending on the spatial and temporal scales at which its motion is observed.

At room temperature, the dynamics of atoms can be supposed to be classical in many circumstances. Under these conditions, the microscopic dynamics is ruled by Newton's equations for all the atoms of masses $\{m_a\}_{a=1}^N$ and positions $\{\mathbf{r}_a\}_{a=1}^N$ composing the system. These atoms are coupled by interatomic forces $\mathbf{F}(\mathbf{r}_a - \mathbf{r}_b) = -\nabla U(\mathbf{r}_a - \mathbf{r}_b)$, deriving from the Born-Oppenheimer potential energy $U(\mathbf{r}_a - \mathbf{r}_b)$ of the interaction between the atoms in the electronic quantum state of the molecular system. Besides, an external force can be applied to the system, $\mathbf{F}_{\text{ext}}(\mathbf{r}_a) = -\nabla U_{\text{ext}}(\mathbf{r}_a)$. The sum over all the forces acting on the atom is thus equal to its acceleration multiplied by its mass:

$$m_a \frac{d^2 \mathbf{r}_a}{dt^2} = \mathbf{F}_{\text{ext}}(\mathbf{r}_a) + \sum_{b(\neq a)} \mathbf{F}(\mathbf{r}_a - \mathbf{r}_b) \quad (1)$$

where $a, b = 1, 2, \dots, N$ are the labels of all the atoms composing not only the nanosystem, but also the reservoirs which are in contact with it if this latter is not isolated. Equivalently, Hamilton's equations

$$\begin{cases} \frac{d\mathbf{r}_a}{dt} = +\frac{\partial H}{\partial \mathbf{p}_a} \\ \frac{d\mathbf{p}_a}{dt} = -\frac{\partial H}{\partial \mathbf{r}_a} \end{cases} \quad (2)$$

govern the time evolution of the positions $\{\mathbf{r}_a\}_{a=1}^N$ and momenta $\{\mathbf{p}_a = m_a d\mathbf{r}_a/dt\}_{a=1}^N$ of all the atoms in the system. This formulation is expressed in terms of the Hamiltonian function which represents the total energy of the whole system:

$$H = \sum_{1 \leq a \leq N} \left[\frac{\mathbf{p}_a^2}{2m_a} + U_{\text{ext}}(\mathbf{r}_a) \right] + \sum_{1 \leq a < b \leq N} U(\mathbf{r}_a - \mathbf{r}_b) \quad (3)$$

The Hamiltonian dynamics is deterministic in the sense that, according to Cauchy's theorem, a unique trajectory is issued from initial conditions taken as a point in the phase space of the positions and momenta:

$$\mathbf{\Gamma} = (\mathbf{r}_1, \mathbf{r}_2, \dots, \mathbf{r}_N, \mathbf{p}_1, \mathbf{p}_2, \dots, \mathbf{p}_N) \quad (4)$$

Therefore, the time evolution of a time-independent system is given by a flow, i.e., a one-parameter continuous group defined in the phase space:

$$\mathbf{\Gamma}(t) = \mathbf{\Phi}^t [\mathbf{\Gamma}(0)] \quad (5)$$

Moreover, the Hamiltonian system (3) is symmetric under the time reversal defined by the operation:

$$\mathbf{\Theta}(\mathbf{r}_1, \mathbf{r}_2, \dots, \mathbf{r}_N, \mathbf{p}_1, \mathbf{p}_2, \dots, \mathbf{p}_N) = (\mathbf{r}_1, \mathbf{r}_2, \dots, \mathbf{r}_N, -\mathbf{p}_1, -\mathbf{p}_2, \dots, -\mathbf{p}_N) \quad (6)$$

because the Hamiltonian (3) is an even function of the momenta. Accordingly, the time reversal of every solution of Hamilton's equations (2) is also a solution, a property called *microreversibility*. It is fundamental to notice that microreversibility does not necessarily imply the coincidence of a trajectory with its time reversal so that the selection of initial conditions can break the time-reversal symmetry of the actual history followed by the system [34–37].

Since the phase space is a continuum, the real numbers (4) defining the initial conditions are practically known by their few first digits so that the effective knowledge of the initial conditions is always limited. Therefore, an error always affects the preparation of initial conditions launching a trajectory. This inherent limitation of the knowledge of initial conditions taking their values in a continuum justifies the introduction of a probability distribution for the initial positions and momenta compatible with the precision with which they are prepared, $p_0(\mathbf{\Gamma})$. This probability distribution evolves in time according to the Liouville equation

$$\partial_t p = \{H, p\}_{\text{Poisson}} \equiv \hat{L} p \quad (7)$$

where the Poisson bracket with the Hamiltonian defines the Liouvillian operator \hat{L} . According to Liouville's theorem, the probability density at time t is given in terms of the initial probability density by

$$p(\mathbf{\Gamma}, t) = p_0 [\Phi^{-t}(\mathbf{\Gamma})] \quad (8)$$

which defines the so-called Perron-Frobenius operator [38]. If the total system is isolated, the probability distribution may converge in the weak sense towards a stationary probability distribution defining an invariant probability measure, which should correspond to the thermodynamic equilibrium state, $p_{\text{eq}}(\mathbf{\Gamma})$. The condition for this weak convergence is the property of mixing [39, 40]. We notice that nonequilibrium states can also be defined as conditionally invariant measures by suitably renormalizing the transient probability distribution evolving in time under given nonequilibrium constraints [38]. In this way, conditionally invariant measures have been constructed in the escape-rate theory or in the hydrodynamic-mode theory [38].

The determinism of Hamiltonian systems does not preclude the possibility of dynamical randomness, i.e., temporal disorder in the long-time evolution of such systems. This dynamical randomness finds its origin in the sensitivity to initial conditions. We notice that this property manifests itself in the so-called chaotic systems, but does not appear in integrable systems having as many constants of motion as degrees of freedom. The sensitivity to initial conditions is characterized by the positivity of at least one Lyapunov exponent [41]. These latter quantities are the rates of exponential separation

$$\lambda_i = \lim_{t \rightarrow \infty} \frac{1}{t} \ln \frac{\|\delta \mathbf{\Gamma}_i(t)\|}{\|\delta \mathbf{\Gamma}_i(0)\|} \quad (9)$$

between a reference trajectory (5) and perturbed trajectories issued from infinitesimally close initial conditions $\mathbf{\Gamma}(0) + \delta \mathbf{\Gamma}_i(0)$ taken in any possible direction i in the $6N$ -dimensional phase space (4). In molecular dynamics, typical Lyapunov exponents are of the order of the inverse of the intercollisional time, which corresponds to the time scale of the thermal fluctuations [42–45]. The dynamical instability characterized by positive Lyapunov exponents implies that trajectories issued from nearby initial conditions may have very different histories, which are thus unpredictable beyond the time scale given by the inverse of the maximal Lyapunov exponent. Over time scales longer than this Lyapunov horizon of predictability, the trajectory appears random listing in time the digits of the real numbers defining its initial conditions. Therefore, dynamical randomness can be characterized as temporal disorder in terms of the so-called Kolmogorov-Sinai entropy per unit time which is equal to the sum of positive Lyapunov exponents according to Pesin's theorem [41]:

$$h_{\text{KS}} = \sum_{\lambda_i > 0} \lambda_i \quad (10)$$

This property of temporal disorder manifests itself in the stochasticity of the random processes describing the slow degrees of freedom of the system where it is characterized by the (ε, τ) -entropy per unit time [46]. Accordingly, the motion of atoms in condensed phases at room temperature is highly random as observed by their thermal and molecular fluctuations.

Methods have been developed in chaos theory to construct solutions of Liouville's equation – in particular, conditionally invariant measures – by using the Lyapunov exponents associated with each trajectory, as it is the case in the periodic-orbit theory [38, 47]. The idea is that the larger the positive Lyapunov exponents of a trajectory, the higher its instability, and the lower its probability weight. Methods based on this idea allow us to construct exact solutions of Liouville's equation on fine scales in the phase space of the system. In this regard, the methods of chaos theory justify on a fundamental ground the existence of relaxation times which are intrinsic to the dynamics.

In many systems, these relaxation times can be obtained with excellent approximations thanks to the coarse-grained descriptions considered since the pioneering work of Boltzmann [48], Einstein [1], Langevin [49], Fokker [50], Planck [51], Pauli [52], and others. Such coarser descriptions focus on a few relevant observables among all the degrees of freedom of the total system. Examples are given by the indicator functions of subsets ω taken inside the phase space: $I_\omega(\mathbf{\Gamma}) = 1$ if $\mathbf{\Gamma} \in \omega$ and zero otherwise. The probability that the system visits this subset at the time t is given by the mean value of this observable taken over the phase-space probability distribution (8) at this time:

$$P(\omega, t) \equiv \int I_\omega(\mathbf{\Gamma}) p(\mathbf{\Gamma}, t) d\mathbf{\Gamma} \quad (11)$$

If these probabilities evolve more slowly than the other observables, the memory of the fast degrees of freedom may be lost over the time scale of variation of these probabilities, which may justify that their time evolution is ruled by a Markovian master equation such as

$$\frac{dP(\omega, t)}{dt} = \sum_{\rho, \omega'} [P(\omega', t) W_{+\rho}(\omega'|\omega) - P(\omega, t) W_{-\rho}(\omega|\omega')] \quad (12)$$

where $W_\rho(\omega'|\omega)$ is the rate of the transition $\omega' \xrightarrow{\rho} \omega$ induced by some elementary mechanism ρ [53–56]. The relaxation times of the stochastic process ruled by this master equation can be obtained in terms of the eigenvalues of this equation. It is interesting to note that stochastic processes have a dual description either in terms of the probabilities ruled by the master equation or in terms of individual random realizations of the time evolution as simulated for instance by Gillespie's algorithm [57, 58]. Such random realizations are paths in the space of the coarse-grained states $\{\omega\}$

$$\omega = \omega_0 \xrightarrow{\rho_1} \omega_1 \xrightarrow{\rho_2} \omega_2 \xrightarrow{\rho_3} \dots \xrightarrow{\rho_n} \omega_n \quad (13)$$

with random jumps $\omega_{j-1} \xrightarrow{\rho_j} \omega_j$ between dwelling time intervals $t_j < t < t_{j+1}$, during which the system stays in the state ω_j . By construction, such a random path should be statistically equivalent to the path that would be obtained from the deterministic trajectory starting from some compatible initial conditions: $\omega[\mathbf{\Gamma}(t)] = \omega\{\Phi^t[\mathbf{\Gamma}(0)]\}$.

In the case of Brownian motion in an external force field $\mathbf{F}_{\text{ext}}(\mathbf{r})$, random paths can be simulated by integrating Langevin's equation

$$m \frac{d^2 \mathbf{r}}{dt^2} = \mathbf{F}_{\text{ext}}(\mathbf{r}) - \zeta \frac{d\mathbf{r}}{dt} + \mathbf{F}_L(t) \quad (14)$$

which is a Newtonian equation where the friction force $\mathbf{F}_{\text{frict}} = -\zeta d\mathbf{r}/dt$ and the associated fluctuating Langevin force $\mathbf{F}_L(t)$ represent the contributions of the forces between the Brownian particle and the molecules of the surrounding fluid [59]. The Langevin forces can be modeled as Gaussian white noises:

$$\langle F_{L,i}(t) \rangle = 0 \quad (15)$$

$$\langle F_{L,i}(t) F_{L,j}(t') \rangle = 2\zeta k_B T \delta(t - t') \delta_{ij} \quad (16)$$

where $i, j = x, y, z$ denote the Cartesian components of the force, ζ the friction coefficient, T the temperature of the surrounding fluid, and $k_B = 1.38 \cdot 10^{-23}$ J/K Boltzmann's constant. The Langevin equation (14) is a stochastic differential equation. Its solutions $\mathbf{r}(t)$ mimic the motion of the Brownian particle as given by typical solutions of Hamilton's equations (2), $\mathbf{r}(t) = \mathbf{r}_1[\mathbf{\Gamma}(t)] = \mathbf{r}_1\{\Phi^t[\mathbf{\Gamma}(0)]\}$, supposing that the Brownian particle has the label $a = 1$ among the N particles of the system.

In the stochastic model by Langevin, the time correlation functions of the fluctuating force coming from the fluid are delta-correlated, meaning that the time over which the correlation functions decay to zero is much shorter than the time scale of the described process. This correlation time is of the order of the intercollisional time of the Brownian particle with surrounding molecules. We notice that the friction coefficient can in general be calculated in terms of the integral of the time correlation function of the fluctuating force according to the Kirkwood formula [60]

$$\zeta = \frac{1}{2k_B T} \int_{-\mathcal{T}}^{+\mathcal{T}} \langle F_{L,i}(t) F_{L,i}(0) \rangle dt \quad (17)$$

where \mathcal{T} is a time scale longer than the correlation time but shorter than the time over which the conservation of the total linear momentum of the total system might manifest itself. If the system is infinite, the limit $\mathcal{T} \rightarrow \infty$ may be taken. The Kirkwood formula for the friction coefficient has been extended to the famous Green-Kubo formulas for the coefficients of transport properties such as the viscosities, the conductivities, as well as the diffusivities [61, 62].

The master equation corresponding to the Langevin equation (14) is the Fokker-Planck equation

$$\frac{\partial \mathcal{P}}{\partial t} + \mathbf{v} \cdot \frac{\partial \mathcal{P}}{\partial \mathbf{r}} + \frac{\mathbf{F}_{\text{ext}}}{m} \cdot \frac{\partial \mathcal{P}}{\partial \mathbf{v}} = \frac{\zeta}{m} \frac{\partial}{\partial \mathbf{v}} \cdot (\mathbf{v} \mathcal{P}) + \frac{\zeta k_B T}{m^2} \frac{\partial^2 \mathcal{P}}{\partial \mathbf{v}^2} \quad (18)$$

where \mathcal{P} denotes the probability density to find the Brownian particle with the position \mathbf{r} and the velocity \mathbf{v} at the time t [59]. This probability density corresponds in principle to the probability distribution obeying Liouville's equation (7) according to

$$\mathcal{P}(\mathbf{r}, \mathbf{v}, t) \equiv \int \delta(\mathbf{r} - \mathbf{r}_1) \delta(\mathbf{v} - \mathbf{p}_1/m) p(\mathbf{\Gamma}, t) d\mathbf{\Gamma} \quad (19)$$

In this regard, the delta distributions play a similar role as the indicator function in Eq. (11).

In the case where the external force is time independent and derives from a potential $\mathbf{F}_{\text{ext}}(\mathbf{r}) = -\nabla U_{\text{ext}}(\mathbf{r})$, the solution of Fokker-Planck equation undergoes a relaxation towards an asymptotic equilibrium state given by the Boltzmann-Maxwell distribution:

$$\lim_{t \rightarrow \infty} \mathcal{P}(\mathbf{r}, \mathbf{v}, t) = \mathcal{P}_{\text{eq}}(\mathbf{r}, \mathbf{v}) \equiv \mathcal{N} \exp \left[-\frac{m\mathbf{v}^2}{2k_B T} - \frac{U_{\text{ext}}(\mathbf{r})}{k_B T} \right] \quad (20)$$

with a normalization constant \mathcal{N} such that $\int \mathcal{P}_{\text{eq}}(\mathbf{r}, \mathbf{v}) d\mathbf{r} d\mathbf{v} = 1$.

In contrast, if the external force is time dependent, the system remains out of equilibrium. If the Brownian particle is dragged by an optical trap moving at the velocity \mathbf{u} , the external potential is given by $U_{\text{ext}} = (\kappa/2)(\mathbf{r} - \mathbf{u}t)^2$ and the probability density can reach a nonequilibrium stationary solution in the frame of the optical trap. In this nonequilibrium state, the energy supplied by the optical trap is dissipated by the friction of the Brownian particle on the surrounding fluid, leading to a positive thermodynamic entropy production.

Brownian motion is the paradigm of physico-chemical stochastic processes. This paradigm can be extended down to the nanoscale and applied to mechanical systems such as multiwalled carbon nanotubes, as well as to molecular motors where mechanics is coupled to chemistry. Multiwalled carbon nanotubes have slow and fast degrees of freedom and thus qualify for a description in terms of stochastic processes (see Section III). In molecular motors, the stochastic process is a combination of diffusive mechanical motions interrupted by random jumps between discrete chemical states due to reactive events. Such diffusion-reaction stochastic processes are governed by coupled Fokker-Planck equations (see Section IV).

The paradigm also extends to mesoscopic chemical systems where reactions transform populations of molecules. In mesoscopic chemical systems such as nanoreactors or nanoelectrodes, the numbers of molecules are random variables jumping at each reactive event. Therefore, the molecular numbers obey a stochastic process compatible with the mass-action law of chemical kinetics [53–56]. At the macroscale, the molecular fluctuations disappear and the chemical concentrations follow deterministic differential equations of chemical kinetics. At the mesoscale, chemical systems can be described as continuous-time jump processes ruled by a master equation for the probability $P(\{N_i\}, t)$ of finding N_i molecules of species $i = 1, 2, \dots, c$ in the system or as diffusive processes ruled by a Fokker-Planck equation for the probability density $\mathcal{P}(\{x_i\}, t)$ defined in the space of chemical concentrations $x_i = N_i/N$ where $N = \sum_{i=1}^c N_i$ is the total number of molecules in the system (see Section V).

Master equations have also been deduced for quantum systems at the nanoscale [63].

B. Entropy and the second law of thermodynamics

Since its historical origin in the pioneering work by Sadi Carnot on the efficiency of steam engines, the concept of entropy is associated with the idea of partitioning the system into microscopic degrees of freedom having their own dynamics and macroscopic ones which can be manipulated at will. In a steam engine, the former are the degrees of freedom of the water molecules and the latter the piston and the valves of the engine. In this regard, the thermodynamic entropy appears as a property of the system of microscopic degrees of freedom with respect to their manipulation by a coarser device which is external to the described system. *A priori*, the thermodynamic entropy is thus a property of the system with respect to a coarse graining superimposed by some external apparatus.

Accordingly, the concept of entropy applies to nanosystems described in terms of the probabilities (11) to visit some coarse-grained states ω . The thermodynamic entropy associated at time t can be defined as

$$S(t) = \sum_{\omega} S(\omega) P(\omega, t) - k_B \sum_{\omega} P(\omega, t) \ln P(\omega, t) \quad (21)$$

The first term is the mean contribution of the entropy $S(\omega)$ due to the statistical distribution of all the degrees of freedom which are not specified by the coarse-grained state ω [20]. For instance, if the coarse-grained state ω only specifies the numbers of the molecules of the different chemical species, $S(\omega)$ is the entropy of the statistical distribution of the positions and momenta of the particles enumerated by ω . The second term characterizes the disorder in statistical distribution $P(\omega, t)$ over the different coarse-grained states $\{\omega\}$.

Since the probability distribution $\{P(\omega, t)\}$ evolves in time according to the master equation (12), the entropy (21) varies accordingly. It is well known that the time variation of the entropy can be decomposed as [64, 65]:

$$\frac{dS}{dt} = \frac{d_e S}{dt} + \frac{d_i S}{dt} \quad (22)$$

into the entropy flow or entropy exchange between the system and its environment and the entropy production which is internal to the system. The *entropy flow* is given by

$$\frac{d_e S}{dt} = \sum_{\rho, \omega, \omega'} [P(\omega', t) W_{+\rho}(\omega'|\omega) - P(\omega, t) W_{-\rho}(\omega|\omega')] \left[S(\omega) - \frac{k_B}{2} \ln \frac{W_{+\rho}(\omega'|\omega)}{W_{-\rho}(\omega|\omega')} \right] \quad (23)$$

which can be either positive or negative. On the other hand, the *entropy production*

$$\frac{d_i S}{dt} = \frac{k_B}{2} \sum_{\rho, \omega, \omega'} [P(\omega', t) W_{+\rho}(\omega'|\omega) - P(\omega, t) W_{-\rho}(\omega|\omega')] \ln \frac{P(\omega', t) W_{+\rho}(\omega'|\omega)}{P(\omega, t) W_{-\rho}(\omega|\omega')} \geq 0 \quad (24)$$

is always non-negative in agreement with the second law of thermodynamics [64, 65]. In a system without external nonequilibrium constraint, the probability distribution $P(\omega, t)$ undergoes a relaxation towards the equilibrium state $P_{\text{eq}}(\omega)$ for which the entropy production vanishes because of the detailed balancing conditions

$$P_{\text{eq}}(\omega') W_{+\rho}(\omega'|\omega) = P_{\text{eq}}(\omega) W_{-\rho}(\omega|\omega') \quad (25)$$

which should hold for all the possible transitions $\omega' \xrightarrow{\rho} \omega$ [66, 67]. During relaxation, the system is transiently out of equilibrium so that the entropy production is positive. The entropy production vanishes asymptotically as the time goes to infinity and the thermodynamic equilibrium is reached.

If external nonequilibrium constraints are imposed to the system, the relaxation proceeds towards a nonequilibrium steady state, $(d/dt)P_{\text{neq}}(\omega) = 0$, in which the detailed balancing conditions (25) do not hold and the entropy production remains positive. Therefore, the thermodynamic entropy production allows us to distinguish between nonequilibrium and equilibrium steady states among all the stationary solutions of the master equation (12) such that $(d/dt)P_{\text{st}}(\omega) = 0$.

C. Identifying the nonequilibrium constraints and the currents with graph analysis

The nonequilibrium constraints are the control parameters driving the nanosystem out of equilibrium. These control parameters are the differences of temperatures or chemical potentials between the heat or particle reservoirs in contact with the nanosystem. In the case of chemical reactions, the difference of chemical potentials is taken between the reactants and the products of each reaction and they are controlled by chemical concentrations. These control parameters are hidden in the transition rates $W_{\rho}(\omega'|\omega)$ of the stochastic process and an important issue is to identify them.

A systematic method is provided with graph theory, as developed by Hill and Schnakenberg [6, 64]. A graph is associated with the stochastic process as follows: Each state ω of the system defines a vertex or node of the graph while each allowed transition $\omega \xrightleftharpoons[\rho]{+\rho} \omega'$ corresponds to an edge. In this respect, two states can be connected by several edges if several elementary processes ρ allow transitions between them.

An orientation is given to each edge of the graph G . The directed edges are thus defined by

$$e \equiv \omega \xrightarrow{\rho} \omega' \quad (26)$$

Let F be a directed subgraph of G . The orientation of the subgraph F with respect to its edges $\{e\}$ is described by introducing the quantity

$$s_e(F) \equiv \begin{cases} +1 & \text{if } e \text{ and } F \text{ are parallel} \\ -1 & \text{if } e \text{ and } F \text{ are antiparallel} \\ 0 & \text{if } e \text{ is not in } F \end{cases} \quad (27)$$

where e and F are said to be parallel (respectively antiparallel) if F contains the edge e in its reference (respectively opposite) orientation.

In order to identify all the cycles of a graph, a concept of maximal tree is introduced [64]. Every maximal tree $T(G)$ of the graph G should satisfy the following properties:

- (1) $T(G)$ is a covering subgraph of G , i.e., $T(G)$ contains all the vertices of G and all the edges of $T(G)$ are edges of G ;
- (2) $T(G)$ is connected;
- (3) $T(G)$ contains no cycle (i.e., no cyclic sequence of edges).

The edges l of the graph G which do not belong to the maximal tree $T(G)$ are called the chords of $T(G)$. If we add to $T(G)$ one of its chords l , the resulting subgraph $T(G) + l$ contains exactly one cycle C_l , which is obtained from $T(G) + l$ by removing all the edges which are not part of the cycle. The convention is used that the orientation is such that $\varsigma_l(C_l) = 1$, i.e., the cycles are oriented as the chords l . A maximal tree $T(G)$ together with its associated fundamental set of cycles $\{C_1, C_2, \dots, C_l, \dots\}$ provides a decomposition of the graph G .

We notice that a given graph G has several maximal trees $T(G)$ and that all the maximal trees of a graph can be obtained by linear combinations of a given maximal tree $T(G)$ with its associated cycles, as described in Ref. [64].

A remarkable property is that the ratio of the products of the transition rates $W_\rho(\omega'|\omega)$ along the two possible directions of any cycle C_l of the graph is independent of the states composing the cycle and will thus only depend on the external nonequilibrium constraints imposed to the system [64]. Thanks to this property, the thermodynamic forces – also called the affinities [68, 69] – can be introduced according to [64]

$$\prod_{e \in C_l} \frac{W_{+\rho}(\omega|\omega')}{W_{-\rho}(\omega'|\omega)} = \exp A(C_l) \quad (28)$$

where $e \in C_l$ denotes the edges (26) in the cycle C_l . In the equilibrium state, the affinities vanish and we recover the conditions of detailed balancing between every forward and backward transition. An important observation is that many of these affinities are equal, $A(C_l) = A_\alpha$ for all $C_l \in \alpha$, which defines the macroscopic affinities A_α imposed by the external reservoirs.

The instantaneous current on the chord l is defined by [22]

$$j_l(t) \equiv \sum_{n=-\infty}^{+\infty} \varsigma_l(e_n) \delta(t - t_n) \quad (29)$$

where t_n is the time of the random transition e_n during a path of the stochastic process. The convention is used that j_l is oriented as the graph G since $\varsigma_l(e_n)$ is equal to (-1) if the transition e_n is (anti)parallel to the chord l . The current (29) is a fluctuating random variable. The different microscopic currents corresponding to a given macroscopic process α can now be regrouped as [22]

$$j_\alpha(t) \equiv \sum_{l \in \alpha} j_l(t) = \sum_{l \in \alpha} \sum_{n=-\infty}^{+\infty} \varsigma_l(e_n) \delta(t - t_n) \quad (30)$$

Examples of nonequilibrium stochastic processes described by the Markovian master equation (12) and their graph analysis are provided in the following sections.

D. Fluctuation theorem for the currents

In the previous framework, a fundamental result can be obtained for the full counting statistics of the fluctuating currents (30) which are flowing across the nanosystem in some nonequilibrium steady state. The generating function of all the statistical cumulants of the fluctuating currents is defined as

$$Q(\boldsymbol{\lambda}, \mathbf{A}) \equiv \lim_{t \rightarrow \infty} -\frac{1}{t} \ln \left\langle \exp \left[-\boldsymbol{\lambda} \cdot \int_0^t dt' \mathbf{j}(t') \right] \right\rangle \quad (31)$$

with $\boldsymbol{\lambda} = \{\lambda_\alpha\}$, $\mathbf{A} = \{A_\alpha\}$, and $\mathbf{j}(t) = \{j_\alpha(t)\}$. We notice that the generating function depends on the affinities because the statistical average $\langle \cdot \rangle$ is carried out in the steady state corresponding to the values \mathbf{A} of the affinities. The mean value of a current is given by differentiating the generating function with respect to the parameter λ_α and setting afterwards all these parameters to zero:

$$J_\alpha(\mathbf{A}) \equiv \left. \frac{\partial Q}{\partial \lambda_\alpha} \right|_{\boldsymbol{\lambda}=0} = \lim_{t \rightarrow \infty} \frac{1}{t} \int_0^t \langle j_\alpha(t') \rangle dt' \quad (32)$$

The diffusivities or second cumulants of the fluctuating currents can be defined as

$$D_{\alpha\beta}(\mathbf{A}) \equiv -\frac{1}{2} \frac{\partial^2 Q}{\partial \lambda_\alpha \partial \lambda_\beta} \Big|_{\boldsymbol{\lambda}=0} = \frac{1}{2} \int_{-\infty}^{+\infty} \langle [j_\alpha(t) - \langle j_\alpha \rangle] [j_\beta(0) - \langle j_\beta \rangle] \rangle dt \quad (33)$$

Higher-order statistical cumulants can be defined similarly such as the third and fourth cumulants

$$C_{\alpha\beta\gamma}(\mathbf{A}) \equiv \frac{\partial^3 Q}{\partial \lambda_\alpha \partial \lambda_\beta \partial \lambda_\gamma} \Big|_{\boldsymbol{\lambda}=0} \quad (34)$$

$$B_{\alpha\beta\gamma\delta}(\mathbf{A}) \equiv -\frac{1}{2} \frac{\partial^4 Q}{\partial \lambda_\alpha \partial \lambda_\beta \partial \lambda_\gamma \partial \lambda_\delta} \Big|_{\boldsymbol{\lambda}=0} \quad (35)$$

which all characterize the full counting statistics of the coupled fluctuating currents $\{j_\alpha(t)\}$.

We have the

Fluctuation theorem for the currents: *The generating function (31) obeys the symmetry relation*

$$Q(\boldsymbol{\lambda}, \mathbf{A}) = Q(\mathbf{A} - \boldsymbol{\lambda}, \mathbf{A}) \quad (36)$$

which has been proved in the framework of graph theory [21–23]. This theorem can also be proved for open quantum systems as a consequence of microreversibility [26, 27].

The Legendre transform of the generating function (31)

$$H(\boldsymbol{\xi}, \mathbf{A}) = \text{Max}_{\boldsymbol{\lambda}} [Q(\boldsymbol{\lambda}, \mathbf{A}) - \boldsymbol{\lambda} \cdot \boldsymbol{\xi}] \quad (37)$$

is the decay rate of the probability that the fluctuating currents averaged over the finite time interval t take their values in the ranges $(\boldsymbol{\xi}, \boldsymbol{\xi} + d\boldsymbol{\xi})$

$$H(\boldsymbol{\xi}, \mathbf{A}) \equiv \lim_{t \rightarrow \infty} -\frac{1}{t} \ln P \left[\frac{1}{t} \int_0^t \mathbf{j}(t') dt' \simeq \boldsymbol{\xi} \right] \quad (38)$$

where P denotes the probability distribution of the nonequilibrium steady state corresponding to the affinities \mathbf{A} . In terms of these decay rates, the fluctuation theorem (36) can be written as

$$H(-\boldsymbol{\xi}, \mathbf{A}) - H(\boldsymbol{\xi}, \mathbf{A}) = \mathbf{A} \cdot \boldsymbol{\xi} \quad (39)$$

which means that the ratio of the probabilities that the fluctuating currents take opposite values behaves exponentially in time with a rate equal to the affinities \mathbf{A} multiplied by the supposed values $\boldsymbol{\xi}$ for the currents:

$$\frac{P \left[\frac{1}{t} \int_0^t \mathbf{j}(t') dt' \simeq +\boldsymbol{\xi} \right]}{P \left[\frac{1}{t} \int_0^t \mathbf{j}(t') dt' \simeq -\boldsymbol{\xi} \right]} \simeq \exp(\mathbf{A} \cdot \boldsymbol{\xi} t) \quad \text{for } t \rightarrow \infty \quad (40)$$

If the fluctuating currents take their mean values (32), $\boldsymbol{\xi} = \mathbf{J}$, the decay rate vanishes by the law of large numbers, $H(\mathbf{J}, \mathbf{A}) = 0$, so that Eq. (40) shows that the probability of the opposite values $-\mathbf{J}$ decays at a rate equal to

$$\frac{1}{k_B} \frac{d_i S}{dt} = \mathbf{A} \cdot \mathbf{J} \geq 0 \quad (41)$$

which is the well-known expression of the entropy production in nonequilibrium thermodynamics [69]. This relation shows that the fluctuation theorem provides an extension of the second law of thermodynamics to small systems. At equilibrium, the affinities vanish with the currents and the thermodynamic entropy production, as expected. Away from equilibrium, the fluctuation theorem (40) shows that an asymmetry appears between the probabilities of opposite fluctuations: the farther from equilibrium, the lower the probability of reversed fluctuations. Since the ratio of probabilities depends exponentially on the time and the affinities, the reversed fluctuations rapidly become negligible as the system is driven far from equilibrium. Ultimately, the probability of the reversed fluctuations vanishes in fully irreversible regimes where the entropy production is infinite.

E. Consequences for linear and nonlinear response coefficients

Typically, the currents flowing across the nanosystem have a nonlinear dependence on the affinities. It is only if the nonequilibrium constraints are weak and the system remains close to equilibrium that the currents may have a linear dependence on the affinities. This is the case for transport properties such as heat conductivity, viscosity, or diffusion in macroscopic fluids. However, nonlinearities tend to manifest themselves in nanosystems because of their inherent heterogeneities. These nonlinearities are well known in chemical reactions which are completed after the breaking of chemical bonds over subnanometric distances [54, 69]. Accordingly, we should expect that nanosystems might present highly nonlinear properties.

The affinities are the thermodynamic forces driving the system out of equilibrium. In this regard, they represent the control parameters probing the responses of the system to external perturbations. If the perturbations are weak, the system remains in the linear regime around its state of thermodynamic equilibrium. If the perturbations are stronger, the effects of the nonlinear responses become observable. Whereupon, the response properties of the system with respect to the nonequilibrium constraints can be defined by expanding the currents in powers of the affinities as

$$J_\alpha = \sum_{\beta} L_{\alpha,\beta} A_\beta + \frac{1}{2} \sum_{\beta,\gamma} M_{\alpha,\beta\gamma} A_\beta A_\gamma + \frac{1}{6} \sum_{\beta,\gamma,\delta} N_{\alpha,\beta\gamma\delta} A_\beta A_\gamma A_\delta + \dots \quad (42)$$

The linear response of the currents J_α with respect to a small perturbation in the affinities A_β is characterized by the Onsager coefficients $L_{\alpha,\beta}$ and the nonlinear response by the higher-order coefficients $M_{\alpha,\beta\gamma}$, $N_{\alpha,\beta\gamma\delta}$,...

Since the currents can be deduced from the generating function (31) according to Eq. (32), any symmetry of the generating function will imply special relations among the linear and nonlinear response coefficients in the expansion (42). This is the case for the symmetry relation given by the fluctuation theorem (36). Indeed, the response coefficients can be found by differentiating the relation (36) with respect to the parameters λ and the affinities \mathbf{A} .

The linear response coefficients $L_{\alpha,\beta}$ are given by differentiating twice the generating function with respect to λ_α and A_β . Using the fluctuation theorem (36), the linear response coefficients can be shown to be equal to the diffusivities (33) taken at equilibrium, $L_{\alpha,\beta} = D_{\alpha\beta}(\mathbf{0})$. We notice that this is the content of the fluctuation-dissipation theorem and the Green-Kubo formulas [61, 62]. Since the diffusivities are symmetric under the exchange of the indices α and β , we recover Onsager's reciprocity relations [70]

$$L_{\alpha,\beta} = L_{\beta,\alpha} \quad (43)$$

The remarkable result is that this method can proceed to higher orders, leading to new relations between the nonlinear response coefficients and quantities characterizing the nonequilibrium fluctuations of the currents [21, 71]. The second-order response coefficients can be related to the diffusivities according to

$$M_{\alpha,\beta\gamma} = \left(\frac{\partial D_{\alpha\beta}}{\partial A_\gamma} + \frac{\partial D_{\alpha\gamma}}{\partial A_\beta} \right)_{\mathbf{A}=0} \quad (44)$$

Similarly, the third-order response coefficients turn out to be related to the fourth and second cumulants by

$$N_{\alpha,\beta\gamma\delta} = \left(\frac{\partial^2 D_{\alpha\beta}}{\partial A_\gamma \partial A_\delta} + \frac{\partial^2 D_{\alpha\gamma}}{\partial A_\beta \partial A_\delta} + \frac{\partial^2 D_{\alpha\delta}}{\partial A_\beta \partial A_\gamma} - \frac{1}{2} B_{\alpha\beta\gamma\delta} \right)_{\mathbf{A}=0} \quad (45)$$

while the third and fourth cumulants are linked by

$$B_{\alpha\beta\gamma\delta}(\mathbf{0}) = \left(\frac{\partial C_{\alpha\beta\gamma}}{\partial A_\delta} \right)_{\mathbf{A}=0} \quad (46)$$

Such relations exist at arbitrary orders as consequences of the fluctuation theorem [71]. Similar relations can be deduced in the presence of an external magnetic field [26]. They characterize the nonlinear response properties of nonequilibrium nanosystems.

F. Temporal disorder

At the nanoscale, the currents are fluctuating either at equilibrium or out of equilibrium. These fluctuations are the manifestation of dynamical randomness due to the incessant collisions among the particles composing the system. This dynamical randomness can be characterized as a property of disorder in the successive pictures of the system

in movies of the stochastic process. The time series of the fluctuating currents can be analyzed and its temporal disorder characterized by an entropy per unit time. Such a quantity is defined as an (ε, τ) -entropy per unit time for the fluctuating signal sampled with a resolution ε and a sampling time τ [46]. In deterministic dynamical systems, the (ε, τ) -entropy per unit time would converge to the Kolmogorov-Sinai entropy per unit time in the limit where ε goes to zero. Such dynamical entropies are the decay rates of the probabilities

$$P(\boldsymbol{\omega}) = P(\omega_0\omega_1\omega_2\dots\omega_{n-1}) \quad (47)$$

that the system follows given paths or histories $\boldsymbol{\omega} = \omega_0\omega_1\omega_2\dots\omega_{n-1}$ where the symbols ω_j are the coarse-grained states observed with the resolution ε at the successive times $t = j\tau$ with $j = 0, 1, 2, \dots, n - 1$. In Eq. (47), P denotes the stationary probability distribution of the process. Because of the temporal disorder, the probability of a typical path is known to decay exponentially at a rate defining the (ε, τ) -entropy per unit time [46]

$$h(\varepsilon, \tau) \equiv \lim_{n \rightarrow \infty} -\frac{1}{n\tau} \sum_{\boldsymbol{\omega}} P(\boldsymbol{\omega}) \ln P(\boldsymbol{\omega}) \quad (48)$$

In nonequilibrium steady states, we expect that the time-reversal symmetry is broken at the level of the invariant probability distribution so that a path $\boldsymbol{\omega} = \omega_0\omega_1\omega_2\dots\omega_{n-1}$ and its time reversal $\boldsymbol{\omega}^R = \omega_{n-1}\dots\omega_2\omega_1\omega_0$ should have different probabilities [34–38]

$$\text{out of equilibrium:} \quad P(\boldsymbol{\omega}) \neq P(\boldsymbol{\omega}^R) \quad (49)$$

Accordingly, the probability of a time-reversed path should decay at a rate which is different from the entropy per unit time (48). This observation motivates the introduction of the time-reversed (ε, τ) -entropy per unit time [28]

$$h^R(\varepsilon, \tau) \equiv \lim_{n \rightarrow \infty} -\frac{1}{n\tau} \sum_{\boldsymbol{\omega}} P(\boldsymbol{\omega}) \ln P(\boldsymbol{\omega}^R) \quad (50)$$

where the average is still carried out with the path probabilities themselves. If the average was performed with the time-reversed path probabilities in Eq. (50), we would recover the quantity (48) because the sum over the paths $\boldsymbol{\omega}$ is equivalent to the sum over their reversals $\boldsymbol{\omega}^R$. In this regard, the time-reversed entropy per unit time characterizes the temporal disorder of the time-reversed paths among the set of the typical paths of the forward process.

The remarkable result is that the difference between the time-reversed and the standard entropies per unit time is equal to the thermodynamic entropy production:

$$\frac{1}{k_B} \frac{d_i S}{dt} = \lim_{\varepsilon, \tau \rightarrow 0} [h^R(\varepsilon, \tau) - h(\varepsilon, \tau)] \geq 0 \quad (51)$$

as can be shown for several classes of nonequilibrium stochastic processes as well as in other frameworks [28, 36]. This fundamental connection has furthermore been verified experimentally for driven Brownian motion and RC electric circuits, providing evidence for the breaking of time-reversal symmetry in nonequilibrium fluctuations down to the nanoscale [30, 31].

The difference of entropies, $h^R - h$, is always non-negative in agreement with the second law of thermodynamics. At equilibrium, both entropies are equal meaning that the equilibrium temporal disorder looks the same for the typical paths and their time reversals, which is an expression of the principle of detailed balancing. In contrast, the time-reversed entropy per unit time is larger than the standard one if the system is driven out of equilibrium because the nonequilibrium constraints perform a selection of typical paths, whereupon the time-reversal symmetry is broken. The probabilities of the time-reversed paths decay faster than for the corresponding typical paths so that the time-reversed paths appear more random in this regard. We thus have the

Theorem of nonequilibrium temporal ordering: *In nonequilibrium steady states, the typical paths are more ordered in time than their time reversals in the sense that their temporal disorder characterized by h is smaller than the temporal disorder of the corresponding time-reversed paths characterized by h^R [29].*

This theorem expresses mathematically the fact that nonequilibrium systems manifest a directionality. For instance, the mean current flowing across a resistance goes downhill in the chemical potential landscape in spite of its upward or downward fluctuations. The farther away from equilibrium, the more regular the flow will look. In the limit of ballistic transport, the current is perfectly regular. This result applies to nonequilibrium nanosystems, showing the potentialities of evolving out of equilibrium to generate or process information at the nanoscale. In particular, Landauer's principle according to which the erasure of information generates thermodynamic entropy production can be deduced from the relationship (51) [72]. The consequences of these results for nanosystems will be discussed below.

G. Nanosystems driven by time-dependent forces

Fundamental results have also been obtained for systems driven by some time-dependent control parameter $\lambda(t)$ [11, 12]. Let us suppose that the dynamics is described by the Hamiltonian function $H(\mathbf{\Gamma}, \lambda)$. The work performed on the system while the control parameter varies from λ_A to λ_B is given by

$$W \equiv H(\mathbf{\Gamma}_B, \lambda_B) - H(\mathbf{\Gamma}_A, \lambda_A) \quad (52)$$

if $\mathbf{\Gamma}_A$ is the initial condition of the trajectory followed by the system. Therefore, the work is a random variable depending on the probability distribution of the initial conditions. Following Jarzynski [11], this initial probability distribution is taken as the canonical ensemble

$$p_A(\mathbf{\Gamma}_A) = \frac{1}{Z_A} e^{-\beta H(\mathbf{\Gamma}_A, \lambda_A)} \quad (53)$$

with the inverse temperature $\beta = (k_B T)^{-1}$. The free energy of the system in this initial canonical state is equal to $F_A = -k_B T \ln Z_A$. The probability density of the work performed on the system driven by the *forward protocol* while the control parameter $\lambda(t)$ varies as $\lambda_A \rightarrow \lambda_B$ is defined by

$$p_F(W) \equiv \langle \delta [W - (H_B - H_A)] \rangle_A \quad (54)$$

with $H_A = H(\mathbf{\Gamma}_A, \lambda_A)$ and $H_B = H(\mathbf{\Gamma}_B, \lambda_B)$.

A *reversed protocol* can be similarly defined by the reversed driving $\lambda_B \rightarrow \lambda_A$ with $\lambda(\mathcal{T} - t)$ from the other initial state

$$p_B(\mathbf{\Gamma}_B) = \frac{1}{Z_B} e^{-\beta H(\mathbf{\Gamma}_B, \lambda_B)} \quad (55)$$

at the same inverse temperature as in the canonical distribution (53). The work performed on the system submitted to this *reversed protocol* has the following probability distribution:

$$p_R(W) \equiv \langle \delta [W - (H_A - H_B)] \rangle_B \quad (56)$$

In this framework, the following theorem can be proved on the basis of Hamiltonian dynamics by using the Liouville theorem and the microreversibility [35]:

Crooks fluctuation theorem: *The probability densities of the work W performed on the system during the forward and reversed protocols have the universal ratio*

$$\frac{p_F(W)}{p_R(-W)} = e^{\beta(W - \Delta F)} \quad (57)$$

which only depends on the inverse temperature β , the work W itself, and the free energy difference $\Delta F = F_B - F_A$ between the thermodynamic equilibria at λ_B and λ_A [12].

This result has been verified in experiments on the unfolding of single RNA molecules [4].

A similar relation as Eq. (57) holds if the work is measured on n successive intermediate times $t_A = t_0 < t_1 < t_2 < \dots < t_{n-1} < t_n = t_B$. The multivariate probability density that the work takes given successive values is defined for the *forward protocol* as

$$p_F(W_1, W_2, \dots, W_n) \equiv \left\langle \prod_{j=1}^n \delta [W_j - (H_j - H_{j-1})] \right\rangle_A \quad (58)$$

and for the *reversed protocol* as

$$p_R(W_1, W_2, \dots, W_n) \equiv \left\langle \prod_{j=1}^n \delta [W_j - (H_{j-1} - H_j)] \right\rangle_B \quad (59)$$

with $H_j = H[\mathbf{\Gamma}(t_j), \lambda(t_j)]$. For these protocols, the fluctuation theorem reads

$$\frac{p_F(W_1, W_2, \dots, W_n)}{p_R(-W_1, -W_2, \dots, -W_n)} = e^{\beta(W_1 + W_2 + \dots + W_n - \Delta F)} \quad (60)$$

A consequence of Crooks' fluctuation theorem (57) is

Jarzynski's nonequilibrium work theorem: *The free energy difference $\Delta F = F_B - F_A$ between the thermodynamic equilibria at λ_B and λ_A can be evaluated in terms of the nonequilibrium work W by*

$$\langle e^{-\beta W} \rangle = e^{-\beta \Delta F} \quad (61)$$

where $\langle \cdot \rangle$ denotes the statistical average over an ensemble of random realizations of the forward protocol [11].

This theorem allows the measurement of free energy landscapes with single-molecule force spectroscopy [73]. Extensions to quantum systems have also been obtained [26, 27, 74, 75]. Moreover, Jarzynski's theorem implies Clausius' thermodynamic inequality:

$$\langle W \rangle \geq \Delta F \quad (62)$$

More recently, Kawai, Parrondo and Van den Broeck have shown [76] that the average value of the nonequilibrium work can be expressed as

$$\langle W \rangle = \Delta F + k_B T \int d\mathbf{\Gamma} p_F(\mathbf{\Gamma}, t) \ln \frac{p_F(\mathbf{\Gamma}, t)}{p_R(\mathbf{\Theta}\mathbf{\Gamma}, t)} \quad (63)$$

in terms of the phase-space probability distributions of the positions and momenta of the particles at some intermediate time t during the aforementioned protocol. We notice that the equality (63) of statistical mechanics completes Clausius' thermodynamic inequality (62).

The difference between the work W performed on the system and the free energy ΔF gained by the system is the work dissipated in the process: $W_{\text{diss}} \equiv W - \Delta F$. In this regard, Clausius' inequality (62) means that the average dissipated work is always non-negative, $\langle W_{\text{diss}} \rangle \geq 0$, which is a statement of the second law of thermodynamics. The last term of Eq. (63) thus provides an exact expression for the work dissipated in the process. If the time-dependent driving is such that a coupling is switched on between the nanosystem and reservoirs at different temperatures or chemical potentials over a long enough time interval \mathcal{T} for reaching a steady state, Eq. (63) can be used to obtain the entropy production in nonequilibrium steady states. The driving can be chosen to be time-reversal symmetric, $\lambda(t) = \lambda(\mathcal{T} - t)$, in order for the forward and reversed protocols to be identical. In such circumstances, the thermodynamic entropy production is given by

$$\frac{d_i S}{dt} = \frac{1}{T} \lim_{\tau \rightarrow \infty} \frac{1}{\mathcal{T}} \langle W_{\text{diss}} \rangle \geq 0 \quad (64)$$

On the other hand, the phase-space integral in Eq. (63) can be partitioned into the cells $C_{\omega_0 \omega_1 \dots \omega_{n-1}} = C_{\omega_0} \cap \Phi^{-\tau} C_{\omega_1} \cap \dots \cap \Phi^{-(n-1)\tau} C_{\omega_{n-1}}$ obtained by sampling the dynamics at the successive times $t = j\tau$ with $j = 0, 1, 2, \dots, n-1$. If these phase-space cells are supposed of volume $\Delta\mathbf{\Gamma}$, the probability densities in Eq. (63) give approximations for the stationary probabilities $P(\boldsymbol{\omega}) \simeq p_F(\mathbf{\Gamma}, t)\Delta\mathbf{\Gamma}$ and $P(\boldsymbol{\omega}^R) \simeq p_R(\mathbf{\Theta}\mathbf{\Gamma}, t)\Delta\mathbf{\Gamma}$ of the paths $\boldsymbol{\omega}$ and their reversals $\boldsymbol{\omega}^R$. In this way, the thermodynamic entropy production can be expressed as a relative entropy between path probabilities [77] and the relationship (51) is recovered, confirming that the thermodynamic entropy production finds its origin in the breaking of the time-reversal symmetry at the level of the probability distribution describing the nonequilibrium steady state.

In the following, selected studies of nonequilibrium nanosystems will be reviewed.

III. MECHANICAL NANOSYSTEMS

The mechanical systems considered in this section are Hamiltonian systems which conserve their total energy in the absence of external driving force.

A. Friction in double-walled carbon nanotubes

Carbon nanotubes have remarkable properties which have been systematically investigated since their discovery in 1991 [78]. They appear in the form of nested coaxial tubes called multiwalled carbon nanotubes (MWCNT), which can move relative to one another opening the possibility of fabricating mechanical devices at the nanoscale. The

relative sliding motion of nested carbon nanotubes was demonstrated in the experiment of Cumings and Zettl [79]. More recently, Fennimore *et al.* [80] and Bourbon *et al.* [81] used multiwalled carbon nanotubes as the shaft of rotary motors or actuators. In multiwalled carbon nanotubes, the different coaxial tubes interact with each other by the same van der Waals interactions as between graphene sheets in graphite. Whether the relative motion of nested nanotubes is translational or rotational, the mutual interaction between the nanotubes is the cause of friction and energy dissipation. This friction is a fundamental preoccupation in nanotribology, which requires the use of nonequilibrium statistical mechanics at the nanoscale, as explained here below.

We consider double-walled carbon nanotubes (DWCNT) [82–85]. Carbon nanotubes can have different geometries depending on the way the graphene sheet is rolled onto itself to form the nanotube. The different geometries are specified by the integers (n, m) with $0 \leq |m| \leq n$, which define the chiral vector $n\mathbf{a}_1 + m\mathbf{a}_2$ giving the equator of the nanotube in terms of the lattice vectors \mathbf{a}_1 and \mathbf{a}_2 of the hexagonal lattice of graphene. The diameter of the nanotube can be evaluated by

$$d = \frac{a}{\pi} \sqrt{n^2 + m^2 + nm} \quad (65)$$

with $a \simeq 2.5 \text{ \AA}$ [86]. The so-called armchair nanotubes correspond to the integers (n, n) , the zigzag ones to $(n, 0)$, and the chiral nanotubes to (n, m) with $n \neq m$ [86]. Double-walled carbon nanotubes are denoted as $(n_1, m_1)@(n_2, m_2)$ (see two examples in Fig. 1).

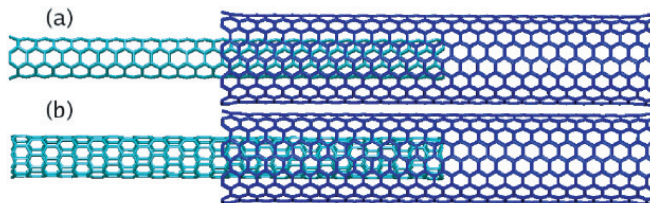


FIG. 1: (a) The armchair-armchair DWCNT $(4,4)@(9,9)$ with respectively $N_1 = 400$ and $N_2 = 900$ carbon atoms. (b) The zigzag-armchair DWCNT $(7,0)@(9,9)$ with $N_1 = 406$ and $N_2 = 900$. Both DWCNTs have outer diameter 13.2 \AA and length 61.5 \AA [83].

The carbon atoms within the inner or outer nanotube interact by Tersoff-Brenner potentials, $V_{\text{TB}}^{(1)}$ or $V_{\text{TB}}^{(2)}$ respectively [87]. The intertube potential is commonly modeled by the 6-12 Lennard-Jones potential

$$V_{\text{LJ}}(r) = 4\epsilon \left[\left(\frac{\sigma}{r} \right)^{12} - \left(\frac{\sigma}{r} \right)^6 \right] \quad (66)$$

with $\epsilon = 2.964 \text{ meV}$ and $\sigma = 3.407 \text{ \AA}$, which was successfully used to study C_{60} solids [88] and the sliding of nanotubes on graphite surface [89]. Accordingly, the total Hamiltonian describing a DWCNT can be written as

$$H = T^{(1)} + T^{(2)} + V_{\text{TB}}^{(1)} + V_{\text{TB}}^{(2)} + \sum_{i=1}^{N_1} \sum_{j=1}^{N_2} V_{\text{LJ}} \left(\|\mathbf{r}_i^{(1)} - \mathbf{r}_j^{(2)}\| \right) \quad (67)$$

where $T^{(1)}$ and $T^{(2)}$ are respectively the kinetic energies of the inner and outer nanotubes. The positions and momenta of the carbon atoms of both nanotubes are denoted by $\{\mathbf{r}_i^{(a)}\}_{i=1}^{N_a}$ and $\{\mathbf{p}_i^{(a)}\}_{i=1}^{N_a}$ with $a = 1$ (resp. $a = 2$) for the inner (resp. outer) tube. The kinetic energies are given by $T^{(a)} = \sum_{i=1}^{N_a} (\mathbf{p}_i^{(a)})^2 / (2m)$, where $m = 12 \text{ amu}$ is the mass of a carbon atom.

The molecular dynamics of the DWCNT system can be simulated by Hamilton's equations (2). The molecular dynamics conserves the total energy $E = H$, the total linear momentum, as well as the total angular momentum. The phase-space volumes are preserved according to Liouville's theorem. The molecular dynamics is carried out with a velocity Verlet algorithm with a time step of 2 fs . The total energy corresponds to room temperature of about $T = 300 \text{ K}$.

Within each nanotube, the carbon atoms undergo thermal fluctuations around their equilibrium position. Moreover, large amplitude motions are possible between the two nanotubes which interact with each other by an attractive van der Waals potential and constitute a mechanical oscillator if they form an isolated system. Molecular dynamics simulations reveal three different time scales characteristic of these motions [82, 83]:

- The time scale of the vibration of the carbon atoms around their equilibrium position is determined by the inverse of the Debye frequency of graphene: $t_C \simeq 50$ fs.
- The translational relative motion of the two nanotubes presents inertial oscillations with a period of about $t_P \simeq 10$ ps if the inner nanotube is initially extracted from the outer nanotube by a fraction of their common length.
- The relative sliding motion of the two nanotubes is damped by the dissipation of the energy contained in the relative motion. This dissipation is caused by dynamic friction between the nanotubes, resulting into a rise in temperature. The relaxation time of the inertial oscillations is of the order of $t_R \simeq 1000$ ps.

We notice that these time scales are separated from each other by several orders of magnitudes: $t_C \ll t_P \ll t_R$.

The sliding motion of the nanotubes can be translational or rotational. Although both types of motion can manifest themselves during a single simulation, their friction properties can be investigated separately.

1. Translational friction

The translational sliding motion of two nanotubes concerns the relative position r and velocity $v = \dot{r}$ between the nanotubes. The relative position can be defined as [83]

$$r(t) \equiv \mathbf{e}_{\parallel}(t) \cdot [\mathbf{R}^{(2)}(t) - \mathbf{R}^{(1)}(t)] \quad (68)$$

in terms of the centers of mass $\mathbf{R}^{(1)}$ and $\mathbf{R}^{(2)}$ of both nanotubes. The unit vector \mathbf{e}_{\parallel} points in the direction of the axis of the DWCNT and can be obtained by diagonalizing the inertia tensor of the total system and selecting the eigenvector associated with its smallest eigenvalue. This eigenvector slightly fluctuates around its initial orientation during the time evolution, which justifies its use to define the relative position by Eq. (68).

The relative position of the nanotubes admits a reduced description in terms of a Newtonian equation of Langevin type:

$$\mu \frac{d^2 r}{dt^2} = -\frac{dV_{\text{LJ}}(r)}{dr} + F_{\text{frict}} + F_{\text{fluct}}(t) \quad (69)$$

where $\mu = m(N_1^{-1} + N_2^{-1})^{-1}$ is the relative mass of the DWCNT system. The force in the right-hand side of Eq. (69) has three contributions.

The first contribution is the force of the V-shaped potential

$$V(r) = F\sqrt{r^2 + \ell^2} - C \simeq F|r| - C \quad (70)$$

due to the van der Waals interaction between the two nanotubes (see Fig. 2). This potential is obtained by averaging the interaction at fixed relative position r between the nanotubes. We notice the absence of corrugation because of the averaging. The V shape finds its origin in the proportionality of the interaction potential with the number of van der Waals bonds between the nanotubes. The potential is parabolic around its minimum because of thermal fluctuations around the configurations with the maximum number of bonds. If the energy of the relative motion is not too high, the potential forms a well in which the motion presents oscillations which would persist if dissipation could be neglected [90]. This inertial oscillator is anharmonic with a period of about $t_P \simeq 10$ ps.

The second contribution to the total force in Eq. (69) is the dynamic friction force:

$$F_{\text{frict}} = -\zeta \frac{dr}{dt} + O\left(\frac{dr}{dt}\right)^2 \quad (71)$$

with the friction coefficient ζ given by Kirkwood formula (17). The force-force correlation function decreases to zero over the time scale of vibration of the carbon atoms around their equilibrium position in graphene [82]. This time scale is determined by the inverse of the Debye frequency ω_D of graphene, i.e., $t_C \simeq 2\pi/\omega_D \simeq 50$ fs. According to the Kirkwood formula (17), the friction coefficient can be estimated to be $\zeta \simeq t_C \Delta F^2 / (2k_B T) = \pi \Delta F^2 / (\omega_D k_B T)$

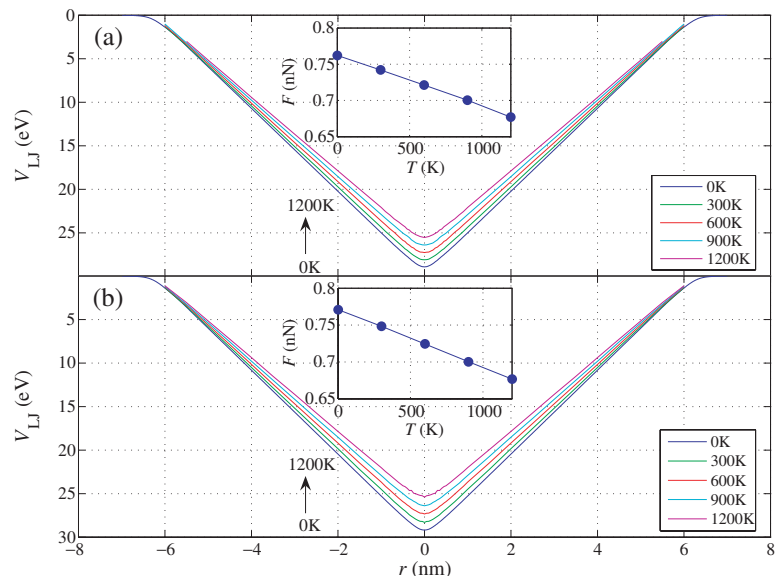


FIG. 2: Plot of the total Lennard-Jones potential V_{LJ} versus the distance r between the centers of mass of the nanotubes for (a) the armchair-armchair (4,4)@(9,9) and (b) the zigzag-armchair (7,0)@(9,9) DWCNTs [83]. The insets show that the force decreases with the temperature because of dilatation.

where ΔF is the standard deviation of the fluctuating intertube force. This latter increases with the temperature T approximately as $\Delta F \sim T$ so that the friction coefficient also increases as $\zeta \sim T$ [82].

The force-force correlation function should be evaluated by fixing the relative position r between the nanotubes. This is carried out by constrained molecular dynamics simulations [82, 83]. The constraint is enforced by modifying the force on all the atoms of each nanotube according to $\mathbf{F}_i^{(a)} \rightarrow \mathbf{F}_i^{(a)} - (1/N_a) \sum_{j=1}^{N_a} \mathbf{F}_j^{(a)}$. This modification has the required effect of canceling the acceleration of the centers of mass of each nanotube, while conserving the total energy E . This method gives the dependence of the friction coefficient on position as seen in Fig. 3 where we observe that the friction coefficient has a slow dependence on position, justifying that the friction coefficient is taken constant in Eq. (71) at the approximate value $\zeta \simeq 6$ amu/ps for the present case [83]. We notice that the friction coefficient also depends on properties affecting the intertube interaction, such as the distance between the nanotubes, the ends of the nanotubes, deformations, defects, or possible impurities composed of atomic species other than carbon.

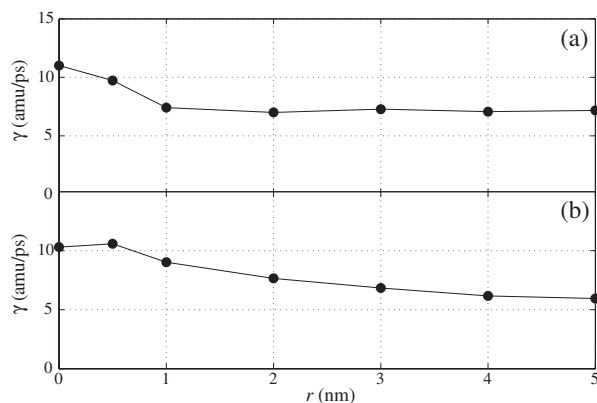


FIG. 3: Friction coefficient calculated by the Kirkwood formula (17) versus the relative position r between the nanotubes for: (a) the armchair-armchair (4,4)@(9,9) and (b) the zigzag-armchair (7,0)@(9,9) DWCNTs [83].

Although the dynamic friction force is proportional to the velocity at moderate sliding velocities, nonlinear dependences on the sliding velocity become important at larger velocities. These nonlinear effects appear in the form of resonances at specific values of the sliding velocity where dynamic friction is enhanced because of the excitation of

radial breathing modes of the outer nanotube. This phenomenon was first observed in the oscillatory system described here above [83], as well as in other systems where a finite inner nanotube moves at given sliding velocity inside an infinitely long outer nanotube [91]. This latter configuration allows a precise determination of the resonant velocities. If the nanotubes move at the relative velocity v , the spatial period $a = 2.5 \text{ \AA}$ of the corrugation of the intertube potential results into the periodic driving at the washboard frequency $\omega_{\text{wb}} = 2\pi v/a$. Resonances are thus possible when the washboard frequency ω_{wb} coincides with some vibration frequency. The vibration modes of the nanotubes and, in particular, of the outer tube form a spectrum of dispersion relations $\omega = \omega_i(k)$ characterizing the acoustic and optical phonons of each nanotube. Phonons of type i and wave number k are excited if the resonance condition $\omega_{\text{wb}} = \omega_i(k)$ is satisfied together with a further condition selecting the resonant values of the sliding velocity. This further condition can be shown to be given by the equality of the sliding velocity with the group velocity of the excited phonons: $v = d\omega_i(k)/dk$ [91]. More recently, a related phenomenon of chiral symmetry breaking has been discovered in the sliding dynamics of DWCNTs made of perfectly left-right symmetric and nonchiral nanotubes [92]. These phenomena of dynamic friction enhancement find their origin in the nonlinear dynamics of DWCNTs.

We notice that the DWCNT system is a weakly underdamped oscillator in the conditions investigated in Refs. [82–84]. Therefore, molecular dynamics simulations show many oscillations which are slowly damped because the friction coefficient is relatively small. Figure 4 depicts the amplitudes $R(t)$ of the successive oscillations during the relaxation. The results of molecular dynamics are compared with the prediction of the model (69) that these amplitudes are exponentially damped as $R(t) = R(0) \exp(-\Gamma_R t)$ with the damping rate $\Gamma_R = 2\zeta/(3\mu)$. The damping of the oscillations means that the energy of the one-dimensional sliding motion of the two nanotubes is dissipated in the many vibrational degrees of freedom of each nanotubes, which indeed undergo a rise in temperature from 300 K at the beginning of the simulation up to 338 K after relaxation.

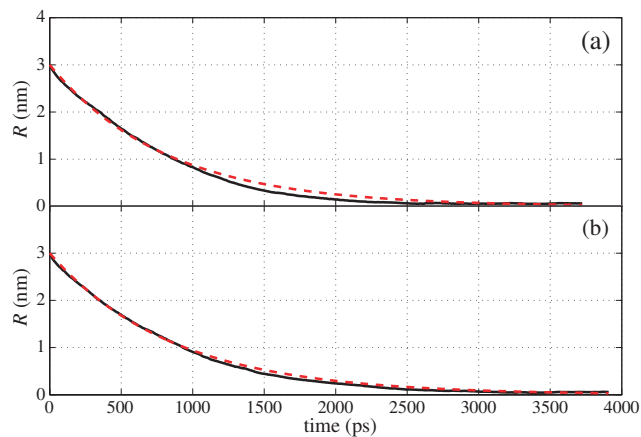


FIG. 4: Evolution of the amplitude of the damped oscillations for (a) the armchair-armchair (4,4)@(9,9) and (b) the zigzag-armchair (7,0)@(9,9) DWNTs [83]. The numerical results of molecular dynamics (solid lines) are compared with the theoretical expectation of the model (69) (dashed line).

The third contribution to the total force in Eq. (69) is the fluctuating Langevin force which is present as a corollary of dynamic friction force by the fluctuation-dissipation theorem. Accordingly, the Langevin force is taken as a Gaussian white noise satisfying

$$\langle F_{\text{fluct}}(t) \rangle = 0 \quad (72)$$

$$\langle F_{\text{fluct}}(t) F_{\text{fluct}}(t') \rangle = 2\zeta k_{\text{B}} T \delta(t - t') \quad (73)$$

for $|t - t'| \gg t_C$, in consistency with Kirkwood formula (17). As a consequence of the smallness of friction, the fluctuating force is also small and plays a significant role only after the large amplitude oscillations have been damped and no longer overwhelm thermal fluctuations in the relative motion between the nanotubes. The Langevin fluctuating force thus describes a state of thermodynamic equilibrium in the sliding motion. For the total system, this equilibrium state is microcanonical at the energy of the initial conditions of each molecular dynamics simulation. Since the total system has many degrees of freedom, $f = 3(N_1 + N_2) \simeq 3900$, the equilibrium statistical distribution of each degree of freedom is practically canonical at the temperature corresponding to the initial total energy. The equilibrium fluctuations of the relative position between the nanotubes remain very small of the order of a fraction of nanometer as seen in Fig. 5.

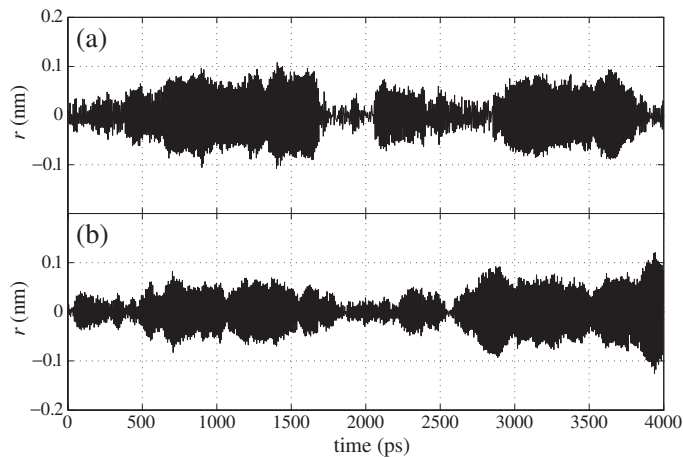


FIG. 5: Equilibrium fluctuating oscillations of the relative position between the nanotube mass centers for (a) the armchair-armchair (4,4)@(9,9) and (b) the zigzag-armchair (7,0)@(9,9) DWCNTs [83].

As explained in Sec. II A, the stochastic process described by the Langevin equation (69) admits an equivalent description in terms of a Fokker-Planck equation such as Eq. (18) for the probability density of the relative position and velocity between the two nanotubes:

$$\mathcal{P}(r, v, t) \equiv \int \delta[r - r(\mathbf{\Gamma})] \delta[v - v(\mathbf{\Gamma})] p(\mathbf{\Gamma}, t) d\mathbf{\Gamma} \quad (74)$$

This Fokker-Planck equation describes, in particular, the relaxation towards a state of equilibrium such as Eq. (20) [83]. This relaxation is characteristic of isolated systems with a few slow degrees of freedom coupled to baths of many fast degrees of freedom. The Poincaré recurrences back close to initial conditions are extremely long in an individual system, but they never occur in the statistical ensemble composed of infinitely many copies of the system described by the probability distribution $p(\mathbf{\Gamma}, t)$, if the dynamics has the ergodic property of mixing. Molecular dynamics shows that this property is practically fulfilled at a temperature of 300 K.

2. Rotational friction

Besides translational sliding motion, the two nanotubes may rotate relative to one another (see Fig. 6a). A friction property can be associated with this rotational motion [84], which is of importance in shafts of nanomachinery made of MWCNTs [80, 81]. For an isolated DWCNT, the total angular momentum is conserved. For long enough DWCNTs, the inner and outer nanotubes essentially rotate around a common axis with their respective angular velocities $\{\omega_1, \omega_2\}$ and angular momenta $\{L_1, L_2\}$. Under these circumstances, the rotational motion can be supposed to be one-dimensional and ruled by the coupled equations

$$\begin{cases} \frac{dL_1}{dt} = I_1 \frac{d\omega_1}{dt} = N_1 \\ \frac{dL_2}{dt} = I_2 \frac{d\omega_2}{dt} = N_2 = -N_1 \end{cases} \quad (75)$$

where I_a denote the moments of inertia around the common axis and N_a the torques acting on each nanotube. These torques are opposite by the conservation of the total angular momentum $L_1 + L_2$. The moment of inertia of a nanotube of radius R_a and length l is given by $I_a = 2\pi\sigma l R_a^3$ in terms of the surface mass density $\sigma = 4m/(3\sqrt{3}a_{CC}^2) \simeq 4.55 \text{ amu}/\text{\AA}^2$ where $m = 12 \text{ amu}$ is the atomic mass of carbon and $a_{CC} = 1.42 \text{ \AA}$ the carbon-carbon bond length in the hexagonal lattice of graphene.

Introducing the relative angular velocity and the angular velocity of the center of inertia as

$$\omega \equiv \omega_1 - \omega_2 \quad (76)$$

$$\Omega \equiv \frac{I_1\omega_1 + I_2\omega_2}{I_1 + I_2} \quad (77)$$

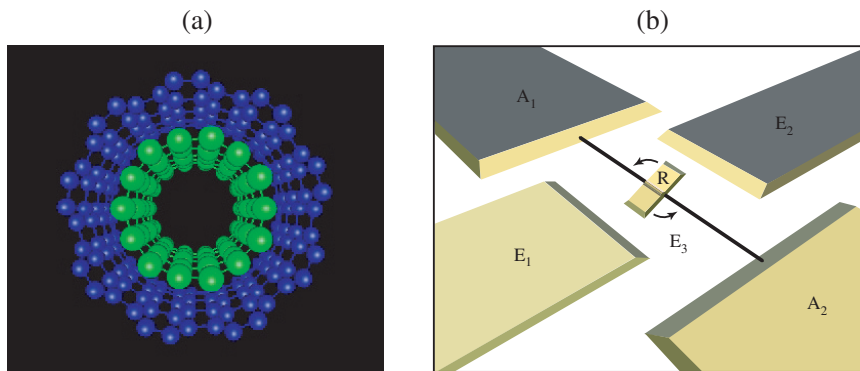


FIG. 6: (a) Coaxial view of a DWCNT showing that the outer nanotube can rotate around the inner nanotube as in the shaft of a rotary motor [82]. (b) Schematic picture of the rotary motor built in Berkeley [80]. The metal plate rotor R has a size of about 300 nm. It rotates around a shaft made of a MWCNT attached to its anchor pads (A_1 , A_2). The rotor is driven by an oscillating electric field between the electrodes E_1 , E_2 and E_3 (adapted from Ref. [80]).

the equations (75) become

$$\begin{cases} I \frac{d\omega}{dt} = N_1 \\ \frac{d\Omega}{dt} = 0 \end{cases} \quad (78)$$

with the relative moment of inertia $I \equiv (I_1^{-1} + I_2^{-1})^{-1}$.

The torque $N_1 = -N_2$ between the nanotubes is determined by the intertube van der Waals interaction. Since the rotation of one nanotube with respect to the other does not change the number of van der Waals bonds, the average potential is essentially flat with negligible corrugation as it is the case for translational motion. However, a dynamic friction torque proportional to the angular velocity and the corresponding Langevin fluctuating torque should be taken into account as in Eq. (69). Accordingly, the relative sliding rotation between the two nanotubes is described by the Langevin equation

$$I \frac{d\omega}{dt} = -\chi \omega + N_{\text{fluct}}(t) \quad (79)$$

where χ is the rotational friction coefficient and $N_{\text{fluct}}(t)$ is the Gaussian white noise

$$\langle N_{\text{fluct}}(t) \rangle = 0 \quad (80)$$

$$\langle N_{\text{fluct}}(t) N_{\text{fluct}}(t') \rangle = 2\chi k_B T \delta(t - t') \quad (81)$$

for $|t - t'| \gg t_C$ [84].

This stochastic model describes very well the molecular dynamics simulations [84]. If the relative angular velocity has a non-vanishing initial value, the sliding rotation is damped exponentially with the relaxation time $\tau = I/\chi$ until an equilibrium state is reached where the angle between the nanotubes undergoes a random walk of diffusion coefficient $D = k_B T/\chi$. The relaxation time is observed to behave as $\tau = \tau_\infty l/(l + l_0)$ in terms of the length l of the DWCNT and a constant l_0 of the order of the nanometer [84]. Hence, the relaxation time becomes independent of the length if the DWCNT is long enough. On the other hand, the relative moment of inertia is proportional to the length $I = 2\pi\sigma l(R_1^{-3} + R_2^{-3})^{-1}$ so that the friction coefficient is also proportional to the length of the DWCNT. This dependence has been shown to be consistent with the proportionality between the friction force and the intertube contact area [84]. Besides, the rotational friction coefficient is observed to increase with temperature as $\chi \sim T^\nu$ with the exponent $\nu = 1.53 \pm 0.04$ [84]. As for translational sliding motion, the isolated DWCNT is an undriven nonequilibrium system reaching a state of equilibrium after relaxation, because friction dissipates kinetic rotational energy.

The rotational friction is the cause of energy dissipation in rotary motors using a DWCNT or MWCNT shaft (see Fig. 6b). Such nanomotors have been fabricated by attaching a metal rotor plate to a single MWCNT suspended between two anchor pads, as carried out by the group of Berkeley [80]). The motor is controlled by voltages between

the rotor plate and three surrounding electrodes. All these components are integrated on a silicon chip, forming an electromechanical system with a rotor of about 300 nm and angular frequency of several Hertz. The fabrication of a similar system has been carried out in a collaboration between Paris and Lausanne [81]. Such nanoelectromechanical devices are driven nonequilibrium nanosystems where energy dissipation due to rotational friction is compensated by the electric energy supply.

B. Electromagnetic heating of microplasmas

1. The undriven system and its Hamiltonian

Microplasmas are small mechanical systems composed of atomic ions moving in a Penning trap [93–95]. Their spatial extension is in the range of micrometers [94]. These systems can be considered as isolated Hamiltonian systems in which energy is conserved, as long as the system is not subjected to a time-dependent driving. As for isolated DWCNTs, these systems undergo a relaxation towards a microcanonical equilibrium state if their initial conditions correspond to a given total energy. Remarkable crystalline-like configurations of the ions have been observed at low mean kinetic energy [93, 94]. These ordered configurations melt as their kinetic energy is increased (see Fig. 7). The dynamics is known to be chaotic with a spectrum of positive Lyapunov exponents [96].

In a frame rotating at the Larmor frequency associated with the magnetic field of the Penning trap, the Hamiltonian of the microplasma is given by

$$H_0 = \sum_a \left[\frac{1}{2} \mathbf{p}_a^2 + \left(\frac{1}{8} - \frac{\gamma^2}{4} \right) (x_a^2 + y_a^2) + \frac{\gamma^2}{2} z_a^2 \right] + \sum_{a < b} \frac{1}{r_{ab}}, \quad (82)$$

in terms of the momenta $\mathbf{p}_a = (p_{xa}, p_{ya}, p_{za})$ and the distances $r_{ab} = \sqrt{(x_a - x_b)^2 + (y_a - y_b)^2 + (z_a - z_b)^2}$ between the ions ($a, b = 1, 2, \dots, N$). The parameter γ controls the geometry of the trap. The trap is elongated or prolate if $0 < |\gamma| < (1/\sqrt{6})$, spherical if $|\gamma| = (1/\sqrt{6})$, and flat or oblate if $(1/\sqrt{6}) < |\gamma| < (1/\sqrt{2})$.

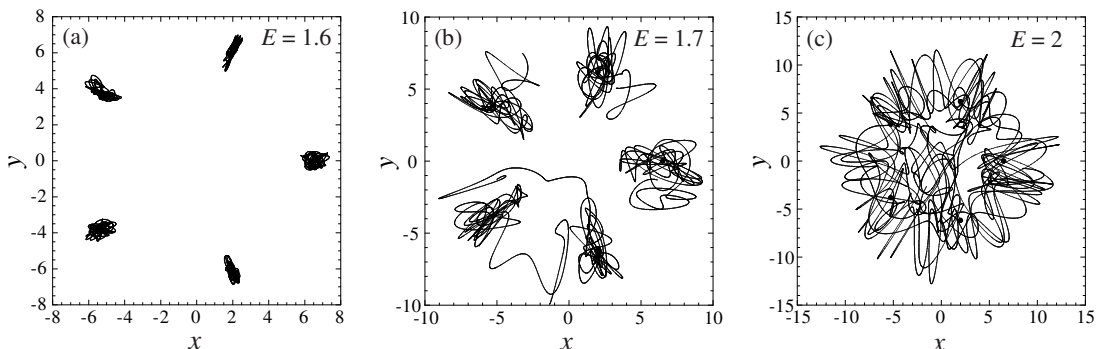


FIG. 7: Simulation of Hamiltonian trajectories of five atomic ions in an oblate Penning trap with $\gamma = 0.7$. The total angular momentum in the z -direction is vanishing. The total energy (82) is (a) $E = 1.6$, (b) $E = 1.7$, (c) $E = 2$.

2. The driven system and the fluctuation theorem

The microplasma can be heated if it interacts with an electromagnetic wave. In this case, the Hamiltonian becomes time dependent:

$$H = H_0 - A \sum_{a=1}^N z_a \sin \omega t \quad (83)$$

and Crooks fluctuation theorem (57) applies. In order that the forward protocol is identical with the reversed protocol, the driving is considered over a time interval with an odd number of half period, e.g., $\mathcal{T} = 3\pi/\omega$. In this case, the Hamiltonian (83) is the same at the beginning and the end of the driving so that the forward and reversed protocols

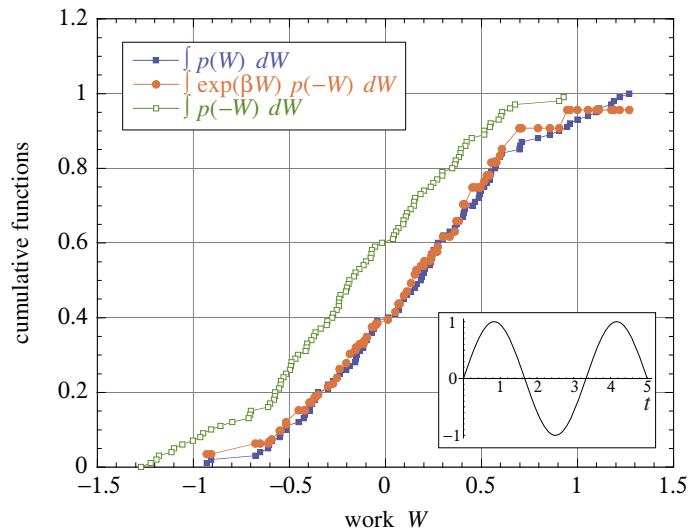


FIG. 8: Numerical verification of Crooks fluctuation theorem for a microplasma of five atomic ions in an oblate Penning trap with $\gamma = 0.7$ and heated by the time-dependent external field shown in inset over the time interval $\mathcal{T} = 3\pi/\omega = 5$. The verification of Crooks fluctuation theorem is the coincidence of the cumulative functions in the left-hand side (filled squares) and right-hand side (filled circles) of Eq. (84). The initial distribution is canonical with temperature $T = 1$. The final distribution is no longer canonical. The cumulative function of the negative values of the work (open circles) is shifted with respect to the other ones because of heating.

have the same probability distribution of nonequilibrium work, $p_F = p_R \equiv p$, and the difference of free energy is vanishing, $\Delta F = 0$. In this case, Crooks fluctuation theorem (57) can be expressed as

$$\int_{-\infty}^W p(W') dW' = \int_{-\infty}^W e^{\beta W'} p(-W') dW' \quad (84)$$

The numerical verification of this result is shown in Fig. 8 for a heated microplasma of five ions. The effect of heating is seen by the shift of the cumulative functions away from the mid-point at $W = 0$.

We notice that the quantum versions of the fluctuation theorem can also be applied to atoms, molecules, or ions trapped in quantum states, which might be of great interest for the control of quantum information devices and other ultracold systems.

IV. MECHANOCHEMICAL NANOSYSTEMS

A. F_1 -ATPase motor

F_1 -ATPase is the hydrophilic part of the F_0F_1 -ATPase also known as ATP synthase, which is an adenosine triphosphate (ATP) producing protein common to most living organisms [5]. *In vivo*, the two parts of ATP synthase, F_0 and F_1 , are attached to each other and mechanically coupled by the central γ -subunit. The F_0 part is embedded in the inner membrane of mitochondria and is rotating as a turbine when a proton current flows across the membrane. This turbine drives the rotation of the γ -subunit inside the hydrophilic F_1 part. This latter is composed of three α - and three β -subunits spatially alternated as a hexamer $(\alpha\beta)_3$ and forming a barrel for the rotation of the shaft made of the γ -subunit [97, 98]. Upon rotation, the γ -shaft induces conformational changes in the hexamer, leading to the synthesis of ATP in catalytic sites located in each β -subunit.

In their experimental work [99, 100], Kinosita and coworkers have succeeded to build a nanomotor by separating the F_1 part and attaching an actin filament or a colloidal bead to its γ -shaft (see Fig. 9). *In vitro*, ATP hydrolysis drives the rotation of this nanomotor, transforming chemical free energy from ATP into the mechanical motion of the γ -shaft. This motion proceeds in steps of 120° , revealing the three-fold symmetry of F_1 -ATPase [97–99]. The diameter of the F_1 -ATPase is 10 nm, which makes it one of the smallest motors in Nature with a tiny power of about 10^{-18} Watt.

The rotation of this nanomotor is powered by the chemical energy supplied by the hydrolysis of adenosine triphosphate (ATP) into adenosine diphosphate (ADP) and inorganic phosphate (P_i):



The thermodynamic force or affinity of this reaction is given by the difference of chemical potential $\Delta\mu$ between the three species:

$$\Delta\mu = \mu_{\text{ATP}} - \mu_{\text{ADP}} - \mu_{P_i} = \Delta\mu^0 + k_B T \ln \frac{[\text{ATP}]}{[\text{ADP}][P_i]} \quad (86)$$

where the concentrations are counted in mole per liter (M), T is the temperature, and k_B Boltzmann's constant. The Gibbs free energy of ATP hydrolysis takes the value $\Delta G^0 = -\Delta\mu^0 = -30.5 \text{ kJ/mol} = -7.3 \text{ kcal/mol} = -50 \text{ pN nm}$ at the temperature of 23°C , the external pressure of 1 atm, and pH 7 [101]. We notice that ATP hydrolysis provides a significant amount of free energy of $\Delta\mu^0 = -\Delta G^0 = 12.2 k_B T$ above the thermal energy $k_B T = 4.1 \text{ pN nm}$. At equilibrium where the chemical potential difference (86) vanishes, the concentrations of ATP, ADP, and P_i satisfy

$$\left. \frac{[\text{ATP}]}{[\text{ADP}][P_i]} \right|_{\text{eq}} = \exp \frac{\Delta G^0}{k_B T} \simeq 4.9 \cdot 10^{-6} \text{ M}^{-1} \quad (87)$$

showing that ATP tends to hydrolyze into its products. The motor is in a nonequilibrium state if the concentrations do not satisfy Eq. (87), whereupon its self-sustained rotation becomes possible thanks to the chemical free energy (86) supplied by the reaction.

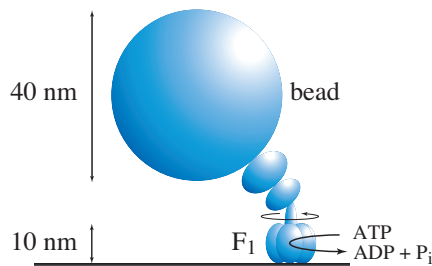
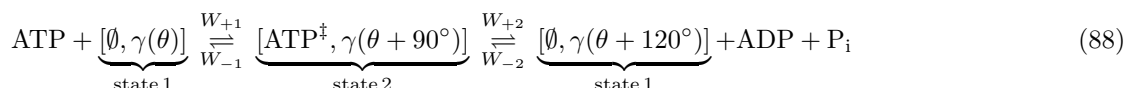


FIG. 9: Schematic representation of the F_1 -ATPase fixed on a surface and with a bead attached to its γ -shaft, as considered in the experiments of Ref. [100].

The motor is functioning along a cycle based on the following kinetic scheme. As reported in Ref. [100], the first substep, the 90° rotation of the γ -shaft, is induced by the binding of ATP to an empty catalytic site. The second substep, the 30° rotation of the γ -shaft, is induced by the release of ADP and P_i . The process can be summarized by the following chemical scheme



In the state 1, ATP can bind to an empty β -catalytic site \emptyset of F_1 with the γ -shaft at angular position θ . The binding of ATP fills this catalytic site and induces the 90° rotation of the γ -shaft from $\gamma(\theta)$ to $\gamma(\theta + 90^\circ)$. ATP^\ddagger stands for any transition state of ATP between the initial triphosphate molecule to the products of hydrolysis ADP and P_i before the evacuation of the β -catalytic site. The state 2 is thus denoted by $[\text{ATP}^\ddagger, \gamma(\theta + 90^\circ)]$. If the F_1 -ATPase proceeds to hydrolysis, the products ADP and P_i are released together, which induces the secondary 30° rotation and empties a β -subunit.

The nanomotor can be subjected to an external torque, for instance, coming from the proton turbine F_o . In a nonequilibrium steady state, the nanomotor has the mean rotation rate

$$V \equiv \frac{1}{2\pi} \left\langle \frac{d\theta}{dt} \right\rangle \quad (89)$$

in revolution per second and the mean ATP consumption rate

$$R \equiv \left\langle \frac{dN_{\text{ATP}}}{dt} \right\rangle = - \left\langle \frac{dN_{\text{ADP}}}{dt} \right\rangle = - \left\langle \frac{dN_{P_i}}{dt} \right\rangle \quad (90)$$

In this steady state, the thermodynamic entropy production is given by

$$\frac{d_i S}{dt} = \frac{2\pi\tau}{T} V + \frac{\Delta\mu}{T} R \geq 0 \quad (91)$$

in terms of the so-called thermodynamics forces or affinities, $2\pi\tau/T$ and $\Delta\mu/T$, and the corresponding fluxes or currents, V and R [102]. The two terms in the entropy production corresponds to the possibility of the coupling between the mechanical motion and the chemical reaction. It is thanks to this mechanochemical coupling that ATP is synthesized *in vivo* from the torque induced by the proton turbine F_o and the rotation of the nanomotor F_1 is powered *in vitro* by ATP hydrolysis. We notice that the mechanochemical coupling can be tight or loose depending on the regime of functioning of the nanomotor [103]. In order to further investigate the properties of the nanomotor, stochastic models have been proposed [104–107].

The modeling can be carried out at different levels of coarse graining. The finest level is certainly obtained by molecular dynamics following the phase-space trajectories of all the atoms of the motor and its environment with ATP, ADP and P_i molecules in water. A stochastic description is obtained by considering the reactive events of the kinetic scheme (88) as random events happening upon the random arrival and exit of ATP, ADP or P_i molecules into or out of the catalytic sites of the nanomotor. These reactive events correspond to transitions between the different chemical states of the motor. Since the three catalytic sites can be either occupied or unoccupied, there is a minimum of six states for the motor, which corresponds to the two states of Eq. (88) for a single catalytic site. On the other hand, the γ -shaft takes an angle θ with respect to the barrel. In each chemical state, this angle moves in a free-energy potential. Since the motor is nanometric, this motion is affected by the thermal fluctuations and is thus similar to a rotational Brownian motion driven by the torque induced by the conformational changes of the barrel. This suggests a continuous-state description in terms of Fokker-Planck equations for this Brownian motion of the angle θ in a free-energy potential corresponding to each chemical states of the motor. These Fokker-Planck equations should be coupled together by the transitions due to the chemical reactions [104, 105]. If the motor has six chemical states, the continuous-state model is thus defined by six coupled Fokker-Planck equations of diffusion-reaction type [106].

However, if the free-energy potentials present important wells and the time intervals to reach these wells are short compared to the dwell times, the angle θ can be supposed to jump between discrete values corresponding to the minima of the potential wells, neglecting the thermal fluctuations of the angle θ around these minima. Under these circumstances, a discrete-state description is appropriate, which further simplifies the modeling [107]. Nevertheless, this simplification carries an assumption of tight coupling between the mechanics and the chemistry of the motor. Indeed, a discrete-state model in which the different angles of the shaft uniquely correspond to the different chemical states of the motor supposes a tight coupling. This is not the case in the continuous-state description where the angle can take several possible values notwithstanding the chemical state. Accordingly, the comparison between both descriptions is interesting in order to determine the regimes of loose or tight coupling [103]. This distinction is important because the chemical and mechanical efficiencies depend on the quality of the mechanochemical coupling.

B. Continuous-state description

In the continuous-state model [106], the system is found at a given time t in one out of six chemical states $\sigma = 1, 2, \dots, 6$ and the γ -shaft at an angle $0 \leq \theta < 2\pi$. There are six chemical states because the three β -subunits can be either empty or occupied by a molecule of ATP or by the products ADP and P_i of hydrolysis. Consequently, the system is described by six probability densities $p_\sigma(\theta, t)$ normalized according to $\sum_{\sigma=1}^6 \int_0^{2\pi} p_\sigma(\theta, t) d\theta = 1$. The time evolution of the probability densities is ruled by a set of six Fokker-Planck equations coupled together by the terms describing the random jumps between the chemical states σ due to the chemical reactions of ATP binding and of the release of the products ADP and P_i with their corresponding reversed reactions [106]:

$$\partial_t p_\sigma(\theta, t) + \partial_\theta J_\sigma(\theta, t) = \sum_{\rho=1,2} \sum_{\sigma'(\neq\sigma)} [p_{\sigma'}(\theta, t) w_{\rho,\sigma'\rightarrow\sigma}(\theta) - p_\sigma(\theta, t) w_{-\rho,\sigma\rightarrow\sigma'}(\theta)] \quad (92)$$

where the probability current densities are given by

$$J_\sigma(\theta, t) = -D \partial_\theta p_\sigma(\theta, t) + \frac{1}{\zeta} [-\partial_\theta U_\sigma(\theta) + \tau] p_\sigma(\theta, t) \quad (93)$$

The diffusion coefficient D is expressed in terms of the friction coefficient ζ according to Einstein's relation $D = k_B T / \zeta$. The friction coefficient ζ can be evaluated for a bead of radius r attached off-axis at a distance $x = r \sin \alpha$ from the rotation axis according to

$$\zeta = 2\pi\eta r^3 (4 + 3 \sin^2 \alpha) \quad (94)$$

with the water viscosity $\eta = 10^{-9}$ pN s nm $^{-2}$ and $\alpha = \pi/6$ [101, 106].

When the motor is in the chemical state σ , the γ -shaft is subjected to the external torque τ and the internal torque $-\partial_\theta U_\sigma$ due to the free-energy potential $U_\sigma(\theta)$ of the motor with its γ -shaft at the angle θ . Applying an external torque to the motor has the effect of tilting the potentials into $U_\sigma(\theta) - \tau\theta$, which eases the rotation or makes it harder, depending on the sign of τ . These free-energy potentials have been fitted to experimental data and are depicted in Fig. 10 together with the potentials associated with the transition states of the reactions. We notice that these potentials generate power strokes if their variations are large with respect to the thermal energy $k_B T$, which is here the case except at the bottom of the potential wells where thermal fluctuations dominate.

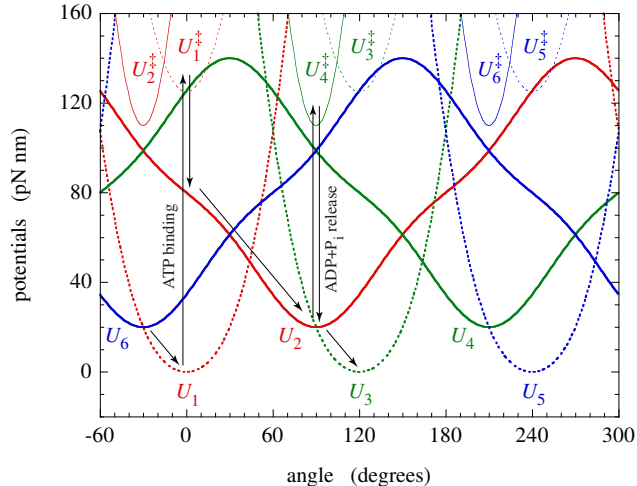


FIG. 10: The potentials of the chemical states $U_\sigma(\theta)$ and of the transition states $U_\sigma^\ddagger(\theta)$ with a schematic representation of the transitions between them during the motor cycle [106]. Because of the three-fold symmetry of the F₁ motor the different potentials are given by $U_1(\theta) = U(\theta)$, $U_3(\theta) = U(\theta - 2\pi/3)$, $U_5(\theta) = U(\theta - 4\pi/3)$, $U_2(\theta) = \tilde{U}(\theta)$, $U_4(\theta) = \tilde{U}(\theta - 2\pi/3)$, and $U_6(\theta) = \tilde{U}(\theta - 4\pi/3)$ in terms of only the two potentials $U(\theta)$ and $\tilde{U}(\theta)$ corresponding to the empty and occupied catalytic sites. A similar symmetry reduction holds for the transition states.

The transition rates $w_{\rho,\sigma' \rightarrow \sigma}(\theta)$ of the reactions are given by [106]

$$w_+(\theta) = k_0 [\text{ATP}] \exp \left\{ -\beta [U^\ddagger(\theta) - U(\theta) - G_{\text{ATP}}^0] \right\} \quad (95)$$

$$w_-(\theta) = k_0 \exp \left\{ -\beta [U^\ddagger(\theta) - \tilde{U}(\theta)] \right\} \quad (96)$$

$$\tilde{w}_+(\theta) = \tilde{k}_0 \exp \left\{ -\beta \left[\tilde{U}^\ddagger(\theta) - \tilde{U} \left(\theta + \frac{2\pi}{3} \right) \right] \right\} \quad (97)$$

$$\tilde{w}_-(\theta) = \tilde{k}_0 [\text{ADP}] [\text{P}_i] \exp \left\{ -\beta \left[\tilde{U}^\ddagger(\theta) - U(\theta) - G_{\text{ADP}}^0 - G_{\text{P}_i}^0 \right] \right\} \quad (98)$$

in terms of the concentrations of ATP, ADP, and P_i molecules in the solution surrounding the nanomotor and the free-energy potentials $U(\theta)$ and $\tilde{U}(\theta)$ for the wells and the potentials $U^\ddagger(\theta)$ and $\tilde{U}^\ddagger(\theta)$ for the transition states. Equations (95)-(98) represent, respectively, the transition rates of binding and unbinding of ATP, and of unbinding and binding of ADP and P_i to the first β -subunit. The other transition rates are obtained by 120° rotations of the rates (95)-(98) in order to reproduce the threefold symmetry of F₁-ATPase. We notice that the system has the threefold rotational symmetry but no reflection symmetry, which is to be attributed to the chirality of the supramolecular architecture of the F₁ molecular motor and is essential for its unidirectional rotation in the presence of its chemical fuel.

The stochastic process ruled by the Fokker-Planck equations (92) can be simulated by Gillespie's algorithm [57, 58], which provides realistic random trajectories as shown in Fig. 11. The rotation proceeds by rapid jumps due to the power strokes generated after each reactive event by the free-energy potentials of Fig. 10. Between two successive jumps, the angle undergoes thermal fluctuations around the minima of the potential wells of Fig. 10. In this respect, the shaft performs a random motion with a mean rotation rate fixed by the chemical concentrations of ATP, ADP, and P_i. For vanishing concentrations of the products of ATP hydrolysis, the mean rotation rate depends on ATP concentration in a way characteristic of a typical Michaelis-Menten kinetics:

$$V \simeq \frac{V_{\text{max}} [\text{ATP}]}{[\text{ATP}] + K_{\text{M}}} \quad (99)$$

with the constant $K_M \simeq 16 \mu\text{M}$, as depicted in Fig. 12. At low ATP concentration, the rotation rate increases with ATP concentration. However, the rate saturates at the maximum value $V_{\text{max}} \simeq 130 \text{ rev/s}$ at high ATP concentration where the speed of the motor is limited by the time scale of the release of the products, ADP and P_i .

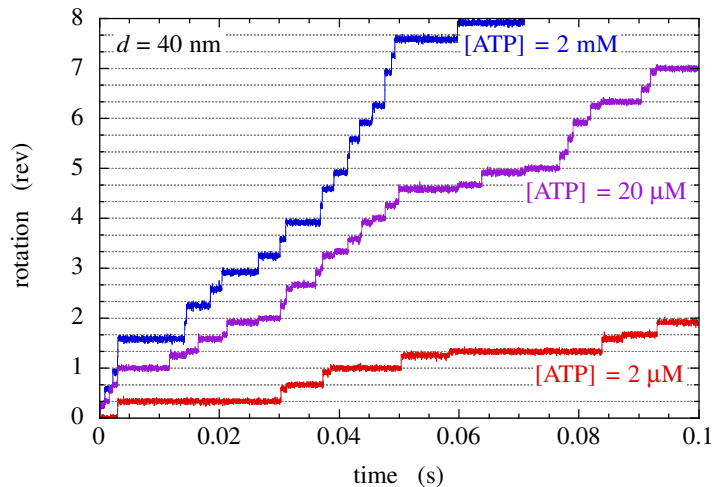


FIG. 11: Stochastic trajectories of the rotation of the γ -shaft of the F_1 motor [106]. The number of revolutions $\theta(t)/2\pi$ is plotted versus time t in seconds for $[\text{ATP}] = 2 \mu\text{M}$, $20 \mu\text{M}$, 2mM , and $[\text{ADP}][\text{P}_i] = 0$. The diameter of the bead is $d = 40 \text{ nm}$. The temperature is of 23 degrees Celsius. The external torque is zero. This figure is to be compared with Fig. 4 of Ref. [100].

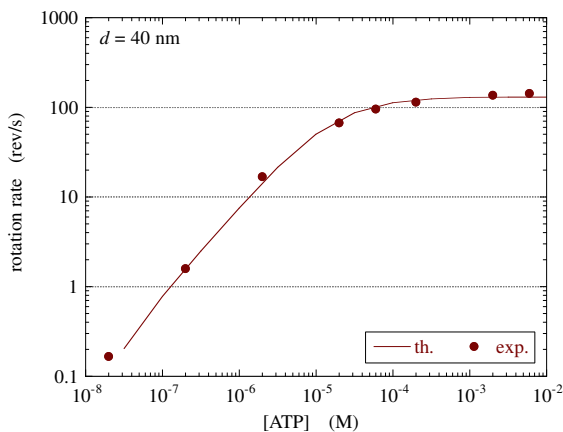


FIG. 12: Mean rotation rate of the γ -shaft of the F_1 motor in revolutions per second, versus ATP concentration in mole per liter for $[\text{ADP}][\text{P}_i] = 0$ [106]. The diameter of the bead is $d = 40 \text{ nm}$. The temperature is of 23 degrees Celsius. The external torque is zero. The circles are the experimental data [100]. The solid line is the result of the present model.

In order to determine the regimes of loose and tight couplings between the chemistry and the mechanics of the F_1 motor, both the rotation rate V and the ATP consumption rate R have been simulated with the continuous-angle model (92) for different values of the external torque τ and chemical potential difference $\Delta\mu$, which are the corresponding affinities. Figure 13 depicts the plane $(\tau, \Delta\mu)$ with the curves where either the rotation stops, $V = 0$, or the ATP consumption rate vanishes, $R = 0$. The value of the external torque where the rotation stops is called the stalling torque. The two curves $V = 0$ and $R = 0$ intersects at the origin $(\tau = 0, \Delta\mu = 0)$ which is the thermodynamic equilibrium point. We notice that the curve $V = 0$ is above the curve $R = 0$ in the plane of the chemical potential difference $\Delta\mu$ versus the torque as it should be in order to satisfy the second law of thermodynamics (91).

We observe that the two curves $V = 0$ and $R = 0$ are very close to each other if the external torque is larger than about -30 pN nm . In this regime, the following condition is satisfied:

$$\text{tight coupling:} \quad V = \frac{1}{3} R \quad (100)$$

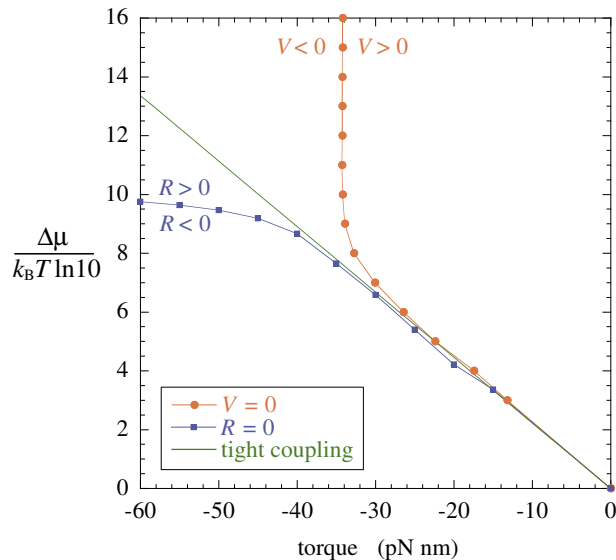


FIG. 13: Chemical potential difference $\Delta\mu$ in units of $k_B T \ln 10$ versus the external torque τ for the situations where the rotation rate V (circles) and the ATP consumption rate R (squares) vanish in the continuous model (92) [107]. The straight line $\Delta\mu = -2\pi\tau/3$ where the chemomechanical affinity (101) vanishes, $A = 0$, is drawn for comparison. The concentrations are fixed according to $[\text{ATP}] = 4.9 \cdot 10^{0.8a-11}$ M and $[\text{ADP}][\text{P}_i] = 10^{-0.2a-5}$ M, in terms of the quantity $a = \Delta\mu / (k_B T \ln 10)$. The bead attached to the γ -shaft has the diameter $d = 2r = 80$ nm and the temperature is of 23 degrees Celsius. The torque where $V = 0$ is called the stall torque. The determination of the curves $V = 0$ and $R = 0$ is difficult close to the thermodynamic equilibrium point ($\tau = 0, \Delta\mu = 0$) because both the rotation rate V and the ATP consumption rate R are very small in this region, which explains the absence of dots close to the origin.

for which one revolution is driven by the hydrolysis of three ATP molecules. In the tight-coupling regime, there remains a single independent current and its associated affinity defined as [107]

$$A \equiv \underbrace{\frac{2\pi}{3} \frac{\tau}{k_B T}}_{\text{mechanics}} + \underbrace{\frac{\Delta\mu}{k_B T}}_{\text{chemistry}} \quad (101)$$

Consequently, the thermodynamic entropy production (91) becomes

$$\text{tight coupling:} \quad \frac{1}{k_B} \frac{d_i S}{dt} = A R \geq 0 \quad (102)$$

which vanishes under the condition $\Delta\mu = -2\pi\tau/3$, as observed in Fig. 13 for $-30 \text{ pN nm} < \tau < 0$.

Beyond this regime, the free-energy potentials $U_\sigma(\theta) - \tau\theta$ are so much tilted by the external torque τ that the rotation can proceed independently of the reaction and the coupling becomes loose [106]. We thus recover two independent currents and affinities in the loose-coupling regime.

Chemical and mechanical efficiencies can be introduced for such molecular motors [102]. In the regime of ATP synthesis under a negative external torque, the ATP consumption rate as well as the rotation rate are negative, $R < 0$ and $V < 0$. In this regime, a chemical efficiency can be defined as the ratio of the free energy stored in the synthesized ATP over the mechanical power due to the external torque [102]

$$\eta_c \equiv -\frac{\Delta\mu R}{2\pi\tau V} \quad (103)$$

such that $0 \leq \eta_c \leq 1$. In the regime where the rotation is powered by ATP, a mechanical efficiency can be defined as the inverse of the chemical efficiency [102]

$$\eta_m \equiv -\frac{2\pi\tau V}{\Delta\mu R} \quad (104)$$

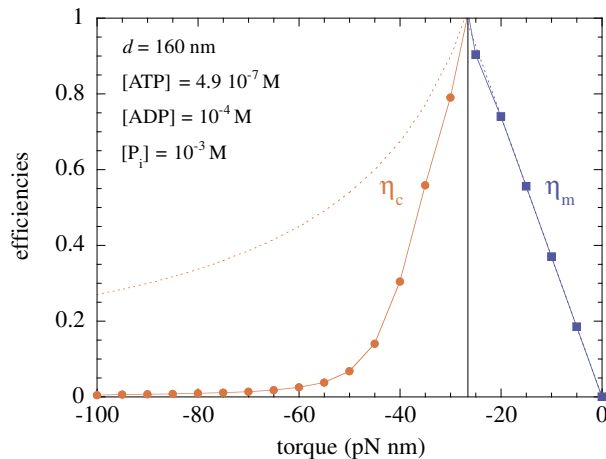


FIG. 14: Chemical efficiency (103) and mechanical efficiency (104) versus the external torque τ in the continuous-state model (respectively circles and squares joined by a solid line) and compared with the prediction (105) of tight coupling (dashed lines) [107]. The vertical solid line indicates the stalling torque at $\tau = \tau_{\text{stall}} = -27.0$ pN nm. The concentrations are $[\text{ATP}] = 4.9 \cdot 10^{-7}$ M, $[\text{ADP}] = 10^{-4}$ M, and $[\text{P}_i] = 10^{-3}$ M. The diameter of the bead is $d = 2r = 160$ nm and the temperature of 23 degrees Celsius. The predictions of tight coupling (dashed lines) are respectively $\eta_c = \tau_{\text{stall}}/\tau$ for $\tau < \tau_{\text{stall}}$, and $\eta_m = \tau/\tau_{\text{stall}}$ for $\tau_{\text{stall}} < \tau < 0$, with $\tau_{\text{stall}} = -27.0$ pN nm.

The mechanical efficiency satisfies $0 \leq \eta_m \leq 1$ in the regime where the external torque is negative while both the rotation rate and the ATP consumption rates are positive, $V > 0$ and $R > 0$. Both efficiencies are depicted in Fig. 14 and compared with the values

$$\text{tight coupling: } \eta_c = \frac{1}{\eta_m} = -\frac{3\Delta\mu}{2\pi\tau} \quad (105)$$

expected from the tight-coupling conditions (100). This plot confirms that the nanomotor is functioning above the stalling torque in the tight-coupling regime and below in a loose-coupling regime. The efficiencies can nearly reach unit values around the stalling torque where the rotational motion of the motor is very slow and nearly adiabatic.

C. Discrete-state description

In the tight-coupling regime, the rotation of the shaft is directly driven by each reactive event, which justifies the modeling of the stochastic process by a master equation for the probabilities to find the motor in each one of its different chemical states [107]

$$\frac{dP_\sigma(t)}{dt} = \sum_{\rho, \sigma'} [P_{\sigma'}(t) W_{+\rho}(\sigma'|\sigma) - P_\sigma(t) W_{-\rho}(\sigma|\sigma')] \quad (106)$$

with a sum over the reactions ρ and the chemical states σ' before the transition $\sigma' \xrightarrow{\rho} \sigma$ or after the reverse transition $\sigma \xrightarrow{-\rho} \sigma'$. The master equation conserves the total probability $\sum_\sigma P_\sigma(t) = 1$ for all times t .

The discrete-state model (106) can in principle be obtained by coarse graining the continuous-state model (92). Since the discrete states correspond to the angular intervals $\theta_\sigma < \theta < \theta_\sigma + 2\pi/3$ where the γ -shaft spends most of its time while in the chemical state σ , the probabilities ruled by the master equation (106) are related to the probability densities of the continuous-state description (92) according to

$$P_\sigma(t) = \int_{\theta_\sigma}^{\theta_\sigma + 2\pi/3} p_\sigma(\theta, t) d\theta \quad (107)$$

This method would in general lead to a non-Markovian master equation. In the case where there is a net separation of time scales between the dwell times and the jump times between the discrete states, the non-Markovian effects may be negligible and a description in terms of a Markovian equation such as the master equation (106) may be obtained. This is the situation we now consider.

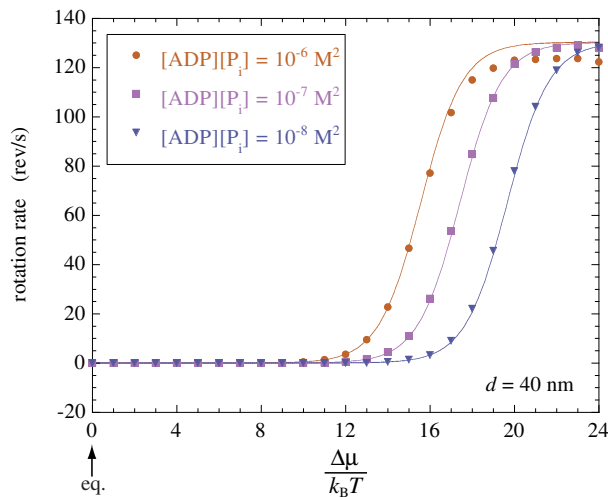


FIG. 15: Mean rotation rate versus the affinity (101) for a zero external torque, in which case the affinity is equal to the chemical potential difference $\Delta\mu$ in units of the thermal energy $k_B T$ [107]. The thermodynamic equilibrium corresponds to $\Delta\mu = 0$. The ATP concentration is given in terms of the chemical potential difference by $[\text{ATP}] = [\text{ADP}][\text{P}_i] \exp[(\Delta\mu - \Delta\mu^0)/(k_B T)] \simeq 4.9 \cdot 10^{-6} \text{ M}^{-1} [\text{ADP}][\text{P}_i] \exp[\Delta\mu/(k_B T)]$ since $\Delta\mu^0 = -\Delta G^0 = 50 \text{ pN nm}$. The results of the discrete model (solid lines) are compared with the continuous model (dots) for three different values of $[\text{ADP}][\text{P}_i]$. The diameter of the bead is $d = 2r = 40 \text{ nm}$ and the temperature 23 degrees Celsius.

The quantities $W_\rho(\sigma'|\sigma)$ are the transition rates per unit time from the state σ' to the state σ due to the reaction ρ . According to the mass-action law of chemical kinetics, the reaction rates W_ρ in Eq. (88) depend on the molecular concentrations in the solution surrounding the motor as follows [107]

$$W_{+1} = k_{+1}[\text{ATP}] \quad (108)$$

$$W_{-1} = k_{-1} \quad (109)$$

$$W_{+2} = k_{+2} \quad (110)$$

$$W_{-2} = k_{-2}[\text{ADP}][\text{P}_i] \quad (111)$$

where the quantities k_ρ ($\rho = \pm 1, \pm 2$) are the constants of the forward and backward reactions of binding and unbinding of ATP or ADP with P_i while $[\text{ATP}]$, $[\text{ADP}]$, and $[\text{P}_i]$ represent the concentrations of these species. k_{+1} is the constant of ATP binding, k_{-1} the ATP unbinding constant, k_{+2} the constant of ATP synthesis, and k_{-2} the constant of product release. These constants can be fitted to data from experiments or numerical simulations of the continuous-state model. In this latter case, we notice that the reaction constants are effective constants which depend on the external torque and are not identical with those entering the definition of the continuous-state model [107].

An advantage of the discrete-state model is that its solutions can be obtained analytically [107]. In a stationary state, the mean rotation and ATP consumption rates are given by [107]

$$V = \frac{V_{\max} ([\text{ATP}] - K_{\text{eq}}[\text{ADP}][\text{P}_i])}{[\text{ATP}] + K_M + K_P[\text{ADP}][\text{P}_i]} = \frac{1}{3} R \quad (112)$$

in terms of the constants

$$V_{\max} \equiv \frac{1}{3} k_{+2} \quad (113)$$

$$K_M \equiv \frac{k_{-1} + k_{+2}}{k_{+1}} \quad (114)$$

$$K_P \equiv \frac{k_{-2}}{k_{+1}} \quad (115)$$

$$K_{\text{eq}} \equiv \frac{k_{-1}k_{-2}}{k_{+1}k_{+2}} = \exp \frac{1}{k_B T} \left(\Delta G^0 - \frac{2\pi}{3} \tau \right) \simeq 4.9 \cdot 10^{-6} \text{ M}^{-1} \exp \left(-\frac{2\pi}{3} \frac{\tau}{k_B T} \right) \quad (116)$$

We recover the Michaelis-Menten kinetics (99) for vanishing concentrations of ADP or P_i . An important observation is that the mean rotation and ATP consumption rates – which are the nonequilibrium fluxes of the nanomotor – both

have a highly nonlinear dependence on the thermodynamic force or affinity (101) driving the motor out of equilibrium. This mechanochemical affinity allows us to express the ATP concentration as

$$[\text{ATP}] = K_{\text{eq}}[\text{ADP}][\text{P}_i] e^A \quad (117)$$

The state of thermodynamic equilibrium thus corresponds to the vanishing of the affinity (101) as it should. Substituting Eq. (117) into Eq. (112), we obtain the following expression for the mean rotation rate [107]

$$V = \frac{V_{\text{max}} (e^A - 1)}{e^A - 1 + \frac{3V_{\text{max}}}{L}} \quad (118)$$

where the coefficient L depends on the concentrations of ADP and P_i as well as the constants (113)-(116) and controls the linear response of the molecular motor because

$$V \simeq \begin{cases} \frac{1}{3}LA & \text{for } A \ll 1 \\ V_{\text{max}} & \text{for } A \gg 1 \end{cases} \quad (119)$$

The analytic form (118) shows that the rotation rate depends on the thermodynamic force A in a highly nonlinear way, in contrast to what is often supposed. The nonlinear dependence is very important as observed in Fig. 15. The linear regime extends around the thermodynamic equilibrium point at $\Delta\mu = 0$ where the function $V(A)$ is essentially flat because the linear-response coefficient takes the very small value $L \simeq 10^{-5} \text{ s}^{-1}$. Since the affinity is about $A \simeq 21.4$ under the physiological conditions $[\text{ATP}] \simeq 10^{-3} \text{ M}$, $[\text{ADP}] \simeq 10^{-4} \text{ M}$, and $[\text{P}_i] \simeq 10^{-3} \text{ M}$ [101], the rotation rate would take the extremely low value $V \simeq LA/3 \simeq 6.5 \text{ rev/day}$ if the motor was functioning in the linear regime. Remarkably, the nonlinear dependence of Eq. (118) on the affinity A allows the rotation rate to reach the maximum value $V_{\text{max}} \simeq 130 \text{ rev/s}$ under physiological conditions.

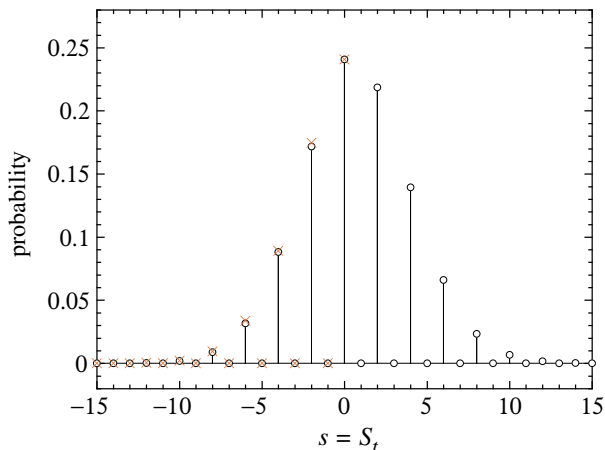


FIG. 16: Probability $P(S_t = s)$ (open circles) that the F_1 motor performs $s = S_t$ substeps during the time interval $t = 10^4 \text{ s}$ compared with the expression $P(S_t = -s) e^{sA/2}$ (crosses) expected from the fluctuation theorem for $[\text{ATP}] = 6 \cdot 10^{-8} \text{ M}$ and $[\text{ADP}][\text{P}_i] = 10^{-2} \text{ M}^2$ [110].

The fluctuation theorem of Subsection IID can be verified from the statistics of the random forward and backward substeps undergone by the γ -shaft of the F_1 motor, a full revolution corresponding to six substeps [110]. The graph associated with the stochastic process has six vertices simply connected as the edges of a hexagon. There is thus a single independent current or flux because of the tight coupling between the mechanical rotation and the chemistry. According to Eq. (40), we should thus expect the following fluctuation relation

$$\frac{P(S_t = +s)}{P(S_t = -s)} = e^{As/2} \quad (120)$$

for the probability $P(S_t = s)$ that the nanomotor performs $s = S_t$ substeps over the time interval t . The quantity A is the affinity (101) for a zero external torque $\tau = 0$.

Figure 16 shows that the fluctuation relation (120) is indeed satisfied [110]. As seen in Fig. 16, the probability distribution of the displacements here takes a specific form where the odd displacements are almost never occurring.

Indeed, for the values of the chemical concentrations considered in Fig. 16, the probability to be on odd sites is about four orders of magnitude lower than the probability to be on even sites. Therefore, the system almost never stays on odd site and immediately jumps to the next or previous sites. We notice that the backward substeps of the motor are here possible because the concentrations are close to chemical equilibrium. Under physiological conditions, the motor is already far enough from equilibrium that the backward rotations become very improbable.

The theorem of nonequilibrium temporal ordering stated in Subsection IIF also applies to the molecular motor, showing that their motion is more ordered out of equilibrium than at equilibrium. If the motion of the shaft of the F_1 rotary motor was recorded with the integers $\omega \in \{1, 2, 3\}$ corresponding to the three main steps, a stochastic trajectory as depicted in Fig. 11 would correspond to a path $\dots\omega_{n-1}\omega_n\omega_{n+1}\dots$. At equilibrium where the principle of detailed balancing holds, the forward and backward motions are equiprobable and a typical path $\dots 212132131223132\dots$ would contain short sequences as well as their time reversals, for instance 132 and 231. In contrast, the time reversals of typical sequences are less probable out of equilibrium by the theorem of nonequilibrium temporal ordering. This remarkable property leads to the emergence of directionality in the rotation of the shaft as observed in Fig. 11 where the paths are now restricted to $\dots 123123123123\dots$. For this nonequilibrium trajectory, the probability of the time reversal 321 of the observed short sequence 123 is essentially vanishing. In the regime of Fig. 11, the time-reversed temporal disorder (50) is thus very large while the temporal disorder (48) is very small. According to Eq. (51), the thermodynamic entropy production is thus large and positive, confirming that the motor is functioning away from equilibrium. This example shows that the directionality of the motion of molecular machines finds its origin in the nonequilibrium driving of these systems. The theorem of nonequilibrium temporal ordering is thus establishing a fundamental relationship between the second law of thermodynamics and the dynamical order that is observed, in particular, in biology. Indeed, the metabolism of biological systems is functioning out of equilibrium thanks to the energy supplied by the environment. This nonequilibrium driving allows the directionality of the various internal machines. This directionality means that the motion is dynamically ordered, a concept often intuitively quoted in biology. Remarkably, this dynamical order finds its fundamental understanding with the theorem of nonequilibrium temporal ordering.

In conclusion, the highly nonlinear dependence of the mean rotation rate of the γ -shaft (118) on the chemomechanical affinity (101) shows that, typically, the F_1 motor does not function in the linear-response regime defined by Onsager's linear-response coefficients, but instead runs in a nonlinear-response regime which is more the feature of far-from-equilibrium systems than of close-to-equilibrium ones. This remarkable property is to be attributed to the molecular architecture of the F_1 motor at the nanoscale, which allows the tight coupling between the mechanical motion and the chemical reactions powering the motor.

V. CHEMICAL NANOSYSTEMS

Besides the aforementioned mechanical and mechanochemical nanosystems, there also exist chemical systems where populations of molecules evolve in time by reactions. These reactions can take place in a small recipient playing the role of a reactor, for instance such as catalytic or electrochemical reactions at the surface of a nanoparticle or nanoelectrode. Other examples concern the biochemical reactions occurring in the nucleus or the cytosol of biological cells. Such reactions may form networks as it is the case for the metabolic networks or the genetic regulatory networks inside cells. Since the number of molecules is limited in such small systems, their time evolution is stochastic. These numbers are jumping at the random times corresponding to the random reactive events. This stochastic process is ruled by a chemical master equation for the probability that the system contains certain numbers of molecules of the species involved in the reactions. Such systems are out of equilibrium as long as the concentrations of these species have not reached their equilibrium ratios. The systems can be maintained out of equilibrium if the reactants are continuously supplied to the reactor from some reservoirs and the products are evacuated. This is the case for heterogeneous catalytic reactions on a solid surface in contact with a mixture of gases at fixed partial pressures. Since the reactions only happen at the surface thanks to its catalytic properties, the gaseous mixture acts as a reservoir containing large amounts of reactants. The reactions proceed out of equilibrium if the ratios of partial pressures do not take their equilibrium values. Since the numbers of molecules at the surface are small with respect to the numbers in the gaseous mixture, the nonequilibrium constraints can be maintained for arbitrarily long time intervals. Such nonequilibrium conditions are also satisfied if the reactants and products are supplied in larger quantities than the intermediate species. The ultimate situation is a reactive process taking place on a single molecule such as a molecular motor or a copolymer in the processes of DNA replication or protein synthesis. The importance of stochasticity has been emphasized in the context of genetic regulatory networks inside the cellular nucleus where the number of DNA molecules is necessarily limited [111, 112].

A. Chemical transistor

An example of purely chemical systems is provided by the “chemical transistor” defined by the network of the three following chemical reactions:



in which the molecules of the species X can be produced from three different reactant or product species coming from so many different reservoirs. The parameters k_ρ are the reaction constants. The number X of molecules of the intermediate species X is a random variable that is incremented by one every time a molecule coming from a reservoir is converted into X and decreased by one if a reversed reaction occurs.

For this stochastic process, the probability $P(X, t)$ that the system contains X molecules at time t is ruled by the master equation [20, 21, 53, 54, 108, 109]

$$\frac{d}{dt}P(X, t) = \sum_{\rho} [P(X - \nu_{\rho}, t) W_{+\rho}(X - \nu_{\rho}|X) - P(X, t) W_{-\rho}(X|X - \nu_{\rho})] \quad (122)$$

where ν_{ρ} denote the stoichiometric coefficients of the reactions $\rho = \pm 1, \pm 2, \pm 3$. The transition rates are given by

$$W_{+\rho}(X|X + 1) = k_{+\rho}\langle R_{\rho} \rangle \quad \nu_{+\rho} = +1 \quad (123)$$

$$W_{-\rho}(X|X - 1) = k_{-\rho}X \quad \nu_{-\rho} = -1 \quad (124)$$

with $\rho = 1, 2, 3$ [113]. The concentrations of the species in the reservoir determine the mean numbers $\langle R_{\rho} \rangle = \Omega[R_{\rho}]$ where Ω is the volume of the reservoir.

The concentration of the species X is defined in terms of the mean number of molecule as

$$[X] = \frac{\langle X \rangle}{\Omega} = \frac{1}{\Omega} \sum_{X=0}^{\infty} X P(X, t) \quad (125)$$

This concentration evolves in time according to the following rate equation of macroscopic chemical kinetics:

$$\frac{d[X]}{dt} = \sum_{\rho} k_{+\rho}[R_{\rho}] - \sum_{\rho} k_{-\rho}[X] \quad (126)$$

We notice that the macroscopic kinetic equation is here exactly recovered because the chemical reaction network (121) is linear in the sense that the transition rates (123)-(124) are at most linear in the number X . For such linear reactions, the stationary solution of the master equation is given by the Poisson probability distribution:

$$P_{\text{st}}(X) = e^{-\langle X \rangle} \frac{\langle X \rangle^X}{X!} \quad (127)$$

with the mean value

$$\langle X \rangle = \frac{\sum_{\rho} k_{+\rho}\langle R_{\rho} \rangle}{\sum_{\rho} k_{-\rho}} \quad (128)$$

The graph associated with the stochastic process has an infinite number of vertices for $X = 0, 1, 2, \dots$. Each pair $(X, X + 1)$ of vertices is connected by three non-directed edges, one for each of the three reactions (121). Figure 17 depicts the associated graph as well as alternative choices of maximal tree together with examples of possible chords defining cycles. Every time a transition occurs on one of these chords, the corresponding current (30) presents a delta peak. The analogy of this reaction network with a transistor is made by associating the three reservoirs with the source, the drain, and the gate of the transistor. Therefore, two independent affinities can be defined in such systems and they control two independent currents.

Using the cycle which starts from the state X , goes to the state $X + 1$ by the chord $\rho = \alpha$, and returns to the state X by the edge $\rho = -3$, the corresponding macroscopic affinity is defined by Eq. (28) as

$$A_{\alpha} \equiv \ln \frac{W_{+\alpha}(X|X + 1)W_{-3}(X + 1|X)}{W_{-\alpha}(X + 1|X)W_{+3}(X|X + 1)} = \ln \frac{k_{-3}k_{+\alpha}\langle R_{\alpha} \rangle}{k_{-\alpha}k_{+3}\langle R_3 \rangle} \quad (129)$$

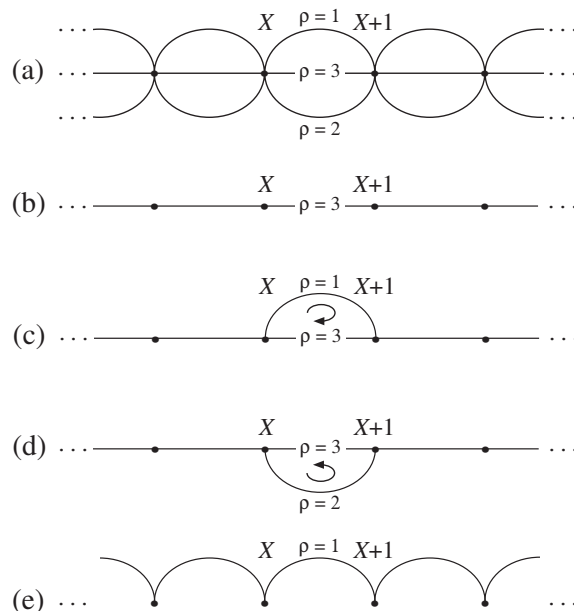


FIG. 17: (a) Graph G associated with the reaction network (121) of the “chemical transistor” [21]. (b) Maximal tree $T(G)$ obtained after removing all the edges corresponding to the reactions $\rho = 1$ and $\rho = 2$. (c) Subgraph $T(G) + l$ composed of the maximal tree $T(G)$ and the chord $l = X \xrightarrow{\rho=1} X+1$, forming a cycle contributing to the current j_1 of affinity A_1 . (d) Subgraph $T(G) + l$ composed of the maximal tree $T(G)$ and the chord $l = X \xrightarrow{\rho=2} X+1$, forming a cycle contributing to the current j_2 of affinity A_2 . (e) Alternative maximal tree $T'(G)$ obtained after removing all the edges corresponding to the reactions $\rho = 2$ and $\rho = 3$.

for $\alpha = 1$ or 2 , as shown respectively in Fig. 17c or 17d. There are therefore only two independent affinities in this chemical reaction network. These affinities only depend on the concentrations of the external reservoirs. The state of thermodynamic equilibrium is reached if both affinities vanish, i.e., if the following detailed balancing conditions are satisfied:

$$\frac{k_{+\rho}}{k_{-\rho}} \langle R_\rho \rangle = \langle X \rangle_{\text{eq}} \quad \text{with } \rho = 1, 2, 3 \quad (130)$$

These conditions fix the concentrations of two reservoirs in terms of the third reservoir R_3 . The equilibrium states thus depend on the third concentration $[R_3] = \langle R_3 \rangle / \Omega$ and form a hyperplane of codimension one in the three-dimensional space of the concentrations. The distance with respect to this equilibrium hyperplane is controlled by the two affinities (129).

The independent random fluxes or currents corresponding to the two affinities (129) can be defined by Eq. (30). The generating function of the statistical cumulants of these currents can be exactly calculated and is given by [113]

$$Q(\lambda_1, \lambda_2) = \frac{k_{+3} \langle R_3 \rangle}{k_{-3}} \left[k_{-1} e^{A_1} + k_{-2} e^{A_2} + k_{-3} - \frac{k_{-1} e^{\lambda_1} + k_{-2} e^{\lambda_2} + k_{-3}}{k_{-1} + k_{-2} + k_{-3}} (k_{-1} e^{A_1 - \lambda_1} + k_{-2} e^{A_2 - \lambda_2} + k_{-3}) \right] \quad (131)$$

which satisfies the fluctuation theorem (36)

$$Q(\lambda_1, \lambda_2) = Q(A_1 - \lambda_1, A_2 - \lambda_2) \quad (132)$$

in terms of the macroscopic affinities (129). The independent macroscopic fluxes (32) are given by [21]

$$J_1 = \frac{k_{-1} k_{+3} \langle R_3 \rangle}{k_{-1} + k_{-2} + k_{-3}} \left[e^{A_1} - 1 + \frac{k_{-2}}{k_{-3}} (e^{A_1} - e^{A_2}) \right] \quad (133)$$

$$J_2 = \frac{k_{-2} k_{+3} \langle R_3 \rangle}{k_{-1} + k_{-2} + k_{-3}} \left[e^{A_2} - 1 + \frac{k_{-1}}{k_{-3}} (e^{A_2} - e^{A_1}) \right] \quad (134)$$

which can be expanded in powers of the affinities according to Eq. (42). The Onsager reciprocity relations (43) can be verified as well as their generalizations (44) and (45) relating the higher-order response coefficients to the cumulants (33)-(35) [113]. The macroscopic expression of the thermodynamic entropy production (41) is thus recovered. In this reaction network, the fluxes have a strong nonlinear dependence on the thermodynamic forces or affinities, A_1 and A_2 , in spite of their linear dependence on the concentrations.

This is also the case for the chemical diode which is the special case where the second reservoir is decoupled from the system by setting $k_{\pm 2} = 0$. There remains a single flux between the first and the third reservoir which is given by [21]

$$J_1 = \frac{k_{-1}k_{+3}\langle R_3 \rangle}{k_{-1} + k_{-3}} (e^{A_1} - 1) \quad (135)$$

The flux can become arbitrarily large for positive values of the affinity, but saturates for negative values. This behavior is the one of an electric diode or rectifier.

We notice that the nonlinear dependences of the fluxes on the affinities have the same origin as those found in Eq. (118) and Fig. 15 for mechanochemical systems.

B. Chemical multistability

An example of bistable chemical system is given by Schlögl's trimolecular reaction network [114, 115]



On mesoscopic scales, the reaction is described as a stochastic process ruled by the master equation (122) with the transition rates:

$$W_{+1}(X|X+1) = k_{+1} [A] \Omega \quad \nu_{+1} = +1 \quad (138)$$

$$W_{-1}(X|X-1) = k_{-1} X \quad \nu_{-1} = -1 \quad (139)$$

$$W_{+2}(X|X-1) = k_{+2} X \frac{X-1}{\Omega} \frac{X-2}{\Omega} \quad \nu_{+2} = -1 \quad (140)$$

$$W_{-2}(X|X+1) = k_{-2} [B] X \frac{X-1}{\Omega} \quad \nu_{-2} = +1 \quad (141)$$

The macroscopic kinetic equation for the concentration (125) of the intermediate species X is given by

$$\frac{d}{dt}[X] = k_{+1}[A] - k_{-1}[X] - k_{+2}[X]^3 + k_{-2}[B][X]^2 \quad (142)$$

which is obtained from the master equation by neglecting the effects of fluctuations at $O(1/\Omega)$ in the limit $\Omega \rightarrow \infty$ [20]. This kinetic equation is nonlinear in the concentration, which leads to a phenomenon of bistability far from thermodynamic equilibrium as observed in Fig. 18a. Figure 18b depicts the entropy production showing that the regime of bistability exists far from the thermodynamic equilibrium state where the entropy production vanishes. Bistability is a particular case of multistability, which plays an important role in many nonlinear dissipative systems, especially, in genetic regulatory networks controlling cell differentiation and its maintenance [54].

A stochastic trajectory simulated by Gillespie's algorithm [57, 58] is depicted in Fig. 18c in the regime of bistability. Because of the fluctuations, the concentration does not remain forever in one of the two macroscopic steady states but randomly jumps between the upper and lower states. In this nonequilibrium regime, the stationary probability distribution is not Poissonian [20]. As suggested by the reaction network (136)-(137), a current is flowing between the reservoirs of molecules A and B. The graph associated with the stochastic process is shown in Fig. 19 confirming the existence of a single independent current associated with the affinity

$$A \equiv \ln \frac{W_{+1}(X|X+1)W_{+2}(X+1|X)}{W_{-1}(X+1|X)W_{-2}(X|X+1)} = \ln \frac{k_{+1}k_{+2}[A]}{k_{-1}k_{-2}[B]} \quad (143)$$

The generating function (31) of the unique current $j(t)$ obeys the fluctuation theorem $Q(\lambda) = Q(A - \lambda)$.

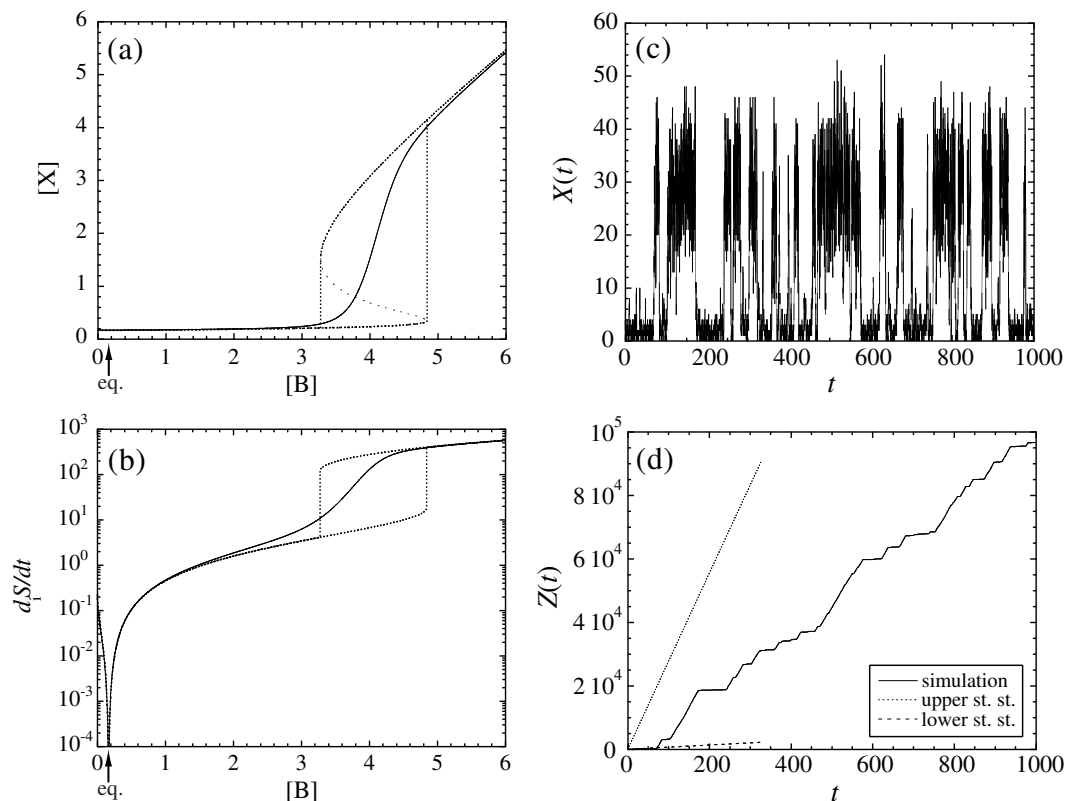


FIG. 18: Schlögl trimolecular model (136)-(137) with the control parameters $k_{+1}[A] = 0.5$, $k_{-1} = 3$, and $k_{+2} = k_{-2} = 1$: (a) Bifurcation diagram of the concentration $[X]$, obtained from the macroscopic equation (142) (dashed lines) and the stochastic description for $\Omega = 10$ (solid line). (b) Entropy production versus the control concentration $[B]$ given by the macroscopic theory (dashed lines) and by the stochastic description for $\Omega = 10$ (solid line). The thermodynamic equilibrium is located at $[B]_{\text{eq}} = \frac{1}{6}$. (c) Stochastic time evolution of the number X of molecules of the intermediate species X , simulated by Gillespie's algorithm for $[B] = 4$ and $\Omega = 10$. (d) Stochastic time evolution of the quantity $Z(t)$ for the trajectory (c) for $[B] = 4$ and $\Omega = 10$. The increase of $Z(t)$ fluctuates between the entropy production rate of the lower (long-dashed line) and upper (dashed line) macroscopic stationary concentrations, in correlation with the jumps seen in (c). (Adapted from Ref. [20].)

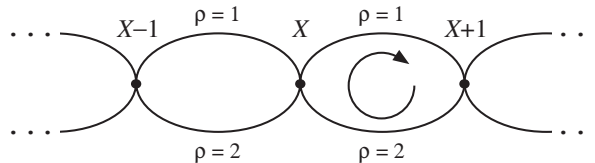


FIG. 19: Graph associated with the stochastic process of Schlögl's trimolecular model.

An alternative fluctuating quantity has been defined by Lebowitz and Spohn [18] as the following ratio

$$Z(t) \equiv \ln \frac{W_{+\rho_1}(X_0|X_1) W_{+\rho_2}(X_1|X_2) \cdots W_{+\rho_n}(X_{n-1}|X_n)}{W_{-\rho_1}(X_1|X_0) W_{-\rho_2}(X_2|X_1) \cdots W_{-\rho_n}(X_n|X_{n-1})} \quad (144)$$

Over long time intervals, this quantity is proportional to the fluctuating current, $Z(t) \simeq A \int_0^t dt' j(t')$. Accordingly, its statistical average in a stationary state gives the entropy production

$$\frac{1}{k_B} \frac{d_i S}{dt} = \lim_{t \rightarrow \infty} \frac{1}{t} \langle Z(t) \rangle = A J \geq 0 \quad (145)$$

The generating function of the statistical cumulants of the quantity (144) is defined as

$$q(\eta) \equiv \lim_{t \rightarrow \infty} -\frac{1}{t} \ln \langle e^{-\eta Z(t)} \rangle \quad (146)$$

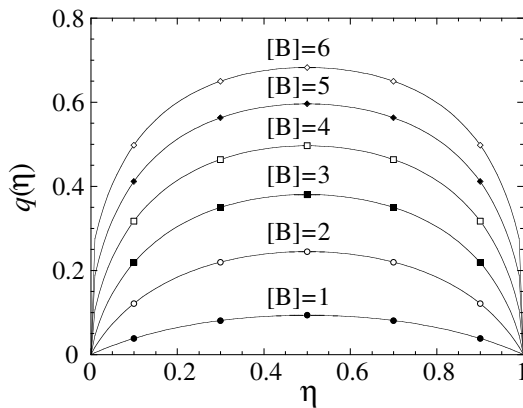


FIG. 20: Generating function (146) of the fluctuating quantity $Z(t)$ versus η in the Schlögl model (136)-(137) for $k_{+1}[A] = 0.5$, $k_{-1} = 3$, $k_{+2} = k_{-2} = 1$, $[B] = 1, 2, \dots, 6$, and $\Omega = 10$. We notice that $q(\eta) = 0$ at the equilibrium $[B]_{\text{eq}} = 1/6$. (Adapted from Ref. [20].)

and obeys the fluctuation theorem

$$q(\eta) = q(1 - \eta) \quad (147)$$

The behavior of the quantity (144) in the bistable regime is shown in Fig. 18d for the same stochastic trajectory as in Fig. 18c. Since the entropy production rate is larger in the upper state than in the lower, the quantity (144) increases faster during the time intervals when the system is in the upper state. The generating function of this quantity can be calculated numerically and is depicted in Fig. 20 for different values of the reservoir concentration $[B]$ from the monostable to the bistable regime. In all cases, the generating function is symmetric around $\eta = 1/2$, as predicted by the fluctuation theorem (147), which is thus verified in this far-from-equilibrium bistable chemical system.

We point out that the verification of the fluctuation theorem requires the coexistence of direct and reversed reactions in the network (136)-(137). If the rate constants k_p of some reactions were vanishing, the quantity (144) could not be defined and the thermodynamic entropy production (145) would be infinite. In this case, the reaction network would be said to be fully irreversible.

C. Chemical clocks

If the chemical reaction network involves two intermediate species X and Y, a self-sustained cyclic process becomes possible if the system is maintained far from equilibrium [69]. In such regimes, the chemical concentrations oscillate in time along a so-called limit cycle which is a periodic solution of the macroscopic kinetic equations [54]. Such rhythmic phenomena have been called chemical clocks [54] and observed not only in the famous Belousov-Zhabotinsky chemical reaction [116, 117] but also in biochemical reactions and in the regulatory networks at the basis of circadian rhythms [118]. On mesoscopic scales, the oscillations are affected by molecular fluctuations and the limit cycle is noisy. The description of such stochastic processes can be carried out in terms of the chemical master equation (122) now extended to the time evolution of the multivariate probability to find the system with given numbers of the different molecular species [54].

A model of oscillatory chemical reactions is provided by the so-called Brusselator, which is defined by the following reaction network [119]:



involving two intermediate species X and Y. The species A, B, and C are supposed to enter the system with the constant concentrations $[A]$, $[B]$, and $[C]$. We notice that the trimolecular reaction network (148)-(150) can be conceived as the

reduction of a larger bimolecular reaction network [120]. Because of the autocatalytic reaction (150), the macroscopic kinetic equations are nonlinear and this nonlinearity is at the origin of the oscillations. These oscillations persist in the fully irreversible Brusselator where the constants of the reversed reactions are vanishing, $k_{-1} = k_{-2} = k_{-3} = 0$, and the thermodynamic entropy production is infinite. In order to keep finite the entropy production, all the reaction constants should take non-vanishing values, which is here supposed.

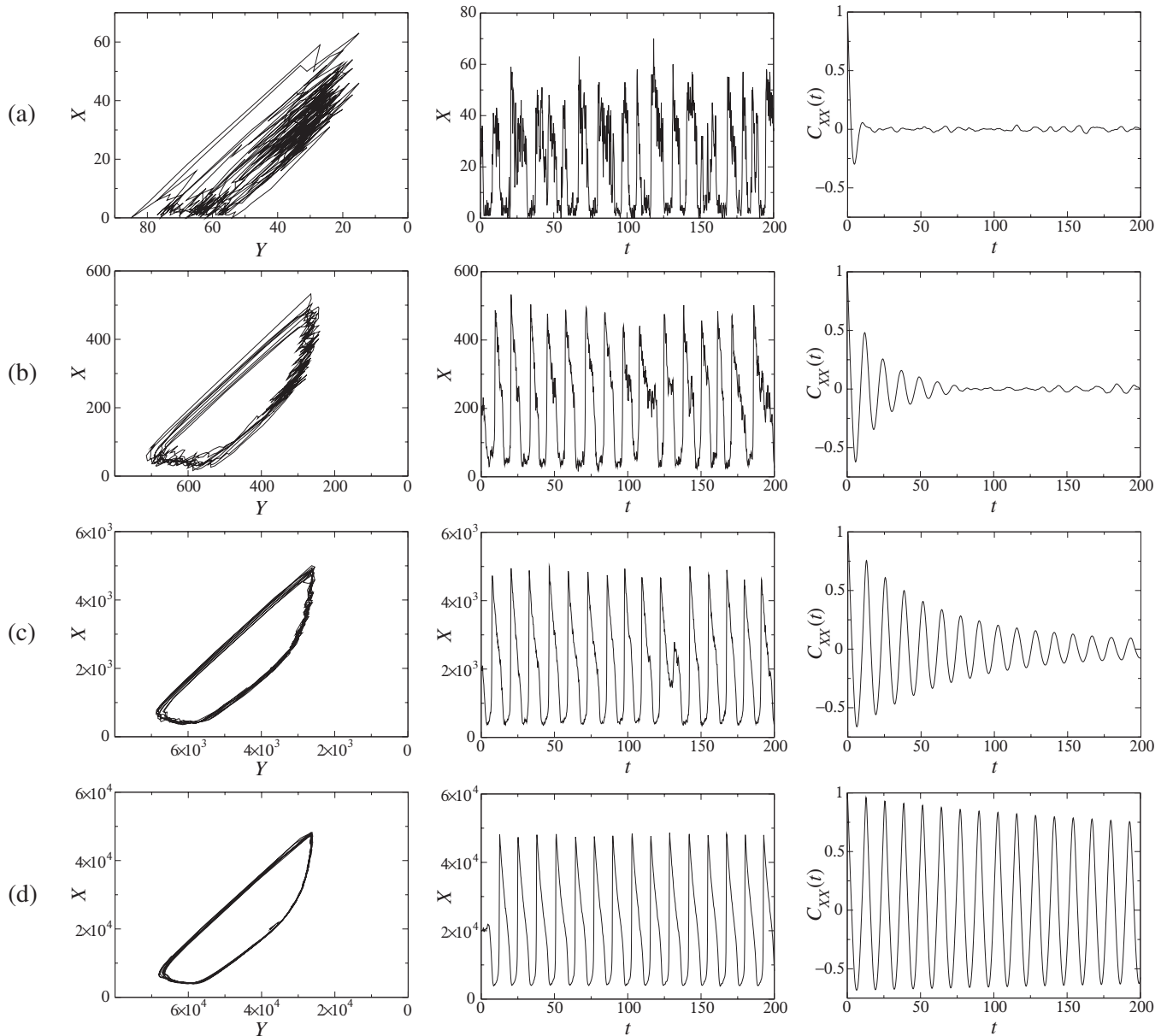


FIG. 21: Simulation by Gillespie's algorithm of the oscillatory regime for the reversible Brusselator (148)-(150). The values of the concentrations are $[B] = 7$, $[A] = [C] = 1$, and the reaction constants $k_{+1} = 0.5$, $k_{+2} = k_{+3} = 1$, $k_{-1} = k_{-2} = k_{-3} = 0.25$. From the top to the bottom, the extensivity parameter takes the values: (a) $\Omega = 10$, (b) $\Omega = 100$, (c) $\Omega = 1000$, and (d) $\Omega = 10000$. The first column depicts the phase portrait in the plane of the numbers X and Y of molecules. The second column shows the number X as a function of time. The third one depicts the autocorrelation function (157) of the number X , which is normalized to unity. (Adapted from Ref. [121].)

At the mesoscopic level, the random reactive events are described as a birth-and-death stochastic process for the numbers, $X(t)$ and $Y(t)$, of molecules of the intermediate species. This stochastic process is ruled by a Markovian master equation for the probability $P(X, Y, t)$ that the system contains the numbers X and Y of molecules at time t

[20, 21, 53, 54, 108, 109]. For the Brusselator, the transitions rates of the master equation are given by [121]

$$W_{+1}(X, Y|X + 1, Y) = k_{+1} [A] \Omega \quad (151)$$

$$W_{-1}(X, Y|X - 1, Y) = k_{-1} X \quad (152)$$

$$W_{+2}(X, Y|X - 1, Y + 1) = k_{+2} [B] X \quad (153)$$

$$W_{-2}(X, Y|X + 1, Y - 1) = k_{-2} [C] Y \quad (154)$$

$$W_{+3}(X, Y|X + 1, Y - 1) = k_{+3} \frac{X(X - 1)Y}{\Omega^2} \quad (155)$$

$$W_{-3}(X, Y|X - 1, Y + 1) = k_{-3} \frac{X(X - 1)(X - 2)}{\Omega^2} \quad (156)$$

where Ω is the extensivity parameter characterizing the volume of the system.

Figure 21 shows examples of stochastic trajectories numerically simulated by Gillespie's algorithm [57, 58] for different values of the extensivity parameter Ω [121]. The reaction constants and the reservoir concentrations correspond to the same regime of oscillations. Since the numbers of molecules in the system is proportional to the extensivity parameter Ω , the size of the system increases with the parameter Ω . In the small system of Fig. 21a, the molecular fluctuations are so important that regular oscillations are not visible. Indeed, the time autocorrelation function depicted in the third column rapidly decays to zero before the completion of a single cycle. Regular oscillations emerge if the system contains a few hundred molecules at larger values of Ω , as seen in Fig. 21b. In this case, the time autocorrelation function presents several oscillations before decaying to zero. The oscillations become more regular as the size further increases in Figs. 21c and 21d. For any finite size, the time autocorrelation function presents exponentially damped oscillations

$$C_{XX}(t) = \frac{\langle X(t)X(0) \rangle}{\langle X \rangle^2} - 1 \sim e^{-\gamma t} \cos(\omega t + \phi) \quad (157)$$

with a correlation time proportional to the extensivity parameter $\gamma^{-1} \sim \Omega$. The constant of proportionality can be calculated by the Hamilton-Jacobi method in the weak-noise limit [122] and determines how the nonlinearities of the reaction network controls the robustness of the oscillations with respect to the molecular fluctuations.

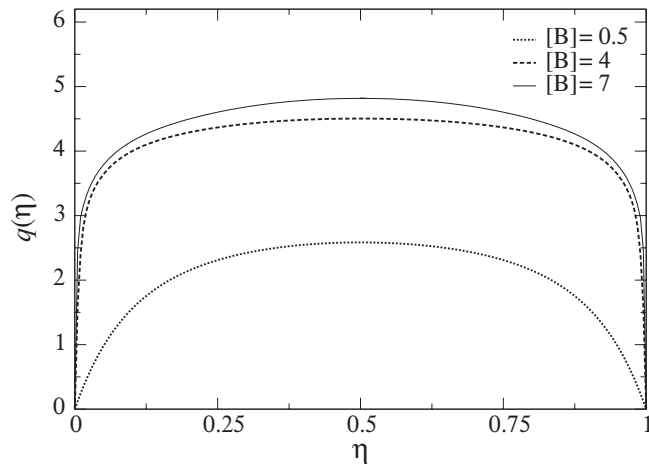


FIG. 22: The generating function (146) numerically obtained for the Brusselator. The extensivity parameter takes the value $\Omega = 15$ while the control parameter takes the values $[B] = 0.5, 4, 7$. The reaction constants and the other concentrations are fixed at the values $k_{+1} = 0.5$, $k_{+2} = k_{+3} = 1$, $k_{-1} = k_{-2} = k_{-3} = 0.25$, and $[A] = [C] = 1$. For these parameter values, the equilibrium state is found at $[B]_{\text{eq}} = 0.0625$, the steady state is a stable node for $0 < [B] < 4.03024$ and a stable focus for $4.03024 < [B] < 6.36667$. The Hopf bifurcation happens at the critical concentration $[B]_{\text{Hopf}} = 6.36667$. Below this critical value, the steady state is an attractor. Above criticality for $6.36667 < [B]$, the attractor is the limit cycle of Fig. 21. (Adapted from Ref. [121].)

Remarkably, the fluctuation theorem (147) is satisfied in the far-from-equilibrium oscillatory regime for both the quantity (144) and the fluctuating currents between the reservoirs [121]. In particular, the generating function of the quantity (144) is symmetric for a reflection around $\eta = 1/2$, as verified in Fig. 22. For $[B] = 7$, the system evolves in the oscillatory regime of Fig. 21.

We notice the analogy between the cyclic processes of molecular motors and chemical clocks. Both types of cyclic processes can be self-sustained if the system is driven out of equilibrium with appropriate thermodynamic forces or affinities. What is most remarkable is that such nonequilibrium systems are functioning in regimes of rotations or oscillations although there is no time-dependent external driving. The temporal periodicity is an intrinsic feature to the system. Both types of systems have important differences. The functionality of molecular motors finds its origin in their molecular architecture with proteins playing the roles of shaft and barrel in the F_1 motor for instance. On the other hand, chemical clocks are functioning by the time evolution of molecular populations. We may wonder which is most efficient to generate regular oscillations. The results here above show that populations with several hundreds or thousands of molecules are required for chemical clocks to emerge from the molecular fluctuations [122]. These sizes are not significantly different from the numbers of atoms composing molecular motors although the molecular architecture tends to confer to these latter well-defined shapes of their own [7–10].

D. Chemical clocks observed in field emission microscopy

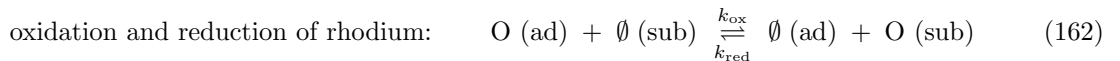
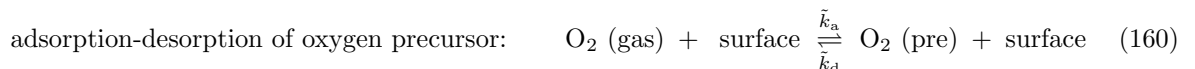
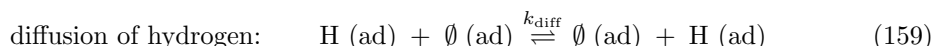
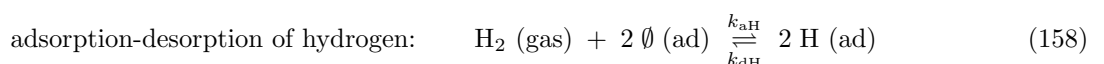
Nanometric chemical clocks have been experimentally observed thanks to field emission microscopy [123–128]. The principle of this microscopy is the magnification provided by an electric field extending from the nanometric tip of a metallic needle to a fluorescent screen [129].

Under a negative voltage, electrons are emitted by the needle and move along the lines of the electric field to arrive at the fluorescent screen at the points corresponding to the emission points at the surface of the needle tip. As a consequence, an image of the surface of the needle is projected on the screen with a magnification factor equal to the ratio of the curvature radii of the screen and the needle tip. This method is called field electron microscopy (FEM).

An alternative method is field ion microscopy (FIM). In this case, the needle is subjected to a positive voltage and the vacuum chamber is filled with gas such as neon. When the neutral neon atoms collide with the surface of the needle, they are ionized and the resulting positive ion is projected to the screen along the line of electric field corresponding to the locus of ionization. The image seen on the fluorescent screen is the magnification of the surface of the needle. Since the needle is crystalline, its surface presents terraces and steps. The electric field is higher at the steps where the ionization rate is enhanced and which thus appear more clearly on the screen. This method invented by Erwin Müller is historically the first microscopy to achieve atomic resolution already in the fifties [130].

In the nineties, chemical clocks have first been observed in FEM [123, 124] and later in FIM with a higher (close to atomic) resolution [125, 126]. An example is provided by the reaction of catalytic water formation from hydrogen and oxygen on rhodium [127, 128]. The electric field at the tip of the rhodium needle is about 12 V/nm. The rhodium field emitter tip is exposed to a gaseous mixture of hydrogen and oxygen at fixed partial pressures. The radius of curvature of the tip is of the order of 10 nm. Since the reaction is concentrated at the tip because of the enhancement of the partial pressures by high electric fields, the field emitter tip constitutes a nanoreactor. Regular oscillations with a period of 30-40 seconds are observed around the partial pressures $P_{H_2} = 2 \times 10^{-3}$ Pa, $P_{O_2} = 2 \times 10^{-3}$ Pa, $P_{H_2O} = 0$, and temperature $T = 550$ K. These oscillations are self-sustained because the partial pressures of hydrogen, oxygen, and water are not in their chemical equilibrium ratios and the system is driven far from equilibrium.

The oscillations can be explained by the following reaction network [131]



Both hydrogen and oxygen diatomic molecules undergo a dissociative adsorption on the rhodium surface. The hydrogen atoms are highly mobile on rhodium. On the other hand, the oxygen atoms are strongly bounded to the surface and some of them move below the surface to form a surface rhodium oxide layer with the stoichiometry of RhO_2 . This surface oxide modifies the rate of adsorption of oxygen on the surface, which is the feedback mechanism at the origin of the oscillations. Water is formed from the combination of hydrogen and oxygen atoms and desorbs from the

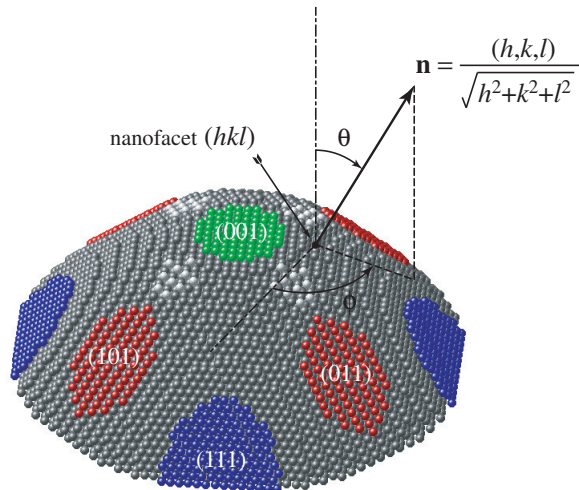


FIG. 23: Ball model of the field emitter tip with the unit vector $\mathbf{n} = (\sin \theta \cos \phi, \sin \theta \sin \phi, \cos \theta)$ perpendicular to the nanofacet of Miller indices (h, k, l) of an underlying fcc crystal. All the balls inside a paraboloid are retained in this model of the field emitter. We notice that the mean electric field points in the same direction $\mathbf{F} = F\mathbf{n}$ because the electric field is always perpendicular to the surface of a conductor such as the field emitter tip. The (001) nanofacet is at the tip's apex. (Adapted from Ref. [131].)

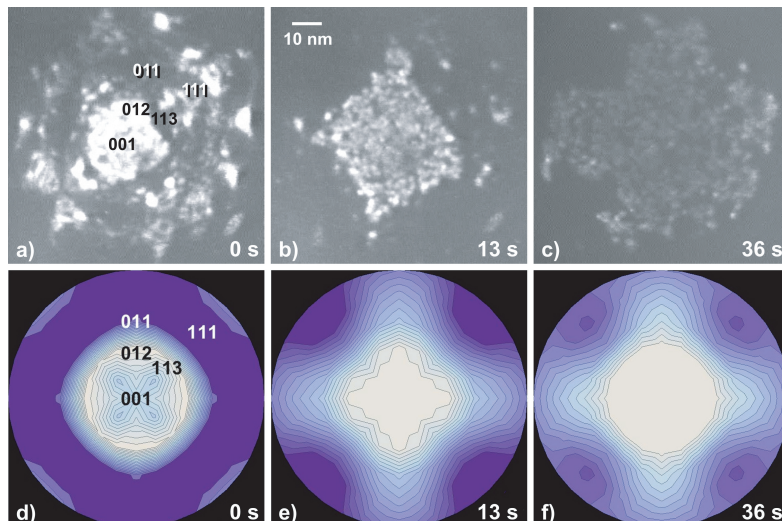


FIG. 24: Series of FIM micrographs covering the complete oscillatory cycle as well as the corresponding time evolution of the subsurface oxygen distribution on a logarithmic scale as obtained within a kinetic model of the field emitter tip. Starting from a surface in the quasi-metallic state (a) and (d), an oxide layer invades the topmost plane and grows along the {011} facets forming a nanometric cross-like structure (b) and (e). The oxide front spreads to finally the whole visible surface area (c) and (f). The temperature, electric field and partial pressures of oxygen in panels (a), (b) and (c) are $T = 550$ K, $F_0 = 12$ V/nm, $P_{\text{O}_2} = 2 \times 10^{-3}$ Pa, respectively. On the other hand, the hydrogen pressure in panels (c), (d) and (e) is $P_{\text{H}_2} = 2 \times 10^{-3}$ Pa in the FIM experiments and 4×10^{-3} Pa in the kinetic model (158)-(163). For the subsurface site occupation, the white areas indicate a high site occupation value while the dark areas indicate a low site occupation value. (Adapted from Ref. [131].)

surface. Most of the water molecules leave the surface in a neutral form but a fraction is ionized and contributes to the imaging of the surface by FIM.

Remarkable oscillatory patterns are observed in FIM [127, 128, 131]. These patterns have a length scale of tens of nanometers, which is much smaller than the typical length scales of ten to hundred micrometers for the patterns of reaction-diffusion processes in heterogeneous catalysis [132, 133]. The nanopatterns of the reactions observed in FIM can be explained in terms of the structural anisotropy of the crystalline tip, which results in different catalytic powers for the various exposed nanofacets [131]. Indeed, the activation energy E_x^\ddagger and the prefactor k_x^0 of each rate

coefficient depend on the crystalline orientation of the nanofacet where the reaction occurs. Each crystalline nanofacet is characterized by its Miller indices (h, k, l) or, equivalently, by the unit vector \mathbf{n} perpendicular to the corresponding crystalline plane $\mathbf{n} = (h, k, l)/\sqrt{h^2 + k^2 + l^2}$ (see Fig. 23). Moreover, the activation energy and the prefactor also depend on the magnitude F of the electric field normal to the metallic surface. If the tip is supposed to have the geometry of a paraboloid with a radius of curvature R at its apex, the electric field is known [129, 134] to vary as

$$F = \frac{F_0}{\sqrt{1 + (r/R)^2}} \quad (164)$$

where r is the radial distance with respect to the symmetry axis of the paraboloid and F_0 is the magnitude of the electric field at the apex of the tip. According to Arrhenius' law, the rate coefficient of each reaction can thus be written as

$$k_x = k_x^0(\mathbf{n}, F) \exp \left[-\frac{E_x^\ddagger(\mathbf{n}, F)}{k_B T} \right] \quad (165)$$

giving the spatial dependence describing the anisotropy of the crystalline tip, which is central to explain the nanopatterns observed in the experiment (see Fig. 24) [131].

In spite of the nanometric size of the chemical clocks, the oscillations are regular. The reason is that the system contains several thousands of adsorbed atoms, which is above the minimum number of a few hundred required for regular oscillations to emerge [122]. As a consequence, chemical clocks can exist at the nanoscale.

E. Single-copolymer processes

The theorem of nonequilibrium temporal ordering stated in Subsection IIF shows that dynamical order may appear in temporal sequences of events if the system is driven away from equilibrium. If the system had the ability to record the temporal sequence on a spatial support, the dynamical order would result into spatial order. The idea of coupling the dynamical order predicted by Eq. (51) with a spatial support of information has been developed in Ref. [32] to explain the possibility of information generation or information processing in nonequilibrium systems such as biosystems. Indeed, the theorem of nonequilibrium temporal ordering suggests that a nonequilibrium system can process information thanks to the directionality of its movements.

At the nanoscale, a natural spatial support of information is provided by random copolymers where information can be coded in the covalent bonds between the different monomers composing the copolymer chain. This is the idea of the aperiodic crystal that Erwin Schrödinger proposed in his famous 1944 book, *What is Life?* [135]. As discovered in 1953 by Watson and Crick [136], the copolymer coding genetic information is DNA, in which a pair of nucleotides composed of about 64 atoms codes for two bits of information at the nanometer scale. DNA is but one among various types of copolymers in chemical and biological systems. Such copolymers are synthesized either with or without a template (see Fig. 25). Styrene-butadiene is an example of random copolymer grown without a template. Examples of copolymerizations with a template are provided by the processes of DNA replication, DNA-mRNA transcription, and mRNA-protein translation [5].

Copolymerization necessarily proceeds away from equilibrium so that the growth of copolymers is controlled by the nonequilibrium conditions fixed in particular by the chemical concentrations of the monomers in the solution surrounding the growing copolymer. Since copolymers have the size of nanometers, copolymerization processes are affected by the molecular fluctuations and should be described as stochastic processes. At equilibrium, the principle of detailed balancing prevents the ordering of temporal events, hence the possibility to generate or transmit information. Out of equilibrium, the ordering of temporal events becomes possible thanks to energy supply. On this condition, the molecular motions acquire a directionality, allowing information generation or transmission (see Fig. 25c).

1. Copolymerization without a template

The stochastic growth of a single copolymer $\omega = m_1 m_2 m_3 \cdots m_l$ composed of monomers $m_i \in \{1, 2, \dots, M\}$ can be described in terms of a master equation for the probability $P(\omega, t)$ to find the copolymer ω at time t [32, 33]

$$\frac{dP(\omega, t)}{dt} = \sum_{\omega'} [P(\omega', t) W(\omega'|\omega) - P(\omega, t) W(\omega|\omega')] \quad (166)$$

where $W(\omega|\omega')$ is the rate of the transition $\omega = m_1 m_2 m_3 \cdots m_l \rightarrow \omega' = m_1 m_2 m_3 \cdots m_{l'}$. During this transition, the length of the copolymer may change as $l \rightarrow l' = l \pm 1$ because of the attachment or detachment of a monomer. For many

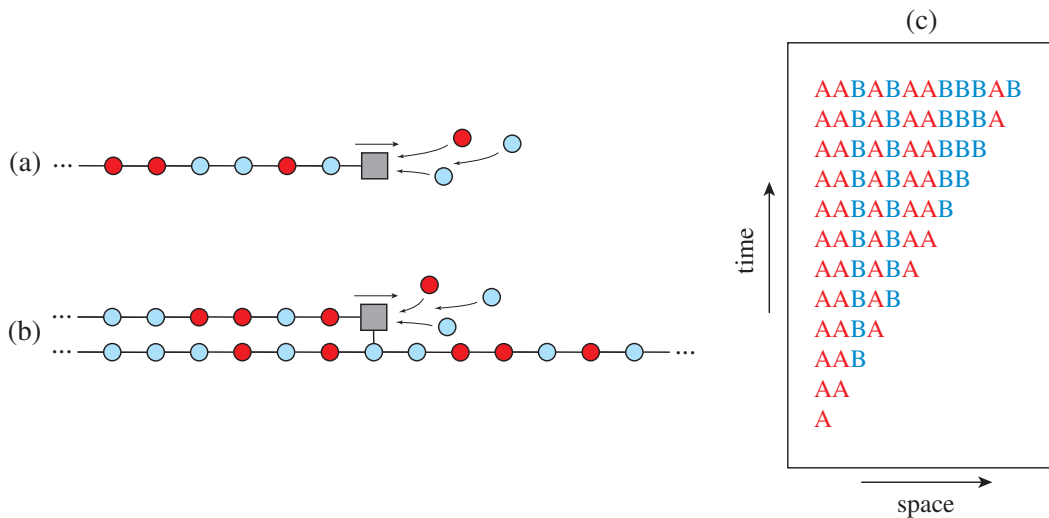


FIG. 25: Schematic representations of (a) a copolymerization process without a template, (b) a copolymerization process with a template. The circles depict the monomers and the square the catalyst of polymerization (adapted from Ref. [32]). (c) Schematic space-time plot of the growth process of a random copolymer composed of monomers A and B. The spatial sequence of monomers in the grown copolymer is directly determined by the temporal sequence of random attachments of A or B monomers at each time step.

processes at fixed pressure and temperature T , the ratio of forward to backward transition rates can be expressed as [6]

$$\frac{W(\omega|\omega')}{W(\omega'|\omega)} = \exp \frac{G(\omega) - G(\omega')}{k_B T} \quad (167)$$

in terms of the free enthalpy $G(\omega)$ of a single copolymer chain ω surrounded by the solution. This Gibbs free energy is related to the enthalpy $H(\omega)$ and the entropy $S(\omega)$ of the copolymer ω in its environment at the temperature T by

$$G(\omega) = H(\omega) - T S(\omega) \quad (168)$$

Since the system is described by the statistical distribution $P(\omega, t)$ giving the probability to find the particular copolymer ω at time t , the overall entropy of the system is given by Eq. (21) and it varies in time according to Eq. (22) because of the exchange of entropy (23) between the copolymer and its surrounding and the entropy production (24).

The growth may proceed in a regime described by the stationary statistical distribution $\mu_l(\omega)$ giving the composition of the copolymer chain ω provided that its length is equal to l [137, 138]. This distribution is normalized as $\sum_{\omega} \mu_l(\omega) = 1$. In the regime of stationary growth, the probability distribution of the system becomes

$$P(\omega, t) = p(l, t) \mu_l(\omega) \quad (169)$$

where the time dependence is included in the statistical distribution $p(l, t)$ of the lengths l of the chains. The mean length of the chains is defined by $\langle l \rangle_t = \sum_l l \times p(l, t)$ and the mean growth velocity

$$v = \frac{d\langle l \rangle_t}{dt} \quad (170)$$

is supposed to be constant. Since the statistical composition of the copolymer is stationary, it is characterized by the mean entropy, enthalpy and free enthalpy per monomer defined as

$$s \equiv \lim_{l \rightarrow \infty} \frac{1}{l} \sum_{\omega} \mu_l(\omega) S(\omega) \quad (171)$$

$$h \equiv \lim_{l \rightarrow \infty} \frac{1}{l} \sum_{\omega} \mu_l(\omega) H(\omega) \quad (172)$$

$$g \equiv \lim_{l \rightarrow \infty} \frac{1}{l} \sum_{\omega} \mu_l(\omega) G(\omega) = h - T s \quad (173)$$

By substituting Eq. (169) in Eq. (21), the entropy of the system can be shown to have a dominant linear dependence on the mean chain length over long time intervals and its time derivative can be written as [32]

$$\frac{dS}{dt} = v [s + D(\text{polymer})] \quad (174)$$

in terms of the mean entropy per monomer s and the spatial disorder per monomer defined by the Shannon entropy per monomer [139, 140]

$$D(\text{polymer}) = \lim_{l \rightarrow \infty} -\frac{1}{l} \sum_{\omega} \mu_l(\omega) \ln \mu_l(\omega) \quad (175)$$

On the other hand, the entropy exchange (23) can be expressed in terms of the enthalpy per monomer as

$$\frac{d_e S}{dt} = v \frac{h}{T} \quad (176)$$

so that the thermodynamic entropy production is given by

$$\frac{d_i S}{dt} = v A \geq 0 \quad (177)$$

in terms of the affinity per monomer

$$A \equiv -\frac{g}{T} + D(\text{polymer}) = \varepsilon + D(\text{polymer}) \quad (178)$$

where $\varepsilon = -g/T$ is the driving force of the copolymer growth [32]. This driving force is positive if the Gibbs free energy decreases as the copolymer grows, in which case the growth is driven by energetic effect. If the copolymer is random, its spatial disorder is positive so that the driving force can take negative values down to its equilibrium value $\varepsilon_{\text{eq}} = -D(\text{polymer})$ where the affinity (178) is vanishing. As a consequence, a random copolymer can grow by entropic effects in an adverse free-energy landscape [32, 141].

2. Copolymerization with a template

Similar considerations apply to the case of copolymerization processes taking place with a template given for instance by another copolymer [32]. This latter is characterized by the statistical distribution $\nu_l(\alpha)$ of the sequences α of length l , which is normalized as $\sum_{\alpha} \nu_l(\alpha) = 1$. The growing copolymer ω now acquires a composition which depends on the template α . In the stationary regime, the statistical distribution of the system can here be written as

$$P(\omega, t) = p(l, t) \mu_l(\omega|\alpha) \quad (179)$$

where $\mu_l(\omega|\alpha)$ gives the conditional probability of the copy ω given the composition α of the template over the length l of the copy [32]. The joint probability to find the copy ω and the template α is defined as

$$\mu_l(\omega, \alpha) \equiv \nu_l(\alpha) \mu_l(\omega|\alpha) \quad (180)$$

and the probability of the copy ω for all the possible templates α is given by

$$\mu_l(\omega) \equiv \sum_{\alpha} \nu_l(\alpha) \mu_l(\omega|\alpha) = \sum_{\alpha} \mu_l(\omega, \alpha) \quad (181)$$

The Shannon conditional disorder of the copy grown on a given template is defined as [139, 140]

$$D(\text{polymer}|\text{template}) = \lim_{l \rightarrow \infty} -\frac{1}{l} \sum_{\alpha, \omega} \nu_l(\alpha) \mu_l(\omega|\alpha) \ln \mu_l(\omega|\alpha) \quad (182)$$

while the Shannon disorder of all the possible copies is still defined by Eq. (175) with the probability distribution (181). The mutual information per monomer between the copy and the template is thus defined as [140]

$$I(\text{polymer}, \text{template}) \equiv D(\text{polymer}) - D(\text{polymer}|\text{template}) = \lim_{l \rightarrow \infty} \frac{1}{l} \sum_{\alpha, \omega} \mu_l(\omega, \alpha) \ln \frac{\mu_l(\omega, \alpha)}{\nu_l(\alpha) \mu_l(\omega)} \quad (183)$$

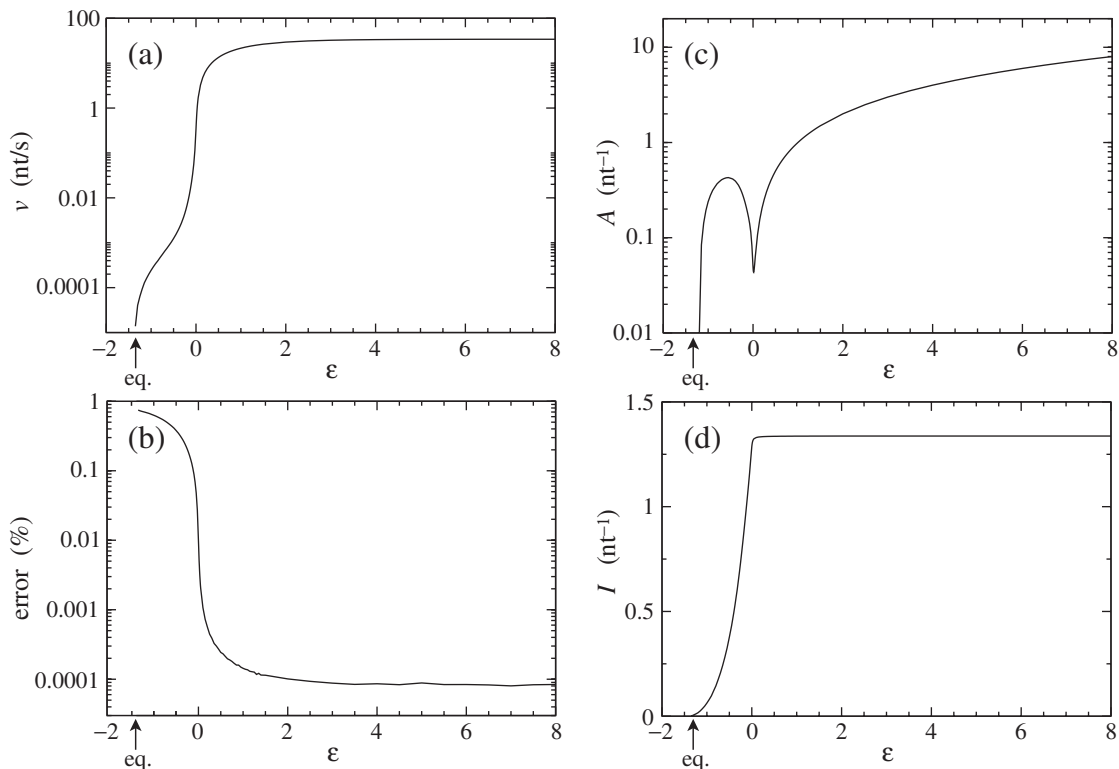


FIG. 26: Replication process of human mitochondrial DNA by polymerase Pol γ : (a) Velocity of versus the driving force ϵ . (b) Percentage of DNA replication errors versus the driving force ϵ . (c) Affinity per copied nucleotide versus the driving force ϵ . (d) Mutual information between the copied DNA strand and the original strand serving as template, versus the driving force ϵ (adapted from Ref. [32]).

The mutual information is always non negative and bounded as

$$0 \leq I(\text{polymer, template}) \leq \text{Min} \{D(\text{polymer}), D(\text{template})\} \quad (184)$$

Following a similar reasoning as in the case without a template, the thermodynamic entropy production can be written as Eq. (177) with the affinity per monomer here given by

$$A \equiv \epsilon + D(\text{polymer}|\text{template}) = \epsilon + D(\text{polymer}) - I(\text{polymer, template}) \quad (185)$$

with the driving force $\epsilon = -g/T$ [32]. This fundamental result shows that a positive mutual information becomes possible away from equilibrium where the thermodynamic entropy production and the affinity are positive: The larger the mutual information, the better the transmission of information between the template and the copy. This phenomenon can be illustrated for the case of DNA replication [32].

3. DNA replication

In vivo, DNA replication is a nonequilibrium process which costs the free energy of two ATP molecules for the attachment of one nucleotide [5]. DNA replication is performed by a whole machinery which separates the two strands of DNA and catalyses the growth of two new strands by DNA polymerases. Moreover, an exonuclease performs a proofreading for the correction of possible errors [142, 143].

The influence of the nonequilibrium constraints has been studied in the case of the DNA polymerase Pol γ , which replicates the human mitochondrial DNA [32]. The human mitochondrial DNA is 16.5 kb long and can be obtained from GenBank [144]. Forward kinetic constants k_{+mn} for the incorporation of both correct and incorrect nucleotides are available [145]. The reversed kinetic constants are taken as $k_{-mn} = k_{+mn}e^{-\epsilon}$ in terms of the driving force ϵ , which is the control parameter of the nonequilibrium constraints. The thermodynamic equilibrium corresponds to the value $\epsilon_{\text{eq}} = -\ln 4$. The replication process has been simulated by Gillespie's algorithm [57, 58].

Figure 26a depicts the mean velocity of replication in nucleotide per second as a function of the driving force. The velocity vanishes at equilibrium and increases towards a maximum value of about 34 nucleotides per second for a large and positive driving force. On the other hand, the percentage of errors in the replication process takes the large value of 75% at equilibrium and drops by several orders of magnitude away from equilibrium (see Fig. 26b). The percentage of replication errors does not vanish far from equilibrium and constitutes a source of genetic mutations. By the way, the analysis shows that the thermal and molecular fluctuations cause replication errors and, thus, mutations.

Since the growth velocity is positive, the thermodynamic entropy production per copied nucleotide is given by the affinity (178) depicted in Fig. 26c. The local minimum around $\varepsilon \simeq 0.015$ marks the transition between the regime driven by entropic effect and the one driven by energy effect. On the other hand, Fig. 26d shows the mutual information per nucleotide (183) between the copy and the template. This mutual information vanishes at equilibrium and reaches a plateau at the maximum value $I_{\max} \simeq 1.337$ nats far from equilibrium. Therefore, the transmission of information between the template and the copy is not possible at equilibrium, but requires that the process is pushed far enough from equilibrium for the replication to be accurate. The fidelity of replication is characterized by the percentage of errors or by the mutual information between the copy and the template [32].

If the copolymerization process was running too close to the thermodynamic equilibrium, the mutations would be too frequent to allow replication and self-reproduction. Therefore, the self-reproduction of biological systems is closely connected to their metabolism, i.e., to their nonequilibrium nature. This connection finds its origin in the aforementioned phenomenon of nonequilibrium temporal ordering. It is remarkable to see that the ingredients of Darwinian evolution are so closely related to the basic physico-chemical laws of nonequilibrium nanosystems. The experimental study of copolymerization processes under tunable nonequilibrium conditions is awaiting the development of new single-molecule techniques such as nanopore sequencing [33, 146, 147].

VI. CONCLUSIONS AND PERSPECTIVES

Many nanosystems play an important role because they function out of equilibrium. The nonequilibrium constraints allow useful motions to be sustained in nanosystems as it is the case for molecular motors, electronic nanosystems, or catalytic nanodevices.

Although nanosystems are affected by thermal and molecular fluctuations, thermodynamic considerations continue to apply thanks to recent advances in nonequilibrium statistical thermodynamics, which have led to the discovery of new fundamental relationships valid not only close to but also far from equilibrium.

Nanosystems may be isolated or in contact with one or several reservoirs. Because of their intermediate size between the atoms and the macroscopic objects, their study requires the connection between different levels of description. Their microscopic dynamics is ruled by Newtonian or Hamiltonian equations for the motion of all the atoms. Often a few degrees of freedom are relevant to the specific property of interest in a nanosystem. These few degrees of freedom are typically slower than the other ones, which results into a separation of time scales justifying a description in terms of stochastic processes, as explained in Section II. Different stochastic processes can be envisaged depending on the level of coarse graining of the relevant quantities. These quantities may be the work performed on a nanosystem by some external force or the currents flowing across the nanosystem. At the nanoscale, these quantities are fluctuating in time so that their recording over some time interval generates random temporal sequences called paths or histories. Each path has a certain probability to occur in a long time series, which defines the probability distribution characterizing the stochastic process. If the stochastic process is stationary, the probability distribution is invariant under time evolution. This is the case at thermodynamic equilibrium where the microcanonical, canonical or grand-canonical probability distributions describe the statistical averages as well as the fluctuations of the relevant quantities. This concept of invariant probability distribution has the subtle feature of remaining a stationary solution of Liouville equation of time evolution while describing individual systems which are highly dynamical with incessant temporal fluctuations. The conceptual advantage of probability distribution is to introduce two levels of descriptions: (1) the single-system level which is dynamical and (2) the statistical-ensemble level in terms of a probability distribution which can remain stationary and thus invariant in time. Since the aforementioned equilibrium distributions are functions of the Hamiltonian, they are symmetric under time reversal if the Hamiltonian is.

Now, the concept of stationary probability distribution extends to nonequilibrium nanosystems in which heat or particle currents are flowing across the system between reservoirs at different temperatures or chemical potentials. Here also the quantities of interest may fluctuate and be highly dynamical at the single-system level and, yet, be described by a stationary probability distribution for the possible random paths or histories followed by the system. The bonus provided by the probabilistic description is that nonequilibrium states such as chemical clocks, which are considered as being time-dependent at the macroscale, can nevertheless be described by a stationary probability distribution at the mesoscale in the presence of fluctuations. Indeed, the stationary probability distribution of the paths may lead to time correlation functions which present (damped) oscillations as illustrated in Fig. 21. There

is thus no incompatibility to describe a system with non-trivial time evolutions in terms of a stationary probability distribution.

Typically, the mean currents are non vanishing in such nonequilibrium steady states as they flow from one reservoir to another in a well-defined direction. Although currents flowing in the opposite direction are possible, both nonequilibrium steady states are physically distinct. At the level of the stationary probability distribution, the paths in the direction of the mean currents are more probable than their time reversals. This fundamental remark shows that the stationary probability distributions of nonequilibrium steady states break the time-reversal symmetry. This symmetry breaking happens at the statistical level of description and is therefore perfectly compatible with microreversibility. This latter property only says that, if Newton's or Liouville's equations admit a solution, they also admit its time reversal as solution. However, microreversibility does not mean that the solution and its time reversal should coincide. In the case where they are physically distinct – which happens most often – the selection of one out of the pair is breaking the time-reversal symmetry. This phenomenon is well known in condensed-matter physics as spontaneous symmetry breaking. Nevertheless, this concept has not been considered until very recently for the time-reversal symmetry in nonequilibrium statistical mechanics [34–38].

Remarkably, the relationship (51) shows that the thermodynamic entropy production is an order parameter for the breaking of the time-reversal symmetry in nonequilibrium steady states. Indeed, Eq. (51) gives the entropy production as the difference between the temporal disorders of the time-reversed and forward paths. At equilibrium, the forward and reversed temporal disorders are equal because of the principle of detailed balancing. Out of equilibrium, the time reversals are less probable than the typical paths so that the time-reversed temporal disorder becomes larger than the forward one, which results into a positive thermodynamic entropy production. Accordingly, a directionality manifests itself away from equilibrium, which is expressed by the theorem of nonequilibrium temporal ordering stated in Subsection IIF. Most remarkably, the breaking of time-reversal symmetry has been experimentally verified down to the nanoscale [30, 31]. In this way, the property of irreversibility that was previously envisaged for macrosystems containing about 10^{23} atoms is nowadays considered in small systems containing a few hundred or thousand atoms.

The time-reversal symmetry breaking of the stationary probability distribution concerns all the large-deviation properties of nonequilibrium nanosystems, as reported in Section II. Amazingly, these properties obey universal relationships which are the consequence of microreversibility. Such relationships have been discovered in different types of dynamical systems and stochastic processes and they are commonly called fluctuation theorems [11–27]. Recently, a fluctuation theorem has been proved for all the independent currents flowing across a nonequilibrium system thanks to graph theory [21–23]. This theory allows us to identify the thermodynamic forces – also called the affinities [68, 69] – as well as the corresponding random currents by using the cycles of the graph associated with the stochastic process. To some extent, these cycles play a similar role as the periodic orbits in dynamical systems theory [38, 47]. Once the affinities are identified in a stochastic process, the symmetry (40) can be proved for the generating function of the statistical cumulants of the fluctuating currents, which is the content of the fluctuation theorem. This generating function provides us with the full counting statistics of the particles flowing across a nonequilibrium system such as an electronic, photonic, or chemical nanodevices [24–27]. Moreover, the symmetry of the fluctuation theorem for the currents allows us to deduce not only the Onsager-Casimir reciprocity relations for the linear response coefficients, but also the generalizations (44)-(46) of these relations to the nonlinear response coefficients [71]. These generalizations relate the nonlinear response coefficients to the statistical cumulants (33)-(35) characterizing the fluctuations. The fluctuation theorem for currents has also been proved for open quantum systems and apply to boson and fermion transport through mesoscopic junctions in electronic, photonic, or ultracold-atom devices [26, 27].

Besides, fluctuation theorems have been obtained for Hamiltonian systems driven by time-dependent forces thanks to a framework due to Jarzynski [11, 12]. The work performed on the system is a random variable similar to the number of particles exchanged between reservoirs and their fluctuations also obey a symmetry relation. In this way, the equilibrium free energy of conformation changes can be experimentally measured by folding and unfolding biomolecules [4]. All these new fundamental results give promising perspectives in our understanding of nonequilibrium nanosystems, as revealed by the case studies presented in this review.

The mechanical nanosystems considered in Section III are Hamiltonian and isolated possibly driven by external time-dependent forces.

The double-walled carbon nanotubes (DWCNT) can slide relative to one another in a telescopic motion [82–85]. Systems containing about 1300 atoms can be studied by molecular dynamics simulations, showing that the energy of the sliding motion is dissipated among the vibrational degrees of freedom of each nanotube. This dissipation is caused by the friction coming from the van der Waals interaction between the nanotubes. The methods of Brownian motion theory extends from the micrometer down to the nanometer. Accordingly, the translational and rotational sliding motions are described by Langevin stochastic models with dynamic friction coefficients given by the Kirkwood formula of nonequilibrium statistical mechanics [60]. If the DWCNT system is isolated, it undergoes a relaxation towards a microcanonical equilibrium state with fluctuations in the sliding motions described by Langevin equations. However,

the internal rotation between the two nanotubes can be driven by external forces as it is the case in nanomechanical devices using DWCNTs for the shaft of rotary motors. In such devices, the energy continuously supplied by the external driving is dissipated by the property of rotational friction described in Section III.

The other example presented in Section III is the heating of a microplasma by electromagnetic waves. This is a time-dependent Hamiltonian system to which Crooks fluctuation theorem applies for the work performed by the time-dependent electric force on the microplasma. This work represents the energy supplied to the system and is a random variable depending on the initial conditions. Heating corresponds to a positive value of the work and cooling to a negative value. As described by the fluctuation theorem, the work is statistically distributed around a positive most probable value, which corresponds to the heating of the system.

Section IV presents the F_1 -ATPase motor, which is an example of nanosystem powered by a continuous supply of chemical energy [99, 100, 104, 105]. Both the shaft and the barrel of this nanomotor are composed of proteins. The barrel is a hexamer of proteins, three of which can bind adenosine triphosphate (ATP). ATP hydrolysis is the source of energy allowing the active rotation of the shaft in a mean unidirectional motion. The ATP molecules are coming from the aqueous solution surrounding the protein and they bind in the catalytic sites of the motor at random arrival times. These arrival times form a stationary random process for constant values of ATP concentration. In this regard, the nanomotor does not need an external cyclic driving, but has its own autonomous cycle as a car engine at constant gas supply. In the F_1 nanomotor, ATP hydrolysis is catalyzed by the conformational change of the protein, inducing the rotation of the shaft by a mechanism similar to a camshaft [101]. In this way, the chemical energy is transformed into mechanical motion at the expense of some dissipation which necessarily reduces the efficiency of energy transduction. This process can be investigated in detail thanks to continuous-state or discrete-state stochastic models [106, 107]. The regimes of tight or loose coupling between the chemistry and the mechanics of the motor can be identified. Although the chemical reaction and the mechanical rotation constitute *a priori* two independent dissipative processes leading to entropy production, they combine together in the tight-coupling regime in such a way that a single independent dissipative process remains. In this tight-coupling regime, the mechanical efficiency can reach its maximum possible value (105). Remarkably, the rotation rate of the nanomotor has a highly nonlinear dependence on the thermodynamic force or affinity driving the system out of equilibrium contrary to what is usually supposed. This nonlinear dependence allows the rotation to be much faster than it would be the case if the nanomotor was functioning in the regime of linear response, whereupon a rotation rate of 130 rev/sec can be obtained under physiological conditions [99, 100]. As a consequence, the rotation rate drops to extremely slow rates close to the equilibrium state and random backward rotations are very rare although the fluctuation theorem remains valid [110]. As discussed at the end of Section IV, the directionality of the rotation is directly related to the fact that the motor is functioning out of equilibrium, which can be understood as the consequence of the theorem of nonequilibrium temporal ordering [29].

Further examples of nonequilibrium nanosystems evolving along an autonomous cycle are provided by the nanometric chemical clocks described in Section V. In these systems, the time evolution concerns the populations composed of many identical molecules of small size, instead of the motion of mechanical pieces formed by large rigid molecules as carbon nanotubes or proteins. If the molecular architecture is instrumental to the mechanical rotation of molecular motors, it plays a secondary role in chemical clocks where the chemical concentrations of some intermediate species undergo oscillations. At the macroscale, these concentrations obey kinetic ordinary differential equations established by the laws of chemical kinetics [54, 69]. These equations are nonlinear if the reaction network contains autocatalytic steps. Far from equilibrium, their solutions may undergo bifurcations leading to bistability, limit cycles, or even chaotic attractors. At the nanoscale, the populations contain hundred or thousand molecules so that the reactive events induce random jumps in the concentrations, whereupon their time evolution is stochastic. Such stochastic processes can be driven out of equilibrium if the reactants and the products are supplied in proportions different from their chemical equilibrium values, in which case a source of chemical free energy maintains the matter fluxes from the reactants to the products. These fluxes are similar to the currents across an electronic circuit and they obey a fluctuation theorem which is remarkably valid far from equilibrium as shown in Section V for bistability in Schlögl trimolecular model [20] and for oscillations in the Brusselator model [121]. As illustrated with the chemical transistor, the fluctuation theorem allows us to recover the Onsager reciprocity relations for the linear response coefficients and to verify their generalizations to the nonlinear response coefficients [21, 71, 113]. The discovery of these new relations in the nonlinear response regime constitutes an important advance in nonequilibrium statistical thermodynamics since Onsager classic paper of 1931 [70].

Field emission microscopy reveals the existence of nanometric chemical clocks [131]. These nonequilibrium nanosystems are the stage of catalytic reactions on metallic surface at the field emitter tip. By the localization of a high electric field, the tip constitutes a nanoreactor of a few dozen nanometers where patterns are observed in the coverage of the surface by adsorbed species. In some regimes, these nanopatterns may oscillate as it is the case in the reaction of water formation from hydrogen and oxygen on rhodium [131]. In spite of the nanometric size of the tip, several thousand atoms are adsorbed on the surface so that the system is large enough to sustain correlated oscillations and

behave as a chemical clock [122]. The observed nanopatterns can be understood in terms of the spatial dependence of the reaction coefficients on the orientation of each nanofacet composing the tip with respect to the underlying metallic crystal [131].

Further nonequilibrium nanosystems where chemical reactions play a fundamental role are those composed of a single copolymer which is growing by the attachment of monomers coming from the surrounding solution [32, 33]. Here also, the process is stochastic since the single copolymer has nanometric size and the reactive events occur at random with either attachment or detachment of monomers. These copolymerization processes can take place freely or with a template. The latter case is fundamental for biology since DNA replication, DNA-mRNA transcription, and mRNA-protein translation are so many examples of such copolymerization processes. They are powered by chemical energy supply and, therefore, proceed in nonequilibrium regimes. For instance, DNA replication requires two ATP for the attachment of each nucleotide [5]. In this regard, the self-reproduction closely depends on the metabolism. This close connection can be further established by considering the nonequilibrium statistical thermodynamics of such copolymerization processes. In this way, the thermodynamic entropy of a single copolymer can be shown to depend on the Shannon disorder in the sequence of monomers composing the copolymer [32]. This spatial disorder contributes to the thermodynamic entropy production of copolymerization. Accordingly, the growth of the copolymer can be driven by the entropic effect of this spatial disorder besides the energetic effect due to the Gibbs free energy of monomer attachment. In the case of copolymerization with a template, the thermodynamic entropy production also depends on the mutual Shannon information between the template and the copy, which shows that nonequilibrium thermodynamics plays a fundamental role in the control of information processing at the molecular level [32, 33].

These new results pave the way towards a statistical thermodynamics of nonequilibrium nanosystems. They open new perspectives in our understanding of the motions and processes that nanosystems can perform. The thermodynamic forces or affinities driving the fluxes and currents can be identified and related to thermodynamic quantities such as energy and entropy, allowing us to study energy dissipation in nanosystems and their efficiency. Moreover, new lights are shed on the possible bridges between biology and the physico-chemical laws. Indeed, biological systems present structures on all scales from the macroscale down to the nanoscale. The hierarchical organization of living systems often appears in contrast with textbook physico-chemical systems which are typically homogeneous such as gases, liquids, and other continuous media. Therefore, the investigation of nonequilibrium biological processes at the nanoscale is very new. In particular, the new advances provide conceptual methods to study the metabolism of biological systems at the molecular level and to shift from 3D to 4D molecular biology.

The new results also concern the dynamical aspects of information and they establish the possibility of temporal ordering in nonequilibrium nanosystems. Indeed, the recent results suggest that the dynamical order so characteristic of biological systems can be understood on the basis of the second law of thermodynamics thanks to the appreciation of the importance of path probabilities and the breaking of time-reversal symmetry in the statistical description of nonequilibrium processes.

Acknowledgments

This research is financially supported by the Belgian Federal Government (IAP project “NOSY”), the “Communauté française de Belgique” (contract “Actions de Recherche Concertées” No. 04/09-312), and the F.R.S.-FNRS Belgium (contract F.R.F.C. No. 2.4577.04).

-
- [1] A. Einstein, *Investigations on the theory of the Brownian movement* (Dover, New York, 1956).
 - [2] W. A. de Heer, *Rev. Mod. Phys.* **65**, 611 (1993).
 - [3] M. Schmidt, R. Kusche, T. Hippler, J. Donges, W. Kronmüller, B. von Issendorff, and H. Haberland, *Phys. Rev. Lett.* **86**, 1191 (2001).
 - [4] D. Collin, F. Ritort, C. Jarzynski, S. B. Smith, I. Tinoco Jr., and C. Bustamante, *Nature* **437**, 231 (2005).
 - [5] B. Alberts, D. Bray, A. Johnson, J. Lewis, M. Raff, K. Roberts, and P. Walter, *Essential Cell Biology* (Garland Publishing, New York, 1998).
 - [6] T. L. Hill, *Free Energy Transduction and Biochemical Cycle Kinetics* (Dover, New York, 2005).
 - [7] M. Schienbein and H. Gruler, *Phys. Rev. E* **56**, 7116 (1997).
 - [8] H.-P. Lerch, R. Rigler, and A. S. Mikhailov, *Proc. Natl. Acad. Sci. USA* **102**, 10807 (2005).
 - [9] Y. Togashi and A. S. Mikhailov, *Proc. Natl. Acad. Sci. USA* **104**, 8697 (2007).
 - [10] A. Cressman, Y. Togashi, A. S. Mikhailov, and R. Kapral, *Phys. Rev. E* **77**, 050901 (2008).
 - [11] C. Jarzynski, *Phys. Rev. Lett.* **78**, 2690 (1997).
 - [12] G. E. Crooks, *Phys. Rev. E* **60**, 2721 (1999).

- [13] D. J. Evans, E. G. D. Cohen, and G. P. Morriss, *Phys. Rev. Lett.* **71**, 2401 (1993).
- [14] S. Tasaki and P. Gaspard, *J. Stat. Phys.* **81**, 935 (1995).
- [15] G. Gallavotti and E. G. D. Cohen, *Phys. Rev. Lett.* **74**, 2694 (1995).
- [16] G. Gallavotti, *Phys. Rev. Lett.* **77**, 4334 (1996).
- [17] J. Kurchan, *J. Phys. A: Math. Gen.* **31**, 3719 (1998).
- [18] J. L. Lebowitz and H. Spohn, *J. Stat. Phys.* **95**, 333 (1999).
- [19] C. Maes, *J. Stat. Phys.* **95**, 367 (1999).
- [20] P. Gaspard, *J. Chem. Phys.* **120**, 8898 (2004).
- [21] D. Andrieux and P. Gaspard, *J. Chem. Phys.* **121**, 6167 (2004).
- [22] D. Andrieux and P. Gaspard, *J. Stat. Phys.* **127**, 107 (2007).
- [23] D. Andrieux, *Nonequilibrium Statistical Thermodynamics at the Nanoscale* (Ph. D. thesis, Université Libre de Bruxelles, 2008).
- [24] D. Andrieux and P. Gaspard, *J. Stat. Mech.: Th. Exp.* P01011 (2006).
- [25] U. Harbola, M. Esposito, and S. Mukamel, *Phys. Rev. B* **76**, 085408 (2007).
- [26] D. Andrieux, P. Gaspard, T. Monnai, and S. Tasaki, *New J. Phys.* **11**, 043014 (2009).
- [27] M. Esposito, U. Harbola, and S. Mukamel, *Rev. Mod. Phys.* **81**, 1665 (2009).
- [28] P. Gaspard, *J. Stat. Phys.* **117**, 599 (2004).
- [29] P. Gaspard, *C. R. Physique* **8**, 598 (2007).
- [30] D. Andrieux, P. Gaspard, S. Ciliberto, N. Garnier, S. Joubaud, and A. Petrosyan, *Phys. Rev. Lett.* **98**, 150601 (2007).
- [31] D. Andrieux, P. Gaspard, S. Ciliberto, N. Garnier, S. Joubaud, and A. Petrosyan, *J. Stat. Mech.* P01002 (2008).
- [32] D. Andrieux and P. Gaspard, *Proc. Natl. Acad. Sci. USA* **105**, 9516 (2008).
- [33] D. Andrieux and P. Gaspard, *J. Chem. Phys.* **130**, 014901 (2009).
- [34] P. Gaspard, in: P. Collet et al., Eds, *Chaotic Dynamics and Transport in Classical and Quantum Systems* (Kluwer, Dordrecht, 2005) p. 107.
- [35] P. Gaspard, *Physica A* **369**, 201 (2006).
- [36] P. Gaspard, *Adv. Chem. Phys.* **135**, 83 (2007).
- [37] P. Gaspard, in: S. Ishiwata and Y. Matsunaga, Eds., *Physics of Self-Organization Systems* (World Scientific, New Jersey, 2008) p. 67.
- [38] P. Gaspard, *Chaos, Scattering and Statistical Mechanics* (Cambridge University Press, Cambridge UK, 1998).
- [39] V. I. Arnold and A. Avez, *Ergodic Problems of Classical Mechanics* (W. A. Benjamin, New York, 1968).
- [40] I. P. Cornfeld, S. V. Fomin, and Ya. G. Sinai, *Ergodic Theory* (Springer, Berlin, 1982).
- [41] J.-P. Eckmann and D. Ruelle, *Rev. Mod. Phys.* **57**, 617 (1985).
- [42] Ch. Dellago, H. A. Posch, and W. G. Hoover, *Phys. Rev. E* **53**, 1485 (1996).
- [43] H. van Beijeren, J. R. Dorfman, H. A. Posch, and Ch. Dellago, *Phys. Rev. E* **56**, 5272 (1997).
- [44] R. van Zon, H. van Beijeren, and Ch. Dellago, *Phys. Rev. Lett.* **80**, 2035 (1998).
- [45] H.-L. Yang and G. Radons, *Phys. Rev. E* **71**, 036211 (2005).
- [46] P. Gaspard and X.-J. Wang, *Phys. Rep.* **235**, 291 (1993).
- [47] P. Cvitanović and B. Eckhardt, *J. Phys. A: Math. Gen.* **24**, L237 (1991).
- [48] L. Boltzmann, *Lectures on Gas Theory* (Dover, New York, 1964).
- [49] P. Langevin, *Comptes rendus Acad. Sci. (Paris)* **146**, 530 (1908).
- [50] A. D. Fokker, *Ann. Physik* **43**, 810 (1914).
- [51] M. Planck, *Sitzungsber. Preuss. Akad. Wissens.* (1917) p. 324.
- [52] W. Pauli, in: *Festschrift zum 60. Geburtstag A. Sommerfelds* (Hirzel, Leipzig, 1928) p. 30.
- [53] D. A. McQuarrie, *Suppl. Rev. Series Appl. Prob.* **8**, 1 (1967).
- [54] G. Nicolis and I. Prigogine, *Self-Organization in Nonequilibrium Systems* (Wiley, New York, 1977).
- [55] N. G. van Kampen, *Stochastic Processes in Physics and Chemistry* (North-Holland, Amsterdam, 1981).
- [56] C. W. Gardiner, *Handbook of Stochastic Methods for Physics, Chemistry and the Natural Sciences*, 3rd ed. (Springer, Berlin, 2004).
- [57] D. T. Gillespie, *J. Comput. Phys.* **22**, 403 (1976).
- [58] D. T. Gillespie, *J. Phys. Chem.* **81**, 2340 (1977).
- [59] S. Chandrasekhar, *Rev. Mod. Phys.* **15**, 1 (1943).
- [60] J. G. Kirkwood, *J. Chem. Phys.* **14**, 180 (1946).
- [61] M. S. Green, *J. Chem. Phys.* **20**, 1281 (1952); **22**, 398 (1954).
- [62] R. Kubo, *J. Phys. Soc. Jpn.* **12**, 570 (1957).
- [63] M. Esposito, *Kinetic theory for quantum nanosystems* (Ph. D. thesis, Université Libre de Bruxelles, 2004).
- [64] J. Schnakenberg, *Rev. Mod. Phys.* **48**, 571 (1976).
- [65] J.-L. Luo, C. Van den Broeck, and G. Nicolis, *Z. Phys. B - Condensed Matter* **56**, 165 (1984).
- [66] G. N. Lewis, *Proc. Natl. Acad. Sci. USA* **11**, 179 (1925).
- [67] P. W. Bridgman, *Phys. Rev.* **31**, 101 (1928).
- [68] T. De Donder and P. Van Rysselberghe, *Affinity* (Stanford University Press, Menlo Park CA, 1936).
- [69] I. Prigogine, *Introduction to Thermodynamics of Irreversible Processes* (Wiley, New York, 1967).
- [70] L. Onsager, *Phys. Rev.* **37**, 405 (1931).
- [71] D. Andrieux and P. Gaspard, *J. Stat. Mech.: Th. Exp.* P02006 (2007).
- [72] D. Andrieux and P. Gaspard, *Europhys. Lett.* **81**, 28004 (2008).

- [73] G. Hummer and A. Szabo, *Acc. Chem. Res.* **38**, 504 (2005).
- [74] S. Mukamel, *Phys. Rev. Lett.* **90**, 170604 (2003).
- [75] D. Andrieux and P. Gaspard, *Phys. Rev. Lett.* **100**, 230404 (2008).
- [76] R. Kawai, J. M. R. Parrondo, and C. Van den Broeck, *Phys. Rev. Lett.* **98**, 080602 (2007).
- [77] C. Maes and K. Netočný, *J. Stat. Phys.* **110**, 269 (2003).
- [78] S. Iijima, *Nature* **354**, 56 (1991).
- [79] J. Cumings and A. Zettl, *Science* **289**, 602 (2000).
- [80] A. M. Fennimore, T. D. Yuzvinsky, Wei-Qiang Han, M. S. Fuhrer, J. Cumings, and A. Zettl, *Nature* **424**, 408 (2003).
- [81] B. Bourlon, D. C. Glattli, C. Miko, L. Forró, and A. Bachtold, *Nano Letters* **4**, 709 (2004).
- [82] J. Servantie and P. Gaspard, *Phys. Rev. Lett.* **91**, 185503 (2003).
- [83] J. Servantie and P. Gaspard, *Phys. Rev. B* **73**, 125428 (2006).
- [84] J. Servantie and P. Gaspard, *Phys. Rev. Lett.* **97**, 186106 (2006).
- [85] J. Servantie, *Dynamics and friction in double walled carbon nanotubes* (Ph. D. thesis, Université Libre de Bruxelles, 2006).
- [86] R. Saito, G. Dresselhaus, and M. S. Dresselhaus, *Physical Properties of Carbon Nanotubes* (Imperial College Press, London, 1998).
- [87] D. W. Brenner, *Phys. Rev. B* **42**, 9458 (1990).
- [88] J. P. Lu, X. P. Li, and R. M. Martin, *Phys. Rev. Lett.* **68**, 1551 (1992).
- [89] A. Buldum and J. P. Lu, *Phys. Rev. Lett.* **83**, 5050 (1999).
- [90] Q. Zheng and Q. Jiang, *Phys. Rev. Lett.* **88**, 045503 (2002).
- [91] P. Tangney, M. L. Cohen, and S. G. Louie, *Phys. Rev. Lett.* **97**, 195901 (2006).
- [92] X. H. Zhang, G. E. Santoro, U. Tartaglino, and E. Tosatti, *Phys. Rev. Lett.* **102**, 125502 (2009).
- [93] J. J. Bollinger and D. J. Wineland, *Sci. Am.* **262**, 114 (1990).
- [94] H. Walther, *Adv. At. Mol. Opt. Phys.* **31**, 137 (1993).
- [95] P. K. Ghosh, *Ion Traps* (Clarendon Press, Oxford, 1995).
- [96] P. Gaspard, *Phys. Rev. E* **68**, 056209 (2003).
- [97] J. P. Abrahams, A. G. W. Leslie, R. Lutter, and J. E. Walker, *Nature* **370**, 621 (1994).
- [98] R. Ian Menz, J. E. Walker, and A. G. W. Leslie, *Cell* **106**, 331 (2001).
- [99] H. Noji, R. Yasuda, M. Yoshida, and K. Kinosita Jr., *Nature* **386**, 299 (1997).
- [100] R. Yasuda, H. Noji, M. Yoshida, K. Kinosita Jr., and H. Itoh, *Nature* **410**, 898 (2001).
- [101] K. Kinosita Jr., K. Adachi, and H. Itoh, *Annu. Rev. Biophys. Biomol. Struct.* **33**, 245 (2004).
- [102] F. Jülicher, A. Ajdari, and J. Prost, *Rev. Mod. Phys.* **69**, 1269 (1997).
- [103] F. Oosawa and S. Hayashi, *Adv. Biophys.* **22**, 151 (1986).
- [104] T. Elston, H. Wang, and G. Oster, *Nature* **391**, 510 (1998).
- [105] H. Wang and G. Oster, *Nature* **396**, 279 (1998).
- [106] P. Gaspard and E. Gerritsma, *J. Theor. Biol.* **247**, 672 (2007).
- [107] E. Gerritsma and P. Gaspard, *Biophys. Rev. Lett.* **5**, 163 (2010).
- [108] G. Nicolis, *J. Stat. Phys.* **6**, 195 (1972).
- [109] M. Malek-Mansour and G. Nicolis, *J. Stat. Phys.* **13**, 197 (1975).
- [110] D. Andrieux and P. Gaspard, *Phys. Rev. E* **74**, 011906 (2006).
- [111] H. H. McAdams and A. Arkin, *Proc. Natl. Acad. Sci. USA* **94**, 814 (1997).
- [112] D. Gonze, J. Halloy, and P. Gaspard, *J. Chem. Phys.* **116**, 10997 (2002).
- [113] D. Andrieux and P. Gaspard, *Phys. Rev. E* **77**, 031137 (2008).
- [114] F. Schlögl, *Z. Phys.* **248**, 446 (1971).
- [115] F. Schlögl, *Z. Phys.* **253**, 147 (1972).
- [116] B. B. Belousov, *Sb. Ref. Radiats. Med. (Medgiz, Moscow, 1958)* p. 145.
- [117] A. M. Zhabotinskii, *Biophysika* **9**, 306 (1964).
- [118] A. Goldbeter, *Biochemical Oscillations and Cellular Rhythms* (Cambridge, University Press, Cambridge UK, 1996).
- [119] R. Lefever, G. Nicolis, and P. Borckmans, *J. Chem. Soc., Faraday Trans. 1* **84**, 1013 (1988).
- [120] F. Baras, J. E. Pearson, and M. Malek Mansour, *J. Chem. Phys.* **93**, 5747 (1990).
- [121] D. Andrieux and P. Gaspard, *J. Chem. Phys.* **128**, 154506 (2008).
- [122] P. Gaspard, *J. Chem. Phys.* **117**, 8905 (2002).
- [123] M. F. H. van Tol, M. Gilbert, and B. E. Nieuwenhuys, *Catal. Lett.* **16**, 297 (1992).
- [124] V. Gorodetskii, J. H. Block, and M. Ehsasi, *Appl. Surf. Sci.* **67**, 198 (1992).
- [125] V. Gorodetskii, W. Drachsel, and J. H. Block, *Catal. Lett.* **19**, 223 (1993).
- [126] C. Voss and N. Kruse, *Appl. Surf. Sci.* **94/95**, 186 (1996).
- [127] T. Visart de Bocarmé, T. Bär, and N. Kruse, *Ultramicroscopy* **89**, 75 (2001).
- [128] T. Visart de Bocarmé, G. Beketov, and N. Kruse, *Surf. Interface Anal.* **36**, 522 (2004).
- [129] M. K. Miller, A. Cerezo, M. G. Hetherington, and G. D. W. Smith, *Atom Probe Field Ion Microscopy* (Clarendon Press, Oxford, 1996).
- [130] E. W. Müller, *Z. Physik* **131**, 136 (1951).
- [131] J.-S. McEwen, P. Gaspard, T. Visart de Bocarmé, and N. Kruse, *Proc. Natl. Acad. Sci. USA* **106**, 3006 (2009).
- [132] G. Ertl, P. Norton, and J. Rustig, *Phys. Rev. Lett.* **49**, 177 (1982).
- [133] M. P. Cox, G. Ertl, and R. Imbihl, *Phys. Rev. Lett.* **54**, 1725 (1985).
- [134] T. Visart de Bocarmé, N. Kruse, P. Gaspard, and H. J. Kreuzer, *J. Chem. Phys.* **125**, 054704 (2006).

- [135] E. Schrödinger, *What is Life?* (Cambridge University Press, Cambridge UK, 1944).
- [136] J. D. Watson and F. H. C. Crick, *Nature* **171**, 737 (1953).
- [137] B. D. Coleman and T. G. Fox, *J. Polym. Sci. A* **1**, 3183 (1963).
- [138] B. D. Coleman and T. G. Fox, *J. Chem. Phys.* **38**, 1065 (1963).
- [139] C. E. Shannon, *Bell System Tech. J.* **27**, 379 (1948); *ibid.* **27**, 623 (1948).
- [140] T. M. Cover and J. A. Thomas, *Elements of Information Theory* (Wiley, Hoboken, 2006).
- [141] C. Jarzynski, *Proc. Natl. Acad. Sci. USA* **105**, 9451 (2008).
- [142] J. J. Hopfield, *Proc. Natl. Acad. Sci. USA* **71**, 4135 (1974).
- [143] C. H. Bennett, *Biosystems* **11**, 85 (1979).
- [144] Homo sapiens DNA mitochondrion, 16569 bp, locus AC 000021, version GI:115315570, <http://www.ncbi.nlm.nih.gov>.
- [145] H. Lee and K. Johnson, *J. Biol. Chem.* **281**, 36236 (2006).
- [146] Y. Astier, O. Braha, and H. Bayley, *J. Am. Chem. Soc.* **128**, 1705 (2006).
- [147] M. Zwolak and M. Di Ventra, *Rev. Mod. Phys.* **80**, 141 (2008).